Università degli Studi di Napoli "Federico II"

Dottorato di Ricerca in Fisica Fondamentale ed Applicata
XIV Ciclo (1998-2001)

Dimension and shape effects on the electronic spectrum of nanostructures

Thesis for Doctor of Philosophy degree
submitted by Giovanni Cantele

Supervisors:
Prof. G. Iadonisi
Prof. D. Ninno

Coordinator:
Prof. R. Musto

Contents

Presentazione

Gli sviluppi della scienza dei materiali hanno offerto, negli ultimi anni, un esempio significativo di come il cammino parallelo di ricerca di base e sviluppi tecnologici ha portato al raggiungimento di obiettivi fondamentali in un nuovo campo della ricerca, detto *nanoscienza*.

I modelli tradizionali della fisica dei materiali presuppongono lunghezze tipiche generalmente maggiori o eguali di 100 nm. La maggior parte degli studi fatti fino agli inizi degli anni '80 hanno riguardato proprietà di materiali bulk o di singole molecole. Lo studio di sistemi con dimensioni intermedie (inferiori a quelle critiche) come clusters di atomi, si è sviluppato a partire da quando l'invenzione di nuovi strumenti capaci di esplorare la materia su scale di pochi nm e, allo stesso tempo, l'introduzione di nuove tecniche di manipolazione della materia alle stesse scale, aprirono la strada verso nuove frontiere della scienza dei materiali.

L'essenza della nanotecnologia consiste nella capacità di manipolare la materia a livello atomico, realizzando sistemi in cui il numero e/o la posizione dei singoli atomi possono essere cambiati in modo controllato. La maggior parte degli sforzi tecnologici è stata volta proprio al raggiungimento del controllo di strutture e dispositivi a livello atomico e molecolare e, contemporaneamente, all'utilizzo di tali sistemi in modo efficiente. Dal punto di vista della ricerca di base, è diventato chiaro che le proprietà di questi nuovi sistemi nanometrici o *nanostrutture* non possono essere predette soltando conoscendo quello che accade su scale di lunghezza molto maggiori. Gran parte dell'interesse dato a questo nuovo campo della ricerca scaturisce proprio dalla considerazione che riducendo le dimensioni compaiono nuovi fenomeni legati al confinamento quantistico. La realizzazione e lo studio di nuovi sis-

temi come “quantum dots”, fili quantici, films sottili, nanotubi di carbonio, strutture a base di DNA, emettitori di luce laser, etc. hanno mostrato proprietà uniche, del tutto assenti in sistemi “tradizionali”. E le possibili applicazioni vanno dalla fisica alla biologia alla chimica, spesso senza la possibilità di distinguere fra esse.

Uno degli aspetti più studiati delle nanostrutture è il fatto che riducendo le dimensioni, molte proprietà fisiche (ottiche, di trasporto, etc.) diventano fortemente dipendenti dalla dimensione, dando luogo ad un ampio spettro di applicazioni. La possibilità di “accordare” la risposta del sistema con le dimensioni ha l'obiettivo tecnologico di progettare le proprietà del dispositivi, realizzando in questo modo sistemi adatti ad applicazioni differenti soltanto variando il numero, le specie e le posizioni di singoli atomi e/o molecole.

Questi enormi, rapidissimi progressi hanno permesso un controllo completo non soltanto sulle dimensioni ma anche sulla forma. Recentemente, la fabbricazione di quantum dots di geometria ellissoidale ha mostrato che la possibilità di accordare la risposta del sistema con le dimensioni può essere inteso in maniera più allargata, cioè esteso ad altre, interessanti proprietà come la polarizzazione della radiazione emessa al variare dell'anisotropia del sistema.

Questo lavoro di tesi è volto a dare un contributo teorico alla gran quantità di studi fatti sui nanosistemi, studiando come la forma può modificarne le proprietà fisiche rilevanti.

Il capitolo 1 è dedicato ad una breve rassegna sulla ricerca sperimentale su questi nuovi sistemi, illustrando alcuni punti importanti riguardo la loro fabbricazione e le loro proprietà ottiche e di trasporto.

Il capitolo 2 è incentrato sullo studio dei sistemi anisotropi, con particolare riguardo alla dipendenza delle proprietà ottiche dall'anisotropia della nanostruttura. L'equazione di Schrödinger a massa efficace è stata risolta esattamente all'interno di un quantum dot ellissoidale, per mostrare le caratteristiche dello spettro di singola particella direttamente legate alla perdita della simmetria sferica. L'analisi di tale spettro dimostra che le proprietà ottiche nell'infrarosso vengono modificate rispetto al caso sferico, mostrando una forte relazione fra la geometria del sistema e la polarizzazione della radiazione assorbita o emessa. Sono stati studiati, inoltre, effetti di correlazione

a due particelle mostrando come la configurazione spaziale e l'energia totale del sistema risultano funzioni delle dimensioni della nanostruttura e della sua geometria.

Il quantum dot ellissoidale è una delle poche eccezioni in cui, anche se nell'approccio più semplice (cioè l'approssimazione a massa efficace), è possibile esibire una soluzione esatta. Per un sistema di forma arbitraria, il problema diventa molto più complicato, in particolare nel caso in cui è necessario tenere in conto la barriera di potenziale finita ai bordi della nanostruttura. Questo problema diventa di particolare interesse se si pensa all'interazione di tali strutture con un ambiente esterno. Infatti, riducendo le dimensioni il decadimento della funzione d'onda di un elettrone o di una buca presenti nella nanostruttura all'esterno di essa diventa sempre più rilevante. Ci si aspetta che la sovrapposizione fra questa funzione d'onda e quella di una molecola esterna che abbia un ruolo chiave nella reazione della nanostruttura con l'ambiente esterno e, quindi, nelle applicazioni sensoristiche. Per trattare sistemi più complicati, è stato elaborato un approccio variazionale che include la barriera di potenziale finita al bordo. Il metodo, che è l'oggetto del capitolo 3, è stato applicato al caso del silicio poroso. Questo materiale ha ricevuto un largo interesse negli ultimi anni poiché il processo di fabbricazione porta ad un sistema eterogeneo che appare come un insieme di fili quantici e quantum dots. L'effetto principale sulle proprietà fisiche è il forte incremento dell'emissione di fotoluminescenza rispetto al silicio bulk. La struttura complicata di tale materiale è stata schematizzata tramite un modello geometrico che consiste in un insieme di fili quantici deformati indipendenti. Nell'ambito di tale modello, l'approccio variazionale è stato utilizzato per spiegare una larga classe di dati sperimentali osservati per il silicio poroso. Sono stati interpretati, in particolare, i risultati riguardo agli spettri di emissione e quelli di assorbimento, mostrando una possibile spiegazione della differenza osservata fra i rispettivi picchi (Stokes shift). Sono state studiate, inoltre, le proprietà del silicio poroso in presenza di un ambiente esterno, mostrando come il quenching ed il red-shift della fotoluminescenza in presenza di ossigeno possano essere interpretati utilizzando l'approccio variazionale.

Il capitolo 4, infine, è dedicato all'analisi di un ulteriore effetto legato alla fisica delle superfici in presenza di deformazioni di scala nanometrica.

Viene mostrato come sotto condizioni opportune una nuova classe di stati di superficie, demominati *stati topologici di superficie*, può essere individuata per superfici a curvatura variabile. Il moto di una particella nelle vicinanze di una superficie curva può dar luogo a stati quantici localizzati sui punti della superficie in cui la curvatura massima e quella minima hanno la loro differenza massima. Questo ha un interesse particolare poiché la presenza di tali stati potrebbe significare un incremento della reattività di superficie verso un ambiente esterno.

A pag. 8 è possibile trovare la lista degli articoli e dei proceedings di conferenze in cui il lavoro presentato in questa tesi è stato pubblicato.

Introduction

Materials science developments in the last years have offered a significant example on how the interplay between basic research and technology has lead to the achievement of fundamental goals within a new field of research, named *nanoscience*.

Traditional models in the materials science involve critical lengths generally of the order or larger than 100 nm. Most of the studies done until the 1980s concerned either bulk material or single-molecule properties, while systems with intermediate sizes, like atom clusters, were not studied at all. The invention of new instruments able to explore the matter down to a scale of a few nm and at the same time the introduction of novel techniques for the matter manipulation at the same scale, aroused the interest of many scientists in what could happen for sizes less than the critical lengths.

The essence of nanotechnology is the ability to work at atomic level, namely the assembly of systems in which the number and/or the position of single atoms can be varied in a controlled way. Most of the technological efforts have been focused just in gaining control of structures and devices at atomic and molecular level as well as in reaching efficient manipulation and use of such systems. On the other hand it has become very clear that the properties of these novel nanometric structures or *nanostructures* cannot be predicted just by knowing what it happens at very large scales. Most of the interest given to this new research world is due just to the consideration that the small size gives rise to new phenomena related to quantum confinement and inter-facial properties. New systems such as quantum dots, quantum wires, thin films, carbon nanotubes, DNA-based structures, laser emitters, etc. have been realized and studied, showing unique properties,

completely absent in "traditional" systems. And the possible applications go from physics to biology to chemistry, often without the possibility of distinguishing between them.

One of the most studied aspects of nanostructures is that on reducing the dimensions, many physical (optical, transport, etc.) properties become strongly dependent on the size, giving rise to a wide range of applications. The possibility of tuning the system response with the dimension has the very challenging technological goal of "designing" device properties, realizing in this way systems suitable to different applications just by varying the number, the species and the positions of single atoms and/or molecules.

These enormous, quick progresses have allowed a complete control not only on the dimensions, but also on the shape. Very recently, the fabrication of anisotropic, shape-controlled quantum dots has shown how the possibility of tuning the system response with the dimensions can be intended in a larger way, namely extended to other, interesting features, as the polarization of the emitted radiation.

This thesis work is intended to give a theoretical contribution to the large amount of studies done on nanosystems, studying how the shape can modify their properties. Just because the goals achieved up to now have shown how the comprehension of the underlying principles and the technological progress run very closely to each other, chapter 1 is dedicated to a short review of the experimental research on these novel systems, illustrating (very shortly) some important points about both their fabrication and their optical and transport properties.

Since the most studied geometry for quantum dots is the spherical one, some fundamental concepts known in that case have been extended to an ellipsoid geometry. The effective-mass Schrödinger equation has been exactly solved within an ellipsoid quantum dot, in order to show the single-particle spectrum features which are explicitly related to the loss of the full spherical symmetry. The implications for the infrared optical properties have been investigated, stressing the strong relation between the shape and the response to polarized light. Moreover, two-particle correlation effects have been studied, showing how they change with the system geometry. Dielectric effects, related to the dielectric mismatch between the dot and the surrounding medium

have been included and discussed. This is the topic of chapter 2.

The ellipsoid quantum dot is one of the few exceptions in which, even in the simplest approach (namely, the effective-mass approximation) an exact solution can be attempted for. For an arbitrarily shaped system, the problem becomes much more complicated, mostly if finite boundary conditions at the nanostructure boundaries have to be considered. This problem becomes very interesting if we think to the interaction of such structures with an external environment. In fact, the small dimensions give rise to the wave function decay outside the nanostructure. The overlap between this wave function and that of an incoming molecule is expected to have a central role in the reaction of the nanostructure with the external environment and, therefore, in sensor applications. In order to treat more complicated systems a variational approach has been built up, with the inclusion of a finite potential barrier at the boundaries. The method, presented in chapter 3, has been applied to the case of porous silicon. This material has received a wide interest in the last years because the fabrication process leads to an heterogeneous system which appears as a collection of quantum wires and dots. The main effect on the physical properties is that a strong enhancement of the photoluminescence emission is observed with respect to bulk silicon. Within a geometrical model which schematizes the very complicated structure of such material as a collection of independent deformed quantum wires, the variational approach has been used to explain a large class of experimental data which have been observed for porous silicon.

Finally, chapter 4 analyzes a further effect related to surface physics in presence of deformations with nanometric size. It is shown that under suitable conditions a new class of surface states, named *topological surface states*, can be found if surfaces with variable curvature are considered. The motion of a particle in the neighbourhood of such surface can give rise to quantum states localized on the surface points where the maximum and minimum curvature have their maximum difference. This point has a particular interest because the presence of such states could mean an enhancement of the surface reactivity towards an external environment.

The work presented in this thesis has been published in the following papers:

1. *Shape effects on the one- and two-electron ground state in ellipsoidal quantum dots*
   G. Cantele, D. Ninno and G. Iadonisi, *Phys. Rev. B* **64**, 125325-1 (2001).

2. *Calculation of the infrared optical transitions in semiconductor ellipsoidal quantum dots*
   G. Cantele, D. Ninno and G. Iadonisi, *Nanoletters* **1**, 121 (2001).

3. *Impurity and topological surface states in porous silicon*
   D. Ninno, F. Buonocore, G. Cantele, and G. Iadonisi, *phys. stat. sol. a* **182**, 285 (2000).

4. *A theory for semiconductor nanostructure reactivity to gas environment*
   D. Ninno, G. Iadonisi, F. Buonocore, G. Cantele and G. Di Francia, *Sensors and Actuators B* **68**, 17 (2000).

5. *Confined states in ellipsoidal quantum dots*
   G. Cantele, D. Ninno and G. Iadonisi, *J. Phys.: Condens. Matter* **12**, 9019 (2000).

6. *Topological surface states in deformed quantum wires*
   G. Cantele, D. Ninno and G. Iadonisi, *Phys. Rev. B* **61**, 13730 (2000).

and in the following conference proceedings:

1. *Chemical sensing with nanostructures*
   G. Di Francia, M. L. Addonizio, G. Cantele, M. Della Noce, V. La Ferrara, L. Lancellotti, P. Morvillo, D. Ninno and L.Quercia, in: *Proceedings of the 6th National Conference on Sensors and Microsystems*, Pisa, 5-7 February, 2001, edited by C. Di Natale, A. D'Amico and P. Siciliano (World Scientific, Singapore, 2001).

2. *The role of quantum confinement in porous silicon gas sensors*
   D. Ninno, F. Buonocore, G. Cantele, G Iadonisi and G. Di Francia, in: *Proceedings of the 5th Italian Conference Extended to Mediterranean Countries on Sensors and Microsystems*, edited by C. Di Natale, A. D'Amico and P. Siciliano (World Scientific, Singapore, 2000).

3. *Calculation of the confinement energies of a particle in deformed nanostructures*
   F. Buonocore and G. Cantele, in: *Porous Semiconductors - Science and Technology*, edited by V. Parkhutik and L. Canham (Rayton Impresores, Valencia, Spain, 2000).

4. *Localized, impurity and topological surface states in porous silicon*
   D. Ninno, G. Iadonisi, F. Buonocore and G. Cantele, in: *Porous Semiconductors - Science and Technology*, edited by V. Parkhutik and L. Canham (Rayton Impresores, Valencia, Spain, 2000).

Chapter 1

The Physics of nanostructures

The wide interest in studying the materials properties at nanometric scale has grown up in the last years. It is in practice commonly accepted that the nanoscience developments have opened new fields in the materials research, but many more are expected to come in the future. A wide potential is perceived in the study of nanometric structures, which has meant the increase of the investments involved in such researches in all the advanced countries. The statement which most effectively highlights it is from the US President's Advisor for Science and Technology [1]:

> "If I were asked for an area of science and engineering that will most likely produce the breakthroughs of tomorrow, I would point to nanoscale science and engineering".

Just to give an example, the US government has invested for the 2001 financial year about $500 million, 83% more than 2000.

The employment of so many human and economic resources can only be explained by considering that as the dimensions are reduced down to nanometric scale, novel properties of matter appear, which makes nanostructures suitable for novel and revolutionary industrial applications as well as one of the most exciting fields of modern science. It is not a case that this field has been defined as "leading to the next industrial revolution" [1].

In this chapter a general overview of the main aspects involved in the physics of nanostructures is given. The experimental progresses done in both

the fabrication of nanometric materials and the investigation of their properties will be described, giving just a few examples of how recent developments of the materials science have lead to the possibility of exploring the matter down to atomic resolution (sec. 1.1). The novel properties which come out as the dimensions are reduced are discussed (sec. 1.2), giving relevance in particular to their present or future applications, such as the possibility of counting electrons one by one.

1.1 Nanoscience technology

The possibility of manipulating very small structures has given new perspectives for the devices fabrication industry, allowing both the improvement of the devices performances (the reduction of the dimensions has meant faster devices, lower heat dissipation, etc.) and the fabrication of new nanostructure-based devices such as single-electron transistors [2–7], quantum dots lasers [8–10], storage devices [11] and fluorescence markers [12–14]. It must be pointed out that the wide development of nanoscience in the last years cannot be viewed simply as the natural evolution of miniaturization engineering and microelectronics industry. Novel and exciting physical, chemical and biological properties occur at nanometric scale. As the structure dimensions are reduced below about one hundred nanometres, that is structures with a low number of atoms (compared with that of bulk crystals) are concerned, *quantum confinement* effects on the electrons and holes motion appear. This can be explained only in the framework of quantum mechanics. In fact, as the particle de Broglie wave length becomes comparable with the structure dimensions, quantum effects become relevant, giving rise to the appearance of a discrete spectrum of levels or of a mini-band structure depending on the system dimensionality. Starting from a three-dimensional bulk structure and by reducing one, two or all three dimensions, two-dimensional, one-dimensional and zero-dimensional systems are obtained. They are usually referred to respectively as quantum wells, quantum wires and quantum dots. For these last ones atomic-like spectra are observed, which has gained for such structures the name of *artificial atoms* [15–25]. It is interesting to note how the

lower dimensionality changes the density of states. This is shown in Fig. 1.1, where the bulk semiconductor density of states is compared with that of low-dimensionality systems. Because in this thesis work the main interest is in studying quantum dots properties, what experimentally comes out if electrons and/or holes quantum confinement in all three dimensions is achieved will be illustrated more in detail.

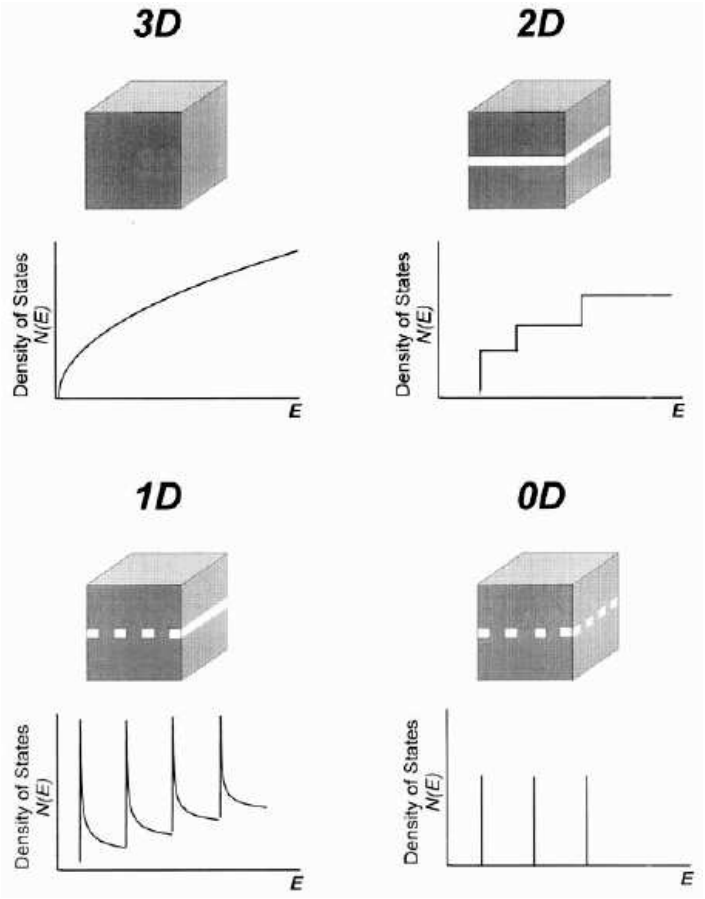

Figure 1.1: A schematic diagram illustrating the electronic density of states that occurs as dimensionality is varied from 3D to 0D, assuming free electrons. It is interesting to note that for a three-dimensional semiconductor the density of states has a $\sqrt{E}$ dependence [26] while for 2D systems a step function is obtained, for 1D systems a $1/\sqrt{E}$ dependence and for 0D systems a δ-function-like dependence.

1.1.1 Imaging the world down to atomic resolution

The possibility of exploring new, fascinating properties of matter at nanometric scale and at the same time of using them for novel applications such as information storage was first pointed out by R. P. Feynmann in his 1959 lecture at the annual meeting of the American Physical Society at the California Institute of Technology [27]. The "visionary" title of this lecture was "*There is a plenty of room at the bottom*". Here he clearly expressed the need of new technologies which could act as "eyes" and "fingers" in the nanoworld. This technology was realized in the early 1980s with the invention of the scanning electron microscopy (STM), an instrument which measures the quantum tunnel current flowing between a metallic tip and a conducting sample to give surface topography at atomic scale. Since then, other powerful scanning probe instruments such as the atomic force microscope (AFM), the magnetic force microscope (MFM) and the scanning near-field optical microscope (SNOM) have been developed [28].

The possibility of realizing atomically resolved surface images has meant the first step towards the development of nanoscience and nanotechnology. A further, significant contribution came just from these scanning probe techniques, which allowed the possibility of manipulating and arranging the mat-

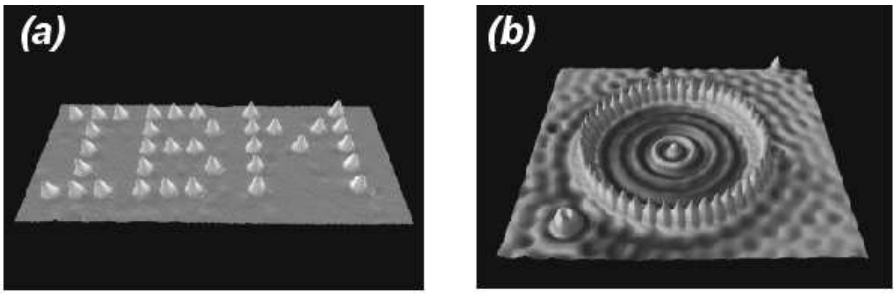

Figure 1.2: (a) Individual Xe atoms positioned on a Ni surface at $4K$ to form the *IBM* logo (from ref. [29]). (b) A quantum corral formed by Fe atoms on a Cu(111) surface. The rings represent the corral eigenstate of the Cu(111) electrons confined within the circular arrangement of Fe atoms (from ref. [30]).

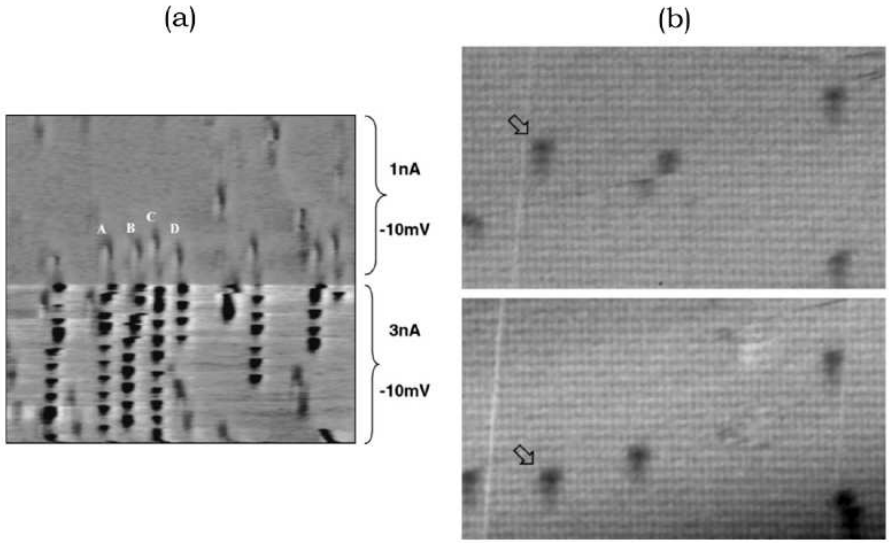

Figure 1.3: (a) 6 nm×6 nm STM image of Br on Cu(100). The tracks in the lower half (higher tunnel current) are atoms hopping from site to site. When the tunnel current is reduced (upper half) the Br atoms stop moving (as those marked A,B,C and D). (b) Controlled positioning of a single atom at room temperature. The lower image is taken before and the upper image after a manipulation stroke on the arrowed atom (from ref. [31]).

ter at so small scales [28]. For example, with STM the controlled positioning of atoms on surfaces by controlling the interaction between the tip and the surface has been realized. Some examples are given in Figs. 1.2 and 1.3.

In the same way molecules have been assembled by directly bringing single atoms and/or molecules close to each other [32].

1.1.2 Nanoclusters fabrication

Scanning probe techniques are not the only way by which to arrange the matter at so small scales. Chemical synthesis of nanoparticles is nowadays a commonly used technique for assembling atoms or molecules [28]. The strategy is based on the so-called *bottom-up* approach, which means that the starting point are the constituent elements which via suitable chemical

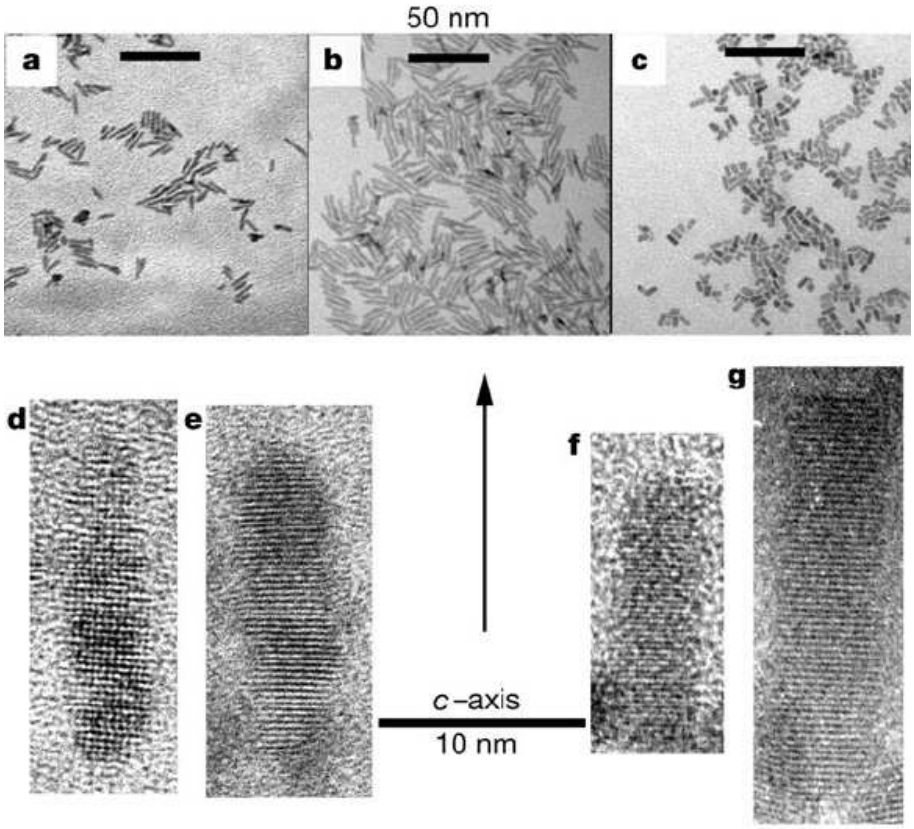

Figure 1.4: (a-c) TEM images of three quantum-rod samples with different sizes and aspect ratios. (d-g) High resolution TEM images of four quantum rods (from ref. [33]).

reactions are assembled together (quantum dots are viewed as extremely large molecules or colloids). Colloidal synthesis of semiconductor clusters has been widely explored. Quantum dots fabricated with these *bottom-up* techniques have dimensions variable from a nearly molecular regime ($\simeq$ 1 nm) up to about 50 nm. It has been shown to be a very powerful technique, being able of controlling nanoclusters size and, very recently, shape. In fact, synthesis of rod-, arrow-, teardrop- and tetrapod-shaped CdSe [33, 34] and rod-like Co [35] nanocrystals has been achieved, showing surprising flexibility in anisotropically controlling the growth kinetic (*oriented attachment*). The

nanorods aspect ratio has been varied from one to one (nearly spherical quantum dots) up to ten to one (long nanorods). Some spectacular images are shown in Figs. 1.4, 1.5, 1.6.

Within this field perhaps the most exciting perspective is the propensity for *self-assembling*, *self-organization* and *self-replication* of natural biological systems such as amino acids, nucleic acids (DNA, RNA) and viruses [28, 36–39]. The application of molecular assembly processes to nanostructures synthesis is just one example of how, at nanometric scale, physics, engineering, biology and chemistry have no longer a neat boundary, the only possible approach being multi-disciplinary. This is one of the most challenging applications of nanostructures, the ultimate goal being the realization of functional bio-inorganic structures biologically self-assembled [40]. An example is shown in Fig. 1.7, where TEM images of polymer 1-Thy-Au aggregates

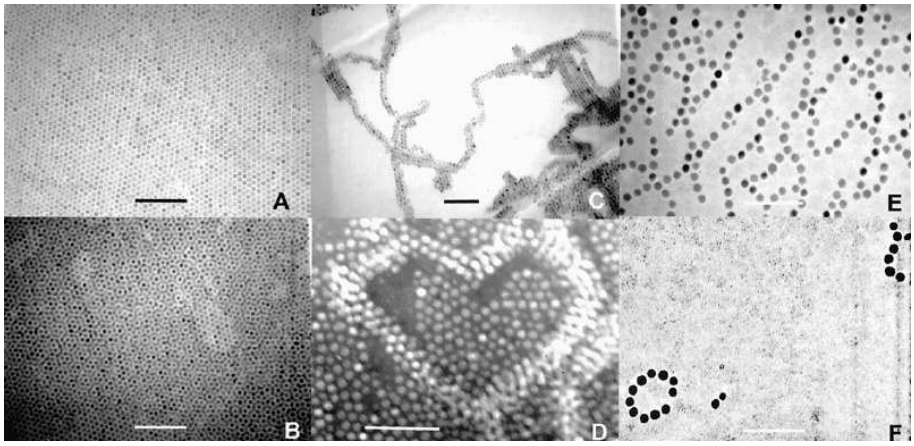

Figure 1.5: (a-f) Images of Co spherical nanoparticles prepared by colloidal synthesis, by using different mixtures of reactants (from ref. [35]). The bars correspond to 100 nm. Spherical particles self-assemble into a hexagonal superlattice (a-b). Due to magnetic interactions, under suitable reaction conditions the nanocrystals form closed loops to minimize their magnetic interaction (e-f). A transition region between the two different kinds of arrangement is also observed, with a mixture of hexagonal monolayer and closed loops (c-d).

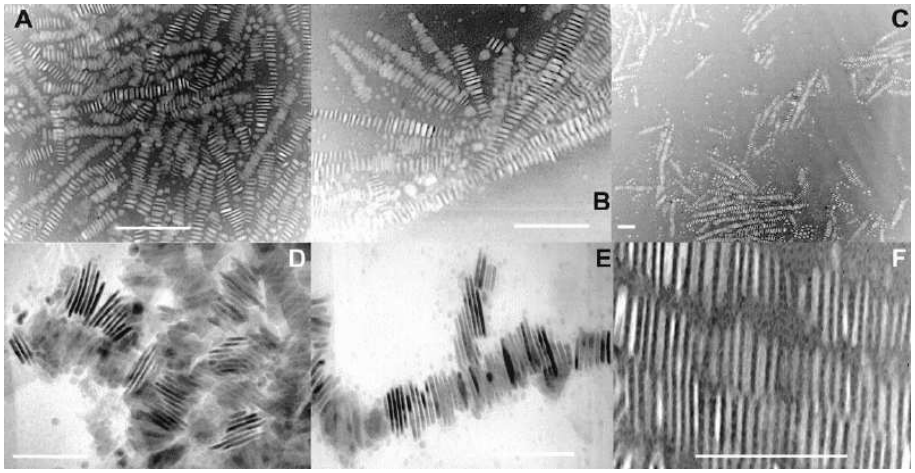

Figure 1.6: (a-f) Assemblies of hpc-Co magnetic nanorods prepared by colloidal synthesis, by using different mixtures of reactants (from ref. [35]). The bars correspond to 100 nm. Long ribbons of rods are formed, whose length is determined by the magnetic properties of the single rods.

formed at different temperatures are shown. The temperature strongly affects the morphology of the resulting ensembles, which ranges from discrete structures observed at the highest temperature (23 ^{o}C) to micro-scale discrete spherical particles, consisting of 10^5-10^6 individual Thy-Au units observed at the lowest temperature (-20 ^{o}C). The intermediate temperature 10 ^{o}C corresponds to networks formation, which suggests that these networks are an intermediate process in the formation of the giant assemblies at -20 ^{o}C.

The fabrication of nanostructures can be also approached from a completely different point of view, in which the nanometric dimensions are obtained by gradually reducing bulk crystal dimensionality (*top-down* approach) [17, 23, 28]. These techniques are usually based on combinations of molecular beam epitaxy, electron beam or x-ray lithography and etching and give quantum dots in the size regime of 1 μm down to 10 nm. A typical example is given by a GaAs thin layer (whose thickness must be less than the carrier de Broglie wave length) embedded in two layers of $Al_xGa_{1-x}As$. The controlled composition of the tertiary alloy allows the tuning of the band gap

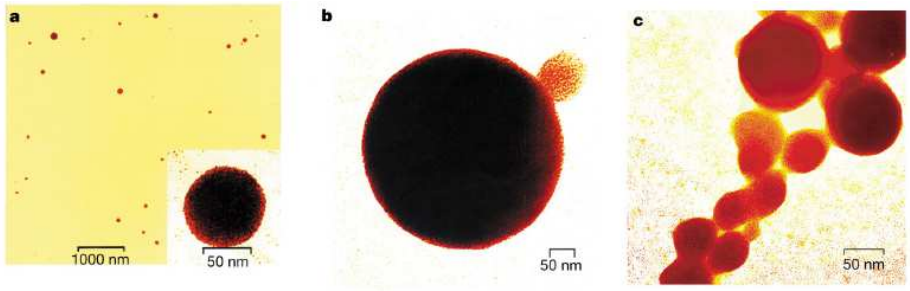

Figure 1.7: TEM images of polymer 1-Thy-Au aggregates formed at (a) 23 ^{o}C, (b) -20 ^{o}C and (c) 10 ^{o}C (from ref. [38]).

mismatch between the two materials, which gives rise to a quantum well potential and, therefore, to the quantum confinement of carriers. Lithography and etching can then be used to further confinement to one (quantum wires) or zero (quantum dots) dimensions. The application of these techniques to lattice-mismatched materials has also lead to the discovery that under suitable conditions nanometric-scale islands with a narrow size distribution form, showing their tendency for self-assembling [23, 28].

1.2 Electrons and holes in artificial atoms and molecules

Quantum dots are small nanocrystals whose dimensions usually are in the range 1-100 nm, which corresponds to 10^3-10^6 lattice atoms. The number of sites of a spherical quantum dot as a function of the dot diameter is shown in Fig. 1.8. An fcc lattice with zincoblende structure has been assumed. The inset shows an HREM image of a nearly spherical Si nanoparticle covered by an amorphous shell (from ref. [41]). The main feature of such systems is the fact that the electron or hole motion can be described by atomic-like wave functions and energy levels. Because of the uncertainty principle the spacing between these levels is of the order of $\hbar^2/MR^2$ if M is the particle mass and R the typical dot dimension. The goal in the fabrication of

quantum dots is that physical phenomena observed for atoms, such as light emission, can be reproduced and tuned by artificially controlling the material properties (such as shape, size, composition, etc.). The most evident example is given by the strongly size-dependent optical properties achieved as the dot dimensions are reduced [16, 25]. The energy gap shifts towards energies higher than the correspondent bulk value, giving rise to size-tunable luminescence at room temperature. At the same time, a strong enhancement of the volume-normalized oscillator strength associated to the allowed transitions is observed. The explanation is given by the fact that for bulk crystals both the particle energy and its crystal momentum can be precisely defined, while its position cannot. As the crystal dimensions are reduced, the particle en-

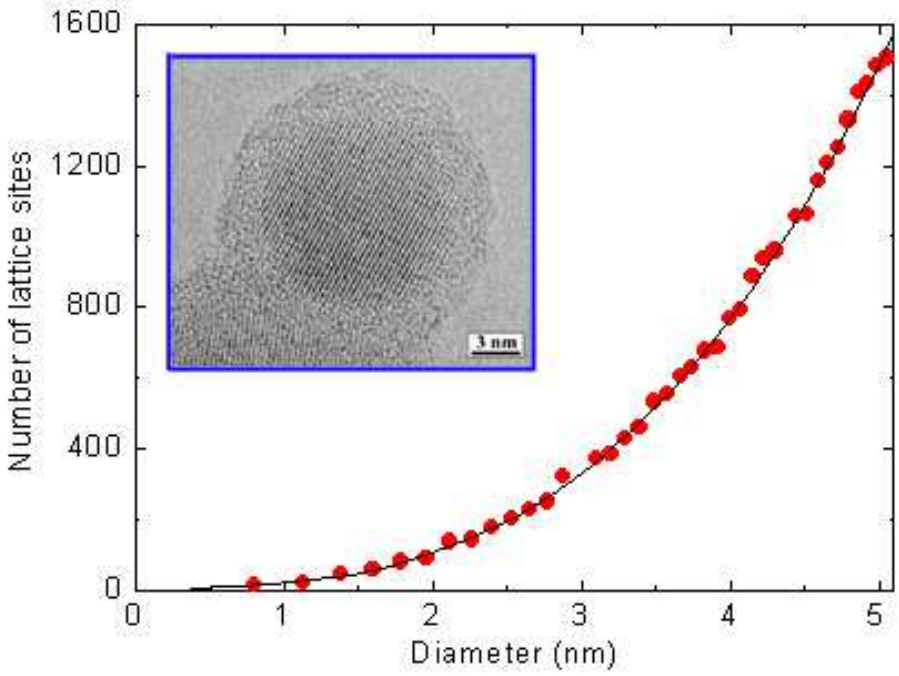

Figure 1.8: The number of sites in a spherical quantum dot as a function of the dot diameter. An fcc lattice with zincoblende structure has been assumed. The inset shows an HREM image of a nearly spherical Si nanoparticle covered by an amorphous shell (from ref. [41]).

ergy can be still defined but, because of the uncertainty principle, the spatial localization imply that the crystal momentum can no longer be precisely defined. Therefore, the nanocrystal atomic-like eigenfunctions may be viewed as the superposition of many bulk momentum states and the energy spectrum changes from continuous bands to discrete levels. A direct consequence is that the oscillator strengths, rather than being distributed over a continuum of states as for bulk semiconductors, become concentrated over sharp transitions [42–49]. The optical line-widths of single quantum dots are orders of magnitude narrower than those observed in ensemble measurements, approaching the natural linewidths expected from radiative lifetimes [50]. This is shown in Fig. 1.9, where high spatial resolution cathodoluminescence of InAs quantum dots at 20 K is shown. This measurement unambiguously gives the spectroscopic evidence of zero-dimensional δ-function electronic density of states.

Therefore, quantum dots have an *excitation spectrum* (that is, the optical spectrum at fixed number of electrons) quite similar to that of atoms.

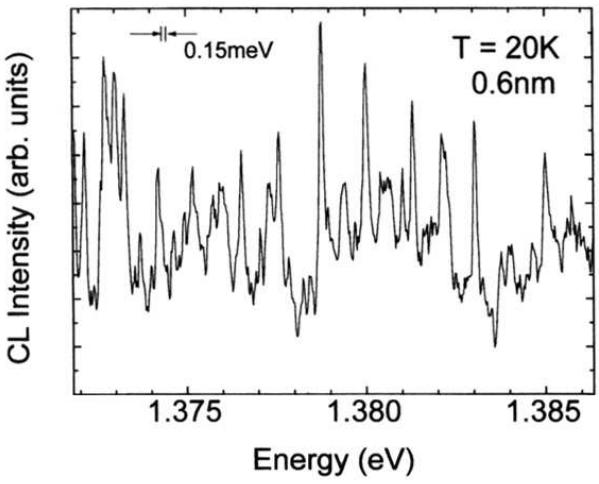

Figure 1.9: High spatial resolution cathodoluminescence spectrum for InAs quantum dots at 20 K (from ref. [43]). Ultra sharp lines (whose width is limited by the spectral resolution of the experimental setup), in absence of thermal broadening, clearly reveal the quantum confined spectrum.

The new feature is the possibility of tuning with size the spacing between the quantum confined levels. A typical example is given in Fig. 1.10a, where size- and material-dependent emission spectra of several semiconductor nanocrystals are shown. The blue, green and red sets of curves correspond respectively to CdSe, InP and InAs nanocrystals. Within each set, different curves correspond to different nanocrystal diameters, increasing from right to left. Moreover, Fig. 1.10(b) shows a true-colour image of a series of nanocrystal probes in aqueous buffer, all illuminated simultaneously with a hand-held ultraviolet lamp. A further example is given in Fig. 1.11, where the UV-visible spectrum is shown, for CdSe quantum dots, for different sizes. The blue-shift of the adsorption edge (corresponding to the quantum dot energy gap) on reducing the dot size clearly comes out.

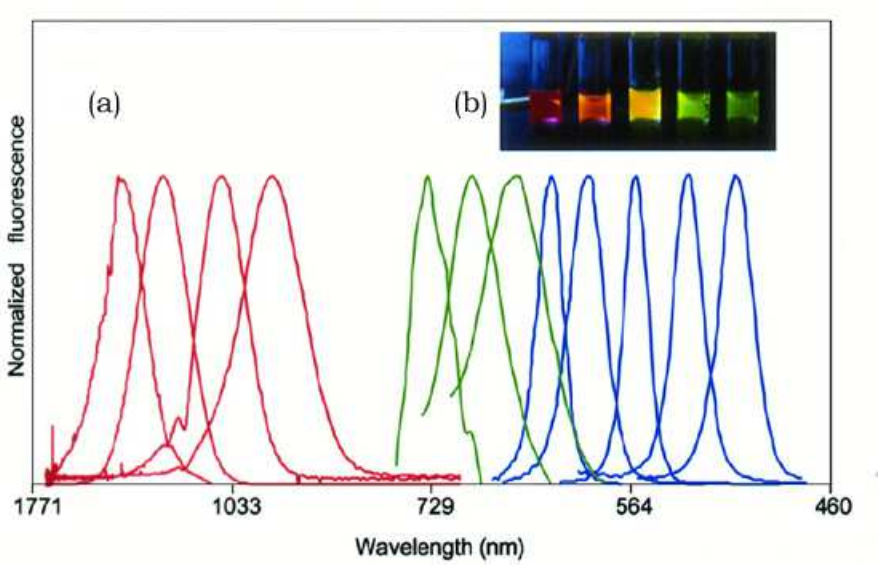

Figure 1.10: (a) Emission spectra of CdSe (blue curves), InP (green curves) and InAs (red curves) nanocrystals with different diameters. Within each set of curves, the size increases from right to left. (b) A true-colour image of a series of nanocrystal probes in aqueous buffer, all illuminated simultaneously with a hand-held ultraviolet lamp (from ref. [13]).

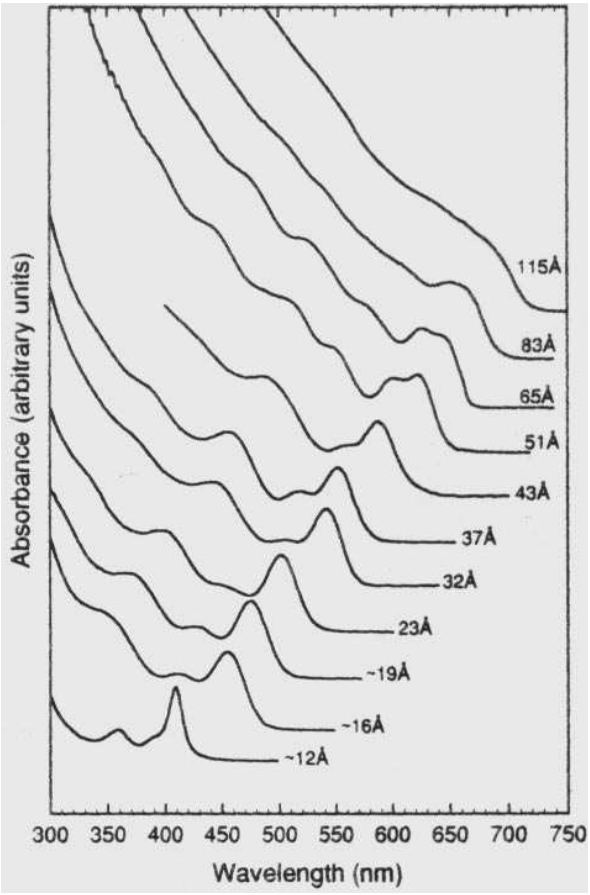

Figure 1.11: UV-visible spectrum for CdSe nanocrystals with different dimensions (from ref. [51]). The blue-shift of the band edge on decreasing the dimensions is clearly visible.

The size-dependence of the quantum dots spectrum gives, as we have seen, the possibility of tuning their optical properties, which has made these objects suitable, for example, to realize nanocrystal-based light emitting diodes (LEDs). Atomic-like features can be observed also for the electron or hole wave function. This has been brought out by magneto-tunnelling spectroscopy (which is not STM-based and can be regarded as the analog of STM in the momentum space). This technique has been applied to pyrami-

dal self-assembled quantum dots [52], showing the elliptical symmetry of the ground state and the characteristic lobes of higher energy states. The result is shown in Fig. 1.12.

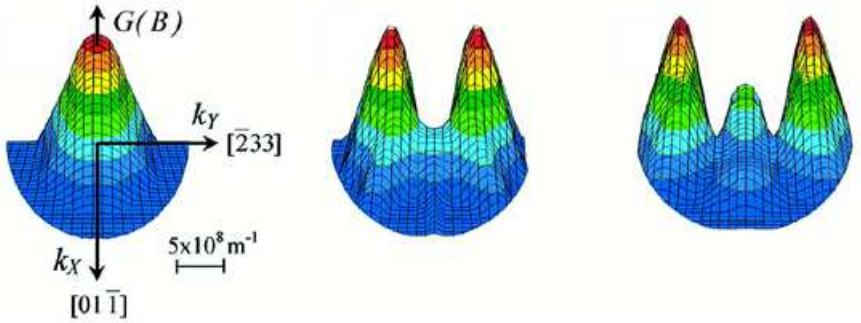

Figure 1.12: The magnetic field dependence of the differential conductance as obtained from magneto-tunnelling spectroscopy applied to InAs self-assembled quantum dots (from ref. [52]). It reproduces a map of the square modulus of the electron wave function Fourier transform. The elliptical symmetry of the ground state and the characteristic lobes of excited states clearly come out. The (x, y) plane corresponds to the basis of the pyramidal dot.

Quantum confinement effects play a central role in determining the transport properties of such structures as well. The most evident example is the introduction of electrons one by one in nanoclusters coupled to a source and drain electrodes. The single-electron properties of quantum dots [2–7, 53–58] have lead to the discovery of new, interesting effects such as *Coulomb blockade*. The basic idea is that the addition of a single electron to an N-electrons system, because of the Coulomb repulsion, requires a charging energy, which is analogous to the ionization energy for atoms, as shown in Fig. 1.13. In other words, the electron-electron repulsion results in a considerable energy cost for adding an extra electron charge and no current will flow until the voltage provides this energy. By varying the bias voltage between the electrodes, the device conductance and current show a peak structure, each peak corresponding to the transport of a single electron. This reflects the structure charging energy as a function of N, known as *addition spectrum*. It is

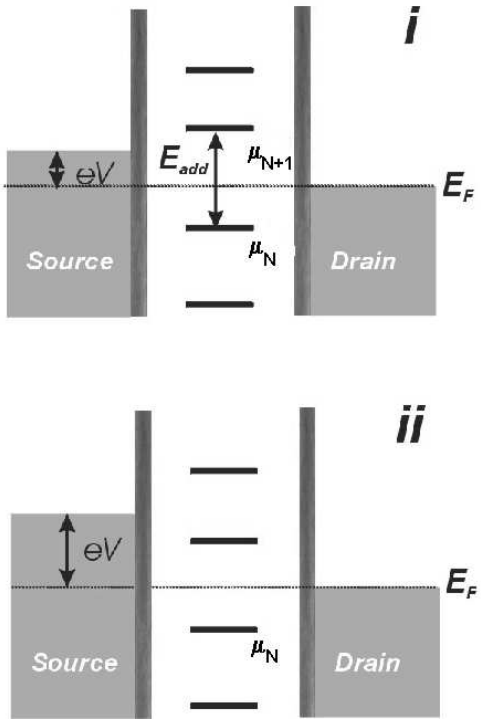

Figure 1.13: The scheme of a quantum dot coupled to source and drain electrodes, explaining the origin of Coulomb blockade. The Fermi level of the source is above that the drain source, the difference being eV if V is the bias voltage. The addition of an electron to the quantum dot filled with N electrons (i) requires that the source Fermi level is raised up to the quantum dot $(N+1)$-electrons chemical potential (ii). Sometimes the bias voltage (between the source and drain electrodes) is kept constant and the addition of single electrons is performed by using a gate voltage which allows the shift of the quantum dot energy levels with respect to the source and drain Fermi levels. Note that the source and drain electrodes can either be lithographically patterned electrodes or be formed by an STM tip and a substrate on which the quantum dot is located.

explained by considering that to add or remove an electron to/from the dot filled with N electrons, the source Fermi level must be raised up to or above

the $(N+1)$-electrons electrochemical potential or lowered down to or below the N electrons electrochemical potential. For intermediate values of the gate voltage electrons transport trough the tunnel junction can not occur. The Coulomb oscillations in the current vs the gate voltage are shown in Fig. 1.14c for a circular vertical quantum dot made from a double-barrier heterostructure (obtained by embedding the dot between two barriers which give quantum confinement in the vertical direction, as in Fig. 1.14a-b). Each oscillation corresponds to just one electron entering the dot. The addition spectrum of the dot is shown in the inset of the same figure. Let us note that the device shown in Fig. 1.14a-b has cylindrical symmetry. If the dot is approximated with a two-dimensional harmonic potential it is possible to show [56] that it gives rise to a shell structure (like for atoms) for which closed shells correspond to $2, 6, 12, \ldots$ electrons in the dot. The numbers in this sequence can be regarded as "magic" numbers for the two-dimensional harmonic potential. The addition spectrum in the inset of Fig. 1.14c shows addition energies unusually large just for $N = 2, 6, 12 \ldots$. Finally, the addition energy becomes larger as N decreases, due to the increasing of the Coulomb interaction. The shell structure of the addition spectrum explains the wide interest in the quantum dot applications as single-electron transistors. In fact, single-electron transistors are able to turn on and off each time their charge varies of just one unit, unlike commercial transistors which are able to turn on when many electrons are added to them. This gives, for example, a quantum dot-based method for counting electrons [59, 60]. Moreover, the sequential filling of the dot with electrons one by one allows the fabrication of artificial atoms analogous to the elements of the periodic table and reveals peaks in the charging energies which are nothing else than the well known Hund's rules for atoms [56, 61–64]. It is important to stress that the investigation of the atomic-like features of such structures can be performed both by fixing the number of electrons (excitation spectrum) or adding electrons one by one (addition spectrum). Nevertheless, measurements in which both features come out have also been done, as shown for example in Fig. 1.15. Here the scanning tunnelling microscopy and spectroscopy of a single InAs nanocrystal 3.2 nm in radius acquired at 4.2 K is shown. A series of discrete levels comes out. For tunnelling through conduction band levels

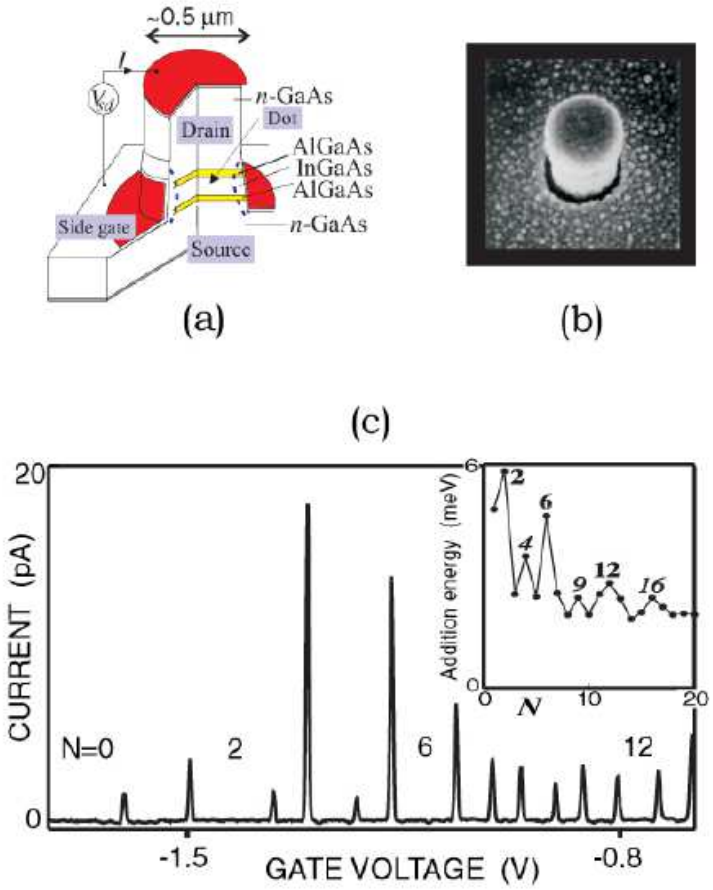

Figure 1.14: (a) Schematic diagram of a semiconductor heterostructure. The dot is located between the two AlGaAs barriers. Electrons can tunnel from occupied states in the drain via the dot to an empty state in the source. The source-drain voltage V_{sd} determines the difference in the Fermi energies between the two electrodes. The current is blocked when this energy window lies in-between two states in the dot (see also Fig. 1.13). (b) Scanning electron micrograph of a quantum dot heterostructure. (c) Coulomb oscillations in the current vs the gate voltage through a vertical quantum dot. Each oscillation period corresponds to the addition of just one electron in the dot. The distance between adjacent peaks corresponds to the addition energies shown in the inset (from refs. [56, 57]).

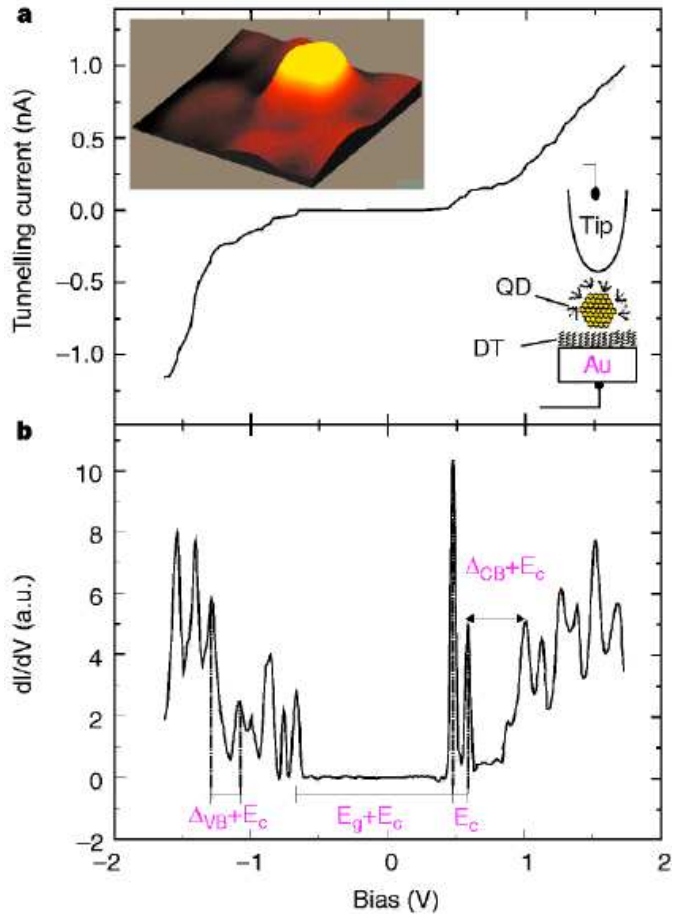

Figure 1.15: (a) Tunnelling I-V characteristic of a single InAs quantum dot 3.2 nm in radius acquired at 4.2 K. Single-electron tunnelling effects come out. The left inset show a 10×10 nm STM topographic image of the nanocrystal. The quantum dot is linked to a gold substrate by hexane dithiol molecule (DT), as shown in the right inset. (b) Tunnelling conductance spectrum, dI/dV, versus the bias voltage V. E_c is the single-electron charging energy, E_g the nanocrystal bandgap, and Δ_{VB} and Δ_{CB} the spacing between levels in valence and conduction band respectively (from ref. [65]).

(positive bias), first a doublet is observed, corresponding to the occupancy of the lowest conduction band confined state, the spacing between the two levels corresponding to the single-electron charging energy E_c. This is consistent with the degeneracy of the conduction-band ground state which has s character. By increasing the bias voltage, further electrons are added to the structure, resulting in the filling of the conduction band first excited state. This corresponds to the second group of six levels, consistently with the p character of the involved confined state. The addition of these electrons requires an energy given by the sum of E_c and the spacing between the two conduction band confined states. The spacing between the six p states is given just by E_c, being these state degenerate in the single-particle picture. The valence band filling (negative bias voltage) has a similar structure, even if in this case the confined levels multiplicities cannot directly be related to angular momentum degeneracies. This is a very clear evidence for atomic-like properties of quantum dots. The same shell structure is observed for excitons (electron-hole pairs) spectra, as shown for example in Fig. 1.16.

All these experimental evidences make the analogy between quantum dots and atoms quite strict. This analogy is made even stronger by observations of fine structure splittings and hyperfine shifts due to the spin of the electrons and nuclei [67–69], Zeeman splittings and Stark shifts due to magnetic [69–75] and electric fields [76]. But the strong correspondence between quantum dots and atoms can go still farther. In fact, two or more quantum dots can be coupled to form an *artificial molecule* [21, 77–87]. Bonding and anti-bonding states appear in the spectrum, just as for molecules. The ground state can be delocalized over the two or more dots, with the possibility of investigating the optical and transport properties of such structures as a function of the "interatomic" distance. A quantum dot molecule can be realized, for example, as the single-dot shown in Fig. 1.14a, except that the double barrier heterostructure is replaced by a triple barrier heterostructure. This is shown in Fig. 1.17a. The central barrier thickness can be varied, giving rise to a strong or weak coupling between the two dots. A gate voltage V_g is applied to investigate Coulomb-blockade effect, as explained previously. The vertical drain current I_d is measured as a function of the drain voltage V_d applied between the substrate and the top contact, and V_g. The addition spectrum reveals

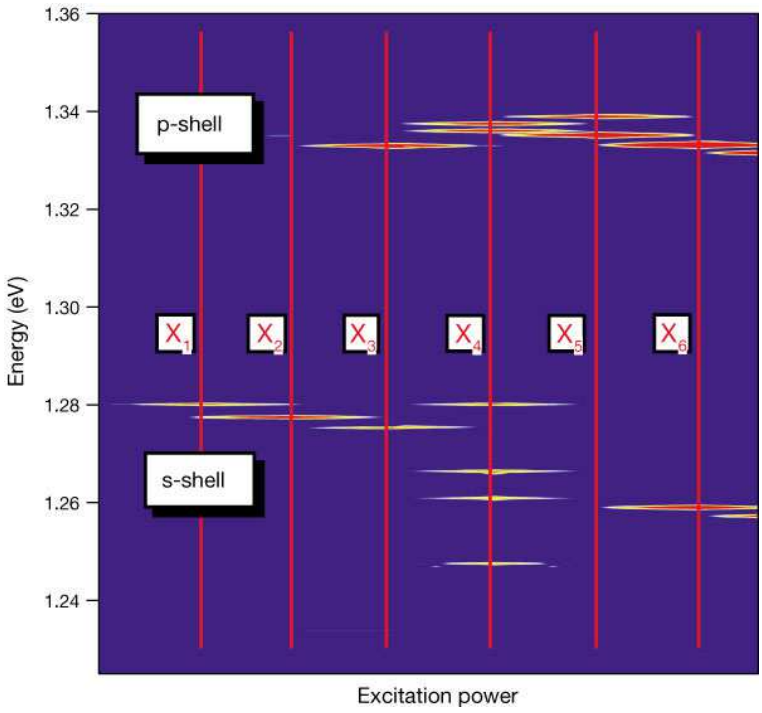

Figure 1.16: High excitation spectroscopy of $In_{0.60}Ga_{0.40}As$ quantum dots. The recombination processes of one up to six excitons clearly come out (from ref. [66]).

"magic" numbers which mark the complete filling of a shell, as shown in Fig. 1.17b. Moreover, "strongly" coupled dots give a Coulomb diamonds structure similar to that observed for the single dot [56] as observed in the grey-scale plot of the device differential conductance dI_d/dV_d in the (V_d, V_g) plane, as shown in Fig. 1.17c. Black (white) lines correspond to positive (negative) value of the differential conductance and identify bound and excited states. The grey diamond-shaped regions correspond to $I_d = 0$. The symmetry of the diamonds with respect to the bias direction corresponds to delocalized states over both the dots. This behaviour becomes much less marked for "weakly" coupled dots [86]. Evidences for quantum dots chains [88, 89] and solids [90] have also been shown. In Fig. 1.18 it is shown how faceted colloidal crystals 5 to 50 μm in size can be made from self-organization of CdSe quantum dots

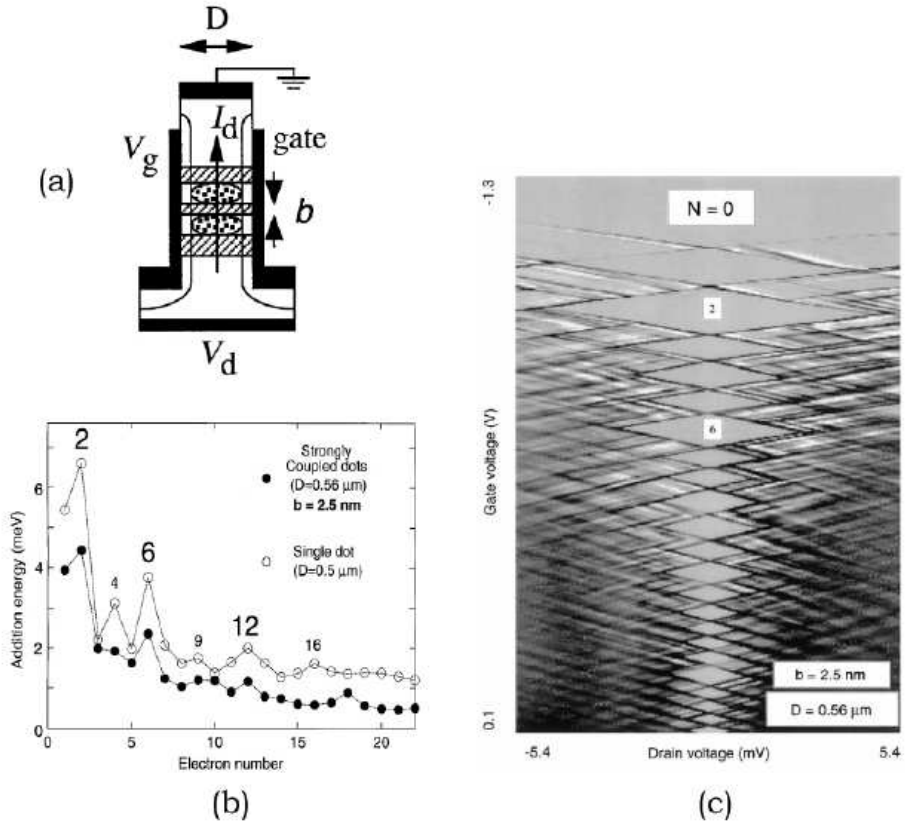

Figure 1.17: (a) A double-dot structure. The drain current I_d flows vertically as a response to the drain voltage V_d applied between the substrate and the grounded top contact, and the gate voltage V_g. (b) "Strongly" coupled double-dot addition spectrum. The single-dot addition spectrum is also shown for comparison. The previously discussed "magic" numbers can be recognized from the plot. (c) Gray-scale plot of the differential conductance dI_d/dV_d in the (V_d, V_g) plane for a "strongly" coupled double-dot. The diamonds structure clearly comes out near $V_d = 0$ mV (from ref. [86]).

2 nm in diameter. The optical spectra of close-packed CdSe quantum dots show evidence of both quantum confinement in the individual dots and inter-dot interaction [90]. Similarly, close-packed planar arrays of self-assembling

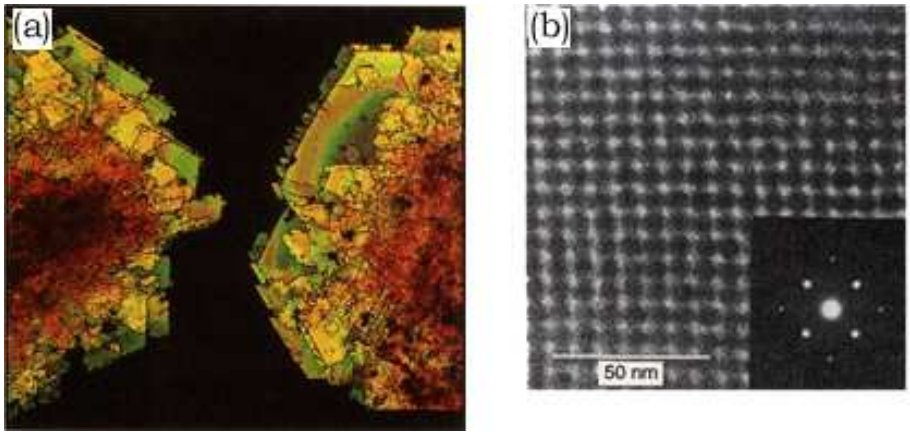

Figure 1.18: (a) A dark-field optical micrograph of a faceted colloidal superlattice formed by self-organization of CdSe quantum dots 2 nm in diameter. (b) A high resolution TEM image of a <100>-oriented fcc array of dots 4.8 nm in diameter, with the small angle electron diffraction pattern shown in the inset (from ref. [90]).

nanometric metal clusters covalently linked to each other by rigid organic molecules have been realized [91]. The realization of nanometric metal islands separated from each other by a tunnel barrier is of great interest for nanoscale electronics. In fact, electric conductance of such structures can be varied from the metallic to the insulating limit by controlling the size of the islands and their coupling (that is, their spacing), as well as the length and chemical structure of the organic molecules used as molecular interconnects. The possibility of injecting electrons into the quantum confined states of quantum dots has opened also the possibility of investigating their infrared optical spectrum [92–94]. It has, indeed, been shown that, if conventional doping (like for bulk materials) is unsuccessful and unstable for quantum dots, n-type colloidal nanocrystals can be fabricated by using an electron transfer approach commonly used for conducting organic polymers [93]. This has allowed the direct measurement of the infrared absorption spectrum corresponding to the $1s_e$-$1p_e$ transition between the ground and the first excited electronic state, as shown in Fig. 1.19. Further studies have demonstrated that the controlled electron occupation of quantum dots gives the possibil-

ity of tuning their optical properties by an electrochemical potential. Electrochromic quantum dots have been realized, showing that the injection of electrons leads to a size-tunable intra-band transition, to the bleach of the visible inter-band exciton transitions and a quench of the narrow band-edge photoluminescence [94]. This gives a further support to future applications of quantum dots for electronic or optoelectronic devices.

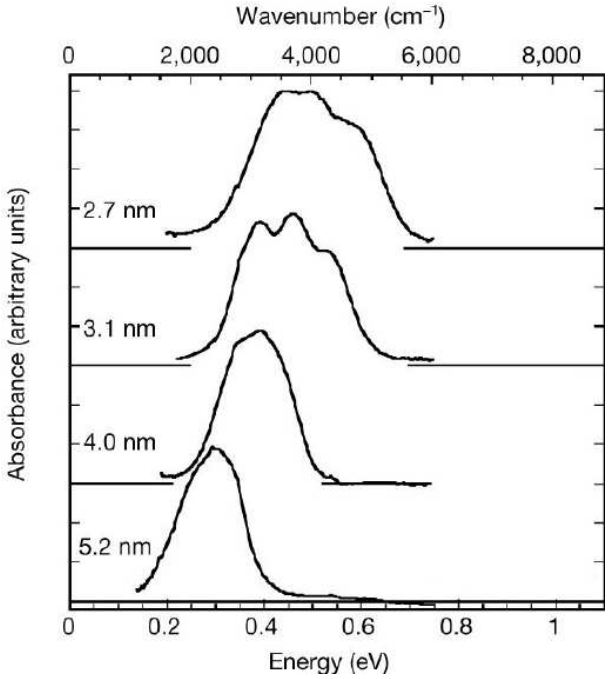

Figure 1.19: Infrared absorption spectrum of n-type CdSe colloidal nanocrystals, with different diameters (from ref. [93]). The two nanocrystals with smallest size give rise to a $1s_e$-$1p_e$ transition which shows three different peaks, possible due to the lifting of the three-fold degeneracy of the $1p_e$ states.

Chapter 2

Volume confined states in ellipsoid quantum dots

The study of the quantum confinement in low-dimensional structures can be theoretically performed, as pointed out in appendix A, within different schemes. A widely explored field is about how the nanostructure dimensions can affect many physical properties of the system, such as absorption and emission spectra, many-particle interactions, transport properties, etc. Within the effective-mass approximation (described in appendix A), many theoretical investigations have been done, in which the quantum dot is simulated with a confinement potential for electrons and holes, assumed to be in the form of a spherical potential well [95–97], isotropic [98–104] or anisotropic [105] harmonic potential (parabolic confinement), on-site repulsive potential [106], infinite barrier at the dot boundary [107–114], Gaussian potential [115] (see also ref. [16]). There have been many numerical approaches for studying few- and many-electron properties of these potentials (such as variational calculations, Hartree and Hartree-Fock methods, power series expansions, WKB approach and several diagonalization techniques). The main problem is that, even in the simplest scheme, that is, the infinite barrier at the dot boundary, it is very difficult to obtain exact solutions, unless high symmetry structures, such as spherical quantum dots, are considered. Anyway, this has allowed the investigation from the theoretical point of view of many experimentally observed properties, and

in particular the explanation of why they can be tuned just by changing the system dimensions. Nevertheless, it is expected that if these properties show a strong dependence on the dimensions, the system geometry should play a fundamental role as well. Therefore, it could be interesting to investigate how the physical properties of quantum dots can change for anisotropic systems. The theoretical aspects of single- and many-particle properties of anisotropic quantum dots have been studied for circular, elliptic and triangular vertical quantum dots [116], ellipsoidally deformed vertical quantum dots [117], quantum confinement within an ellipsoidally deformed harmonic potential [105], CdSe ellipsoid quantum dots [118, 119]. In these last two works, the dot anisotropy has been taken into account within a perturbative scheme, as a correction to the spherical quantum dot spectrum, while the valence band degeneracy has been properly taken into account. Nevertheless, it could be relevant to find an anisotropic geometry in which, even in the simplest effective-mass, infinite-barrier model, the Schrödinger equation can be exactly solved. In fact, alternative schemes require perturbation or variational calculations which treat the system geometry as a deviation from a reference, exactly solvable geometry, such as the spherical one and cannot account for an arbitrary system anisotropy.

In this chapter it is shown that if an ellipsoid geometry is considered, the single-particle confined energy levels can be exactly calculated, and some relevant effects on the dot optical properties derived from them. In sec. 2.1 the theoretical background needed for such calculations is given, showing how the Schrödinger equation can be separated within an ellipsoid region, allowing the exact calculation of the Hamiltonian eigenvalues and eigenvectors (subsec. 2.1.1). Moreover, because real systems are usually constituted by a dots matrix embedded in an external environment, the additional electrostatic potential due to the dielectric mismatch is exactly calculated (subsec. 2.1.2). The selection rules and electronic infrared (conduction band) transitions are studied (subsec. 2.1.3), showing how they change with respect to the spherical quantum dot, as effect of the anisotropy. Finally the effect of the system geometry on the electron-electron interaction is studied, using a variational scheme which allows to take in to account anisotropy-dependent correlations (subsec. 2.1.4).

In sec. 2.2 the numerical results obtained by using this theoretical background are shown, bringing out how all the main properties of the system are affected by its geometry. In particular, it is shown that it is not enough to specify just the system volume to explain the single-electron optical spectrum features (as for the spherical quantum dot) and that the optical transitions induced by electro-magnetic radiation become dependent on the emitted/absorbed radiation polarization.

2.1 Theory

2.1.1 Single-particle eigenfunctions and eigenvectors

The solution of the Schrödinger equation within an ellipsoid region can be performed exactly as for the spherical quantum dot [108]. Let us consider an ellipsoid quantum dot with rotational symmetry around the z direction and indicate with a and c its semi-axes in the x-y plane and along the z direction respectively (x, y and z are the coordinates in a Cartesian orthogonal system with origin in the ellipsoid symmetry centre). The considered region is limited by the surface S with parametric equations

$$\begin{cases} x = a\cos\varphi\sin\Theta \\ y = a\sin\varphi\sin\Theta \\ z = c\cos\Theta \end{cases} \tag{2.1}$$

with $0 \leq \varphi < 2\pi$ and $0 \leq \Theta \leq \pi$. This surface is shown in Fig. 2.1a for $c > a$ (*prolate ellipsoid*) and in Fig. 2.1b for $c < a$ (*oblate ellipsoid*).

The problem is to solve the free-electron[1] Schrödinger equation

$$-\frac{\hbar^2}{2m^*}\overrightarrow{\nabla}^2\Psi\left(x,y,z\right) = E^v\Psi\left(x,y,z\right) \tag{2.2}$$

(where m^* is the electron effective-mass and E^v its volume confined energy) with the boundary condition

$$\Psi\left(x,y,z\right)\big|_{(x,y,z)\in S} = 0. \tag{2.3}$$

[1] In the following, conduction-band electrons will be considered. The theory is valid for holes as well, provided that valence band degeneracy and/or mixing do not make the effective-mass approximation to fail.

Because the surface has rotational symmetry only with respect to the z axis, the considered Schrödinger system (that is, the free-particle Hamiltonian with the associated boundary condition (2.3)) no longer commutes with all the angular momentum operators, and spherical coordinates are not suitable if an exact solution of the problem is needed. Therefore, a new coordinates system (ξ, η, φ) must be found, such that eq. (2.2) is separable and that the equation of the ellipsoid surface S reads $\xi =$ constant. Let us consider [120, 121] the following transformation (*prolate spheroidal coordinates* [122]):

$$\begin{cases} x = f\sqrt{(\xi^2-1)\,(1-\eta^2)}\cos\varphi \\ y = f\sqrt{(\xi^2-1)\,(1-\eta^2)}\sin\varphi \\ z = f\xi\eta \end{cases} , \tag{2.4}$$

where $1 \leq \xi < +\infty$, $-1 \leq \eta \leq +1$, $0 \leq \varphi < 2\pi$ and f is a parameter. By setting $\eta = \cos\Theta$ with $0 \leq \Theta \leq \pi$ and by comparing eq. (2.4) with the boundary parametric equations (2.1), it is seen that the surfaces obtained by setting $\xi =$ constant represent a family of ellipsoids with semi-axes $f\sqrt{\xi^2-1}$ and $f\xi$ (in the x-y plane and along the z direction respectively), all characterized by the same focal distance $2f$. Similarly, a family of hyperboloids is obtained by setting $\eta =$ constant and a family of half-planes with origin in the z axis is obtained by setting $\varphi =$ constant, as shown in Fig. 2.2a. These three surfaces families are mutually orthogonal. The parameter f which appears in the definition of the new coordinates system (2.4) is determined by the condition that the ellipsoid boundary S belongs to the surfaces family $\xi =$ constant, that is, it must exist a value $\overline{\xi}$ of ξ such that

$$\begin{cases} f\sqrt{\overline{\xi}^2-1} = a \\ f\overline{\xi} = c \end{cases} \Rightarrow \begin{cases} f = c\sqrt{1-\dfrac{1}{\chi^2}} = ce \\ \overline{\xi} = \dfrac{1}{\sqrt{1-\dfrac{1}{\chi^2}}} = \dfrac{1}{e} \end{cases} , \tag{2.5}$$

where $\chi = c/a$ is the ellipsoid aspect ratio and $e = f/c$ its eccentricity.

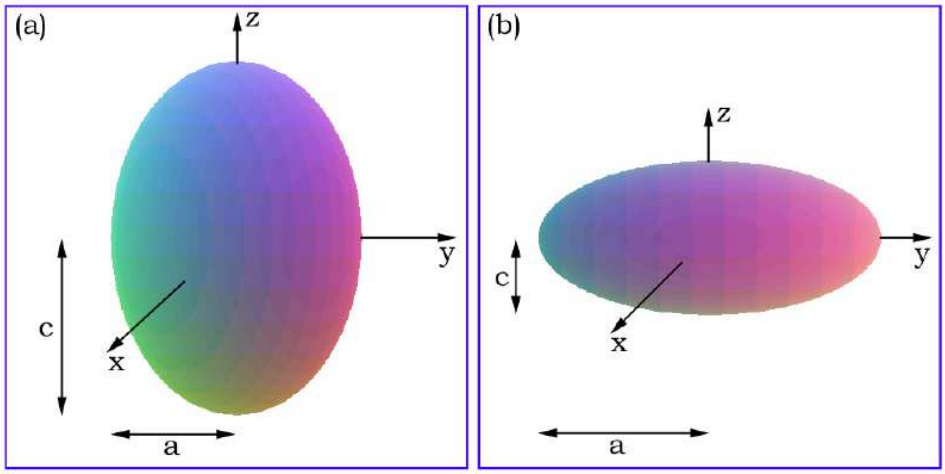

Figure 2.1: (a) A prolate ellipsoid. (b) An oblate ellipsoid. Let us note that the oblate ellipsoid cannot be obtained by rotating the prolate ellipsoid around some axis.

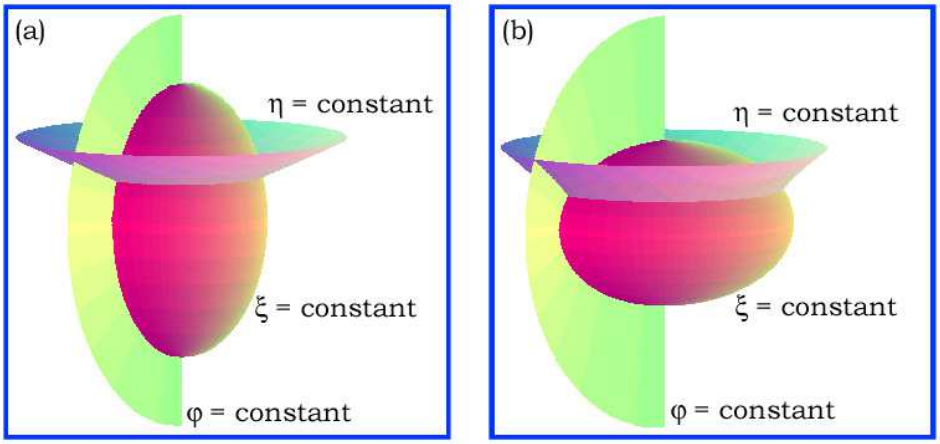

Figure 2.2: The orthogonal surfaces obtained by setting $\xi = \text{constant}$, $\eta = \text{constant}$ and $\varphi = \text{constant}$ for (a) prolate and (b) oblate spheroidal coordinates.

It is evident that eq. (2.5) is valid only if $\chi > 1$, which follows from the fact that the transformation (2.4) parameterizes the space with ellipsoid surfaces which have the semi-axis along the z direction greater than the semi-axes in the x-y plane. The case $\chi < 1$ will be discussed later.

In order to write eq. (2.2) in the prolate spheroidal coordinates system it is necessary to write the Laplacian operator in the new coordinates system (2.4). It is possible to show that if (q_1, q_2, q_3) indicate a generic curvilinear coordinates system the following expression holds [123]:

$$\overrightarrow{\nabla}^2 = \frac{1}{\sqrt{\det \mathbf{G}}} \sum_{i,j=1}^{3} \frac{\partial}{\partial q_i} \left[\overline{G}_{i,j} \sqrt{\det \mathbf{G}} \frac{\partial}{\partial q_j} \right], \tag{2.6}$$

where $\mathbf{G} \equiv ||G_{i,j}|| = ||\partial\vec{r}/\partial q_i \cdot \partial\vec{r}/\partial q_j||$ is the metric tensor and $\overline{G}_{i,j}$ the ratio between the algebraic complement of $G_{i,j}$ and $\det \mathbf{G}$. By using eq. (2.4) ($(q_1, q_2, q_3) \equiv (\xi, \eta, \varphi)$) it is not difficult to show that

$$\mathbf{G} = \begin{Vmatrix} f^2 \dfrac{\xi^2 - \eta^2}{\xi^2 - 1} & 0 & 0 \\ 0 & f^2 \dfrac{\xi^2 - \eta^2}{1 - \eta^2} & 0 \\ 0 & 0 & f^2 (\xi^2 - 1)(1 - \eta^2) \end{Vmatrix}. \tag{2.7}$$

It comes out that the non-diagonal elements of the metric tensor are zero, showing that the coordinates system (2.4) is orthogonal. By using eqs. (2.6) and (2.7) the expression of the Laplacian operator in prolate spheroidal coordinates is easily obtained and eq. (2.2) becomes:

$$-\frac{1}{f^2(\xi^2 - \eta^2)} \left\{ \frac{\partial}{\partial \xi} \left[(\xi^2 - 1) \frac{\partial \Psi}{\partial \xi}(\xi, \eta, \varphi) \right] + \frac{\partial}{\partial \eta} \left[(1 - \eta^2) \frac{\partial \Psi}{\partial \eta}(\xi, \eta, \varphi) \right] + \frac{\xi^2 - \eta^2}{(\xi^2 - 1)(1 - \eta^2)} \frac{\partial^2 \Psi}{\partial \varphi^2}(\xi, \eta, \varphi) \right\} = \varepsilon^v \Psi(\xi, \eta, \varphi), \tag{2.8}$$

where $\varepsilon^v = 2m^* E^v / \hbar^2$, and the boundary condition (2.3) can be written as

$$\Psi(\overline{\xi}, \eta, \varphi) = 0. \tag{2.9}$$

It is easy to show that eq. (2.8) with the boundary condition (2.9) can be solved with the separation of variables technique [120]. In other words, its

solution can be written as $\Psi(\xi,\eta,\varphi) = je(\xi)\,S(\eta)\exp(im\varphi)$, where it has been taken into account the fact that, because of the rotational symmetry around the z direction, it is possible to find a complete set of solutions of eq. (2.2) which are simultaneously eigenfunctions of the z component of the angular momentum with eigenvalues $m\hbar$ ($m = 0, \pm1, \pm2, \dots$). In this way eq. (2.8) separates in the two coupled equations (for je and S respectively)

$$\frac{d}{d\xi}\left[\left(\xi^2-1\right)\frac{dje}{d\xi}\right] - \left(A - h^2\xi^2 + \frac{m^2}{\xi^2-1}\right)je = 0, \tag{2.10a}$$

$$\frac{d}{d\eta}\left[\left(1-\eta^2\right)\frac{dS}{d\eta}\right] + \left(A - h^2\eta^2 - \frac{m^2}{1-\eta^2}\right)S = 0. \tag{2.10b}$$

Eqs. (2.10a) and (2.10b) are usually referred to as respectively the "radial" and the "angular" equation. A represents the separation constant and $h = f\sqrt{\varepsilon^v}$. It can be noticed that eqs. (2.10a) and (2.10b) are coupled by both the separation constant and the eigenvalue (proportional to h^2). Therefore, the separation of the Schrödinger equation in spheroidal coordinates is more difficult than in spherical or cylindrical coordinates. In fact, in these last cases only the first equation contains the eigenvalue so that one can solve the second equation by determining the A values which give a regular angular solution, substitute these values in the first equation and then solve it to get the radial solutions and the allowed energy levels. In this case the same procedure can be followed, but the angular equation must be solved with fixed h so that the discrete set of A values, obtained by requiring that the angular solution is regular at the points $\eta = -1$ and $\eta = +1$, are functions of h. Some further mathematical details are given in appendix B.

It must be pointed out that, if $\chi \to 1$ (that is, $f, h \to 0$), the prolate spheroidal coordinates tend to spherical coordinates (because the surfaces $\xi =$ constant become ellipsoids with a very small focal distance as shown by eq. (2.5)). A direct consequence is that if in eq. (2.10b) the limit $h \to 0$ is considered, we must obtain $S(\eta) \to P_l^{|m|}(\eta)$ (where $P_l^{|m|}(\eta)$ are the associated Legendre functions) and $A \equiv A(h) \to l(l+1)$ with $l = |m|, |m|+1, |m|+2, \dots$. Therefore, it is possible to label the solutions of eq. (2.10b) and the corresponding values of the separation constant as $S(\eta) \equiv S_{l,m}(h,\eta)$ and $A \equiv A_{l,|m|}(h)$ with $|m| = 0, 1, 2, \dots$ and $l = |m|, |m|+1, |m|+2, \dots$.

Correspondingly it can be set for eq. (2.10a) $je(\xi) \equiv je_{l,m}(h,\xi)$ (see also appendix B). It can be shown [122] that the solutions of eq. (2.10a) and (2.10b) can be written respectively as

$$je_{l,m}(h,\xi) = \left(\frac{\xi^2-1}{\xi^2}\right)^{\frac{|m|}{2}} {\sum_{s=0,1}^{+\infty}}' a_s^{l,|m|}(h)\, j_{s+|m|}(h\xi) \tag{2.11a}$$

and

$$S_{l,m}(h,\eta) = {\sum_{s=0,1}^{+\infty}}' d_s^{l,|m|}(h)\, P_{s+|m|}^{|m|}(\eta)\,, \tag{2.11b}$$

where j_k is the spherical Bessel function of order k. The primate sum indicates that the sum must be extended over even values or odd values of s in which cases it begins from 0 and 1 respectively. This reflects the system invariance with respect to parity transformations.

If $c < a$ (that is, $\chi < 1$) it is possible to follow the same procedure indicated above but using oblate spheroidal coordinates defined as follows [124]:

$$\begin{cases} x = f\sqrt{(\xi^2+1)(1-\eta^2)}\cos\varphi \\ y = f\sqrt{(\xi^2+1)(1-\eta^2)}\sin\varphi, \\ z = f\xi\eta \end{cases} \tag{2.12}$$

with $0 \le \xi < +\infty$, $-1 \le \eta \le +1$ and $0 \le \varphi < 2\pi$. The surfaces $\xi =$ constant represent a family of ellipsoids with semi-axes $f\sqrt{\xi^2+1}$ and $f\xi$ (the semi-axis in the x-y plane is in this case greater than the one along the z direction). The orthogonal surfaces obtained by keeping constant ξ, η and φ are shown in Fig. 2.2b. The condition that the considered ellipsoid belongs to the surfaces family $\xi =$ constant (given by eq. (2.5) for prolate spheroidal coordinates) in this case becomes:

$$\begin{cases} f\sqrt{\overline{\xi}^2+1} = a \\ f\overline{\xi} = c \end{cases} \Rightarrow \begin{cases} f = c\sqrt{\dfrac{1}{\chi^2}-1} = ae \\ \overline{\xi} = \dfrac{1}{\sqrt{\dfrac{1}{\chi^2}-1}} = \dfrac{\chi}{e} \end{cases}, \tag{2.13}$$

with $\chi < 1$. The metric tensor is:

$$\mathbf{G} = \left\| \begin{array}{ccc} f^2 \dfrac{\xi^2+\eta^2}{\xi^2+1} & 0 & 0 \\ 0 & f^2 \dfrac{\xi^2+\eta^2}{1-\eta^2} & 0 \\ 0 & 0 & f^2\left(\xi^2+1\right)\left(1-\eta^2\right) \end{array} \right\|. \tag{2.14}$$

By using eqs. (2.6) and (2.14) the expression of the Laplacian operator in oblate spheroidal coordinates can be obtained and eq. (2.2) becomes:

$$-\frac{1}{f^2(\xi^2+\eta^2)}\left\{\frac{\partial}{\partial\xi}\left[(\xi^2+1)\frac{\partial\Psi}{\partial\xi}(\xi,\eta,\varphi)\right]+\frac{\partial}{\partial\eta}\left[(1-\eta^2)\frac{\partial\Psi}{\partial\eta}(\xi,\eta,\varphi)\right]+\right.$$
$$\left.\frac{\xi^2+\eta^2}{(\xi^2+1)(1-\eta^2)}\frac{\partial^2\Psi}{\partial\varphi^2}(\xi,\eta,\varphi)\right\}=\varepsilon^v\Psi(\xi,\eta,\varphi). \tag{2.15}$$

As for the case of prolate spheroidal coordinates, eq. (2.15) can be separated in a radial and an angular equation given by:

$$\frac{d}{d\xi}\left[\left(\xi^2+1\right)\frac{dje}{d\xi}\right]-\left(A-h^2\xi^2-\frac{m^2}{\xi^2+1}\right)je = 0, \tag{2.16a}$$
$$\frac{d}{d\eta}\left[\left(1-\eta^2\right)\frac{dS}{d\eta}\right]+\left(A+h^2\eta^2-\frac{m^2}{1-\eta^2}\right)S = 0, \tag{2.16b}$$

and their solutions provided in the form of a series expansion. Eq. (2.11a) becomes:

$$je_{l,m}\left(h,\xi\right)=\left(\frac{\xi^2+1}{\xi^2}\right)^{\frac{|m|}{2}}{\sum_{s=0,1}^{+\infty}}' a_s^{l,m}\left(h\right)j_{s+|m|}\left(h\xi\right), \tag{2.17}$$

while eq. (2.11b) is formally unchanged.

The solution of eq. (2.10a) or eq. (2.16a) (depending on whether $\chi > 1$ or $\chi < 1$ respectively) with the additional condition $je_{l,m}\left(h,\overline{\xi}\right)=0$ (hard walls boundary condition) gives the confined spectrum of the ellipsoid quantum dot. Because for fixed l and m the boundary condition can be compatible with a discrete set of values of h, an additional label n (principal quantum number)

is needed to classify the eigenvalues, namely $h \equiv h_{n,l,m}(\chi)$. Therefore, the energy spectrum of the ellipsoid quantum dot will take the form [120]:

$$E^v_{n,l,m} = \frac{\hbar^2}{2m^*} \frac{\widetilde{\varepsilon}^v_{n,l,m}(\chi)}{c^2}, \tag{2.18a}$$

where the adimensional quantity $\widetilde{\varepsilon}^v_{n,l,m}(\chi)$ is given by the equation:

$$\frac{\widetilde{\varepsilon}^v_{n,l,m}(\chi)}{c^2} = \varepsilon^v_{n,l,m}(\chi) = \frac{h^2_{n,l,m}(\chi)}{c^2 \left| 1 - \dfrac{1}{\chi^2} \right|}. \tag{2.18b}$$

The corresponding eigenfunctions are given by:

$$\Psi_{n,l,m}(\vec{r}) = \mathcal{A}_{n,l,m}\; je_{l,m}(h_{n,l,m}, \xi) S_{l,m}(h_{n,l,m}, \eta) \exp(im\varphi), \tag{2.18c}$$

where $\mathcal{A}_{n,l,m}$ is a normalization constant.

As already pointed out before, it is expected that the spherical quantum dot limit is recovered as $\chi \to 1$. Let us remember that for the sphere a complete set of eigenfunctions is given by

$$\Psi^{\text{SPHERE}}_{n,l,m}(r, \vartheta, \varphi) = \mathcal{B}_{n,l,m}\; j_l \left[z_{n,l} \frac{r}{R} \right] Y^m_l(\vartheta, \varphi), \tag{2.19a}$$

where (r, ϑ, φ) are the spherical coordinates of the generic point, R is the sphere radius, $z_{n,l}$ the n-th zero of the Bessel function of order l and $Y^m_l(\vartheta, \varphi)$ the spherical harmonics ($Y^m_l(\vartheta, \varphi) \propto P^{|m|}_l(\cos\vartheta) \exp(im\varphi)$). This state has energy (in units $\hbar^2/2m^*$)

$$\varepsilon^{\text{SPHERE}}_{n,l} = \frac{z^2_{n,l}}{R^2}, \tag{2.19b}$$

which is degenerate with respect to m. This energy levels can be labelled as ns, np, $nd, \ldots$, where s, p, $d, \ldots$ correspond to $l = 0, 1, 2, \ldots$ respectively. From the mathematical point of view n and $l-m$ are related to the number of nodes respectively of the radial part and the angular part of the wave function inside the sphere. Moreover, $l(l+1)\hbar^2$ takes the physical meaning of total angular momentum of the particle in the given quantum state, reflecting the full rotational symmetry of the problem. This, of course, is no longer true for the ellipsoid quantum states because this type of symmetry is lost. It

is therefore important to stress that if $\chi \neq 1$ the label l which appears in eqs. (2.11a), (2.17) and (2.11b) does not have the meaning of total angular momentum of the particle. It has been used here because it obviously exists a one-to-one correspondence between the quantum states in the sphere and the ones in the ellipsoid, so that these last ones can be labelled with the same quantum numbers of the state to which they reduce when $f \to 0$, as pointed out previously.

2.1.2 Dielectric effects

The single-particle picture shown in the last subsection allows the calculation of the exact kinetic energy contribution to the effective-mass, single-particle quantum confined states. Actually, an additional contribution has to be accounted for to give a correct description of the electron motion inside the dot. In fact it is known from classical electro-magnetism that if a charged particle is moving within a certain region of space which has a dielectric constant different from that of the surrounding medium, a surface polarization charge appears on the interface between the two media. This polarization charge generates an electrostatic potential which acts on the particle itself. Many works [108, 125–129] have demonstrated that confined levels in nanometric structures can be significantly modified by this additional contribution.

Let us consider a prolate ellipsoid and indicate with I the quantum dot region ($1 \leq \xi \leq \overline{\xi}$), with II the surrounding medium ($\xi > \overline{\xi}$), and with ε_I and ε_{II} the respective dielectric constants. The total electrostatic potential $V(\vec{r};\vec{r}_0)$ at a given point $\vec{r}$ due to a fixed electron at $\vec{r}_0$ is given by the solution of the Poisson equation

$$\overrightarrow{\nabla}^2 V(\vec{r};\vec{r}_0) = -\frac{e\delta(\vec{r}-\vec{r}_0)}{\varepsilon_0\varepsilon_I}, \tag{2.20}$$

with the following boundary conditions:

$$|V(\vec{r};\vec{r}_0)| < +\infty \;\; \forall \vec{r} \neq \vec{r}_0, \tag{2.21a}$$

$$\lim_{|\vec{r}|\to+\infty} |V(\vec{r};\vec{r}_0)| = 0 \;\; \forall \vec{r}_0, \tag{2.21b}$$

$$\lim_{\vec{r}\to\vec{r}_S^{\,-}} V(\vec{r};\vec{r}_0) = \lim_{\vec{r}\to\vec{r}_S^{\,+}} V(\vec{r};\vec{r}_0) \;\; \forall \vec{r}_S \in S, \; \forall \vec{r}_0, \tag{2.21c}$$

$$\varepsilon_I \lim_{\vec{r}\to\vec{r}_S^{\,-}} \hat{n}\cdot\overrightarrow{\nabla} V(\vec{r};\vec{r}_0) = \varepsilon_{II} \lim_{\vec{r}\to\vec{r}_S^{\,+}} \hat{n}\cdot\overrightarrow{\nabla} V(\vec{r};\vec{r}_0) \;\; \forall \vec{r}_S \in S, \; \forall \vec{r}_0, \tag{2.21d}$$

where the symbols $\vec{r}\to\vec{r}_S^{\,-}$ and $\vec{r}\to\vec{r}_S^{\,+}$ mean $\vec{r}\to\vec{r}_S$ with $\vec{r}\in I$ and $\vec{r}\in II$ respectively. It has been supposed that $\vec{r}_0 \notin S$. Eq. (2.21c) indicates that the electrostatic potential must be continuous on the surface S which separates the medium I from the medium II and eq. (2.21d) that its normal derivative is discontinuous on S (the ratio between the external normal derivative to the internal one in each point of S being $\varepsilon_I/\varepsilon_{II}$).

The most general solution of this problem can be written as [130]

$$V(\vec{r};\vec{r}_0) = V_C(|\vec{r}-\vec{r}_0|) + V_S(\vec{r};\vec{r}_0), \tag{2.22}$$

where

$$V_C(|\vec{r}-\vec{r}_0|) = \frac{q}{4\pi\varepsilon_0\varepsilon_I}\frac{1}{|\vec{r}-\vec{r}_0|} \tag{2.23}$$

is the Coulomb potential of a point charge $q=-e$ at $\vec{r}_0$ in the bulk material (infinite medium with dielectric constant ε_I) and $V_S(\vec{r};\vec{r}_0)$ the potential due to the surface polarization charge. The electrostatic problem can be solved by using the expansion of $V_C(|\vec{r}-\vec{r}_0|)$ in prolate spheroidal coordinates [131]:

$$\begin{aligned} V_C(|\vec{r}-\vec{r}_0|) \;=\; & \frac{q}{4\pi\varepsilon_0\varepsilon_I}\frac{1}{f}\sum_{l=0}^{+\infty}(2l+1)\sum_{m=0}^{l}\epsilon_m i^m\left[\frac{(l-m)!}{(l+m)!}\right]^2 P_l^m(\eta_0)\,P_l^m(\eta)\cdot \\ & P_l^m(\xi_<)\,Q_l^m(\xi_>)\cos\left[m\left(\varphi-\varphi_0\right)\right], \end{aligned} \tag{2.24}$$

where $\epsilon_0 = 1, \epsilon_1 = \epsilon_2 = \cdots = \epsilon_m = \cdots = 2$, $\xi_< = \min\{\xi,\xi_0\}, \xi_> = \max\{\xi,\xi_0\}$ and P_l^m and Q_l^m are respectively the first and second kind associated Legendre functions. Moreover, by inserting eq. (2.22) in the Poisson equation (2.20) it comes out that $V_S(\vec{r};\vec{r}_0)$ is an harmonic function, that is, it is solution of the Laplace equation

$$\overrightarrow{\nabla}^2 V_S(\vec{r};\vec{r}_0) = 0 \tag{2.25}$$

in all the space and for any fixed $\vec{r}_0$. By using eqs. (2.6) and (2.7) it is possible to write eq. (2.25) in prolate spheroidal coordinates and show [131] that the

set of linearly independent functions

$$v_{l,m}^{(1)}(\vec{r}) = P_l^{|m|}(\xi) P_l^{|m|}(\eta) \exp(im\varphi) \tag{2.26}$$

is a basis set for the solutions of the Laplace equation (2.25) which are regular at $\vec{r} = \vec{0}$ but not vanishing as $|\vec{r}| \to +\infty$, while the set of linearly independent functions

$$v_{l,m}^{(2)}(\vec{r}) = Q_l^{|m|}(\xi) P_l^{|m|}(\eta) \exp(im\varphi) \tag{2.27}$$

is a basis set for the solutions of the Laplace equation (2.25) which are singular at $\vec{r} = \vec{0}$ but vanishing as $|\vec{r}| \to +\infty$. In eqs. (2.26) and (2.27) we have $l = 0, 1, 2, \ldots$ and $m = -l, \ldots, 0, \ldots, l$. Therefore, the most general solution of eq. (2.20) which satisfies the conditions (2.21a) and (2.21b) is in the form:

$$V(\vec{r}; \vec{r}_0) = \begin{cases} V_C(|\vec{r} - \vec{r}_0|) + V_S^{(I)}(\vec{r}; \vec{r}_0) & \text{if } \vec{r} \in I \\ V_C(|\vec{r} - \vec{r}_0|) + V_S^{(II)}(\vec{r}; \vec{r}_0) & \text{if } \vec{r} \in II \end{cases}, \tag{2.28}$$

where

$$V_S^{(I)}(\vec{r}; \vec{r}_0) = \sum_{l=0}^{+\infty} \sum_{m=-l}^{l} A_{l,m}^{(I)}(\vec{r}_0) v_{l,m}^{(1)}(\vec{r}), \tag{2.29a}$$

$$\widetilde{V}_S^{(II)}(\vec{r}; \vec{r}_0) \equiv V_C(|\vec{r} - \vec{r}_0|) + V_S^{(II)}(\vec{r}; \vec{r}_0) = \sum_{l=0}^{+\infty} \sum_{m=-l}^{l} A_{l,m}^{(II)}(\vec{r}_0) v_{l,m}^{(2)}(\vec{r}). \tag{2.29b}$$

It has been considered that in the region II there is not free charge, so that both the Coulomb and the surface contributions are both harmonic functions. The unknown coefficients $A_{l,m}^{(I)}$ and $A_{l,m}^{(II)}$ are determined by requiring that the boundary conditions (2.21c) and (2.21d) are satisfied and using the expansion (2.24) for the Coulomb potential. It can been shown [130] that

$$V_S^{(I)}(\vec{r}; \vec{r}_0) = \sum_{l=0}^{+\infty} \sum_{m=0}^{l} C_{l,m}^{(I)}(\xi_0, \eta_0) P_l^m(\xi) P_l^m(\eta) \cos[m(\varphi - \varphi_0)], \tag{2.30a}$$

$$\widetilde{V}_S^{(II)}(\vec{r}; \vec{r}_0) = \sum_{l=0}^{+\infty} \sum_{m=0}^{l} C_{l,m}^{(II)}(\xi_0, \eta_0) Q_l^m(\xi) P_l^m(\eta) \cos[m(\varphi - \varphi_0)], \tag{2.30b}$$

with:

$$C_{l,m}^{(I)}(\xi_0,\eta_0) = \frac{q}{4\pi\varepsilon_0\varepsilon_I}\frac{s-1}{f}(2l+1)\,\epsilon_m i^m\left[\frac{(l-m)!}{(l+m)!}\right]^2 P_l^m(\xi_0)\,P_l^m(\eta_0)\cdot \frac{Q_l^m(\bar{\xi})\,Q_l^{m'}(\bar{\xi})}{P_l^m(\bar{\xi})\,Q_l^{m'}(\bar{\xi}) - s\,Q_l^m(\bar{\xi})\,P_l^{m'}(\bar{\xi})}, \tag{2.31a}$$

$$C_{l,m}^{(II)}(\xi_0,\eta_0) = \frac{q}{4\pi\varepsilon_0\varepsilon_I}\frac{s}{f}(2l+1)\,\epsilon_m i^m\left[\frac{(l-m)!}{(l+m)!}\right]^2 P_l^m(\xi_0)\,P_l^m(\eta_0)\cdot \frac{P_l^m(\bar{\xi})\,Q_l^{m'}(\bar{\xi}) - Q_l^m(\bar{\xi})\,P_l^{m'}(\bar{\xi})}{P_l^m(\bar{\xi})\,Q_l^{m'}(\bar{\xi}) - s\,Q_l^m(\bar{\xi})\,P_l^{m'}(\bar{\xi})}, \tag{2.31b}$$

with $s = \varepsilon_I/\varepsilon_{II}$. $\vec{r},\vec{r}_0 \in I$ because hard walls boundary conditions are assumed, namely zero probability of finding the electron outside the dot.

The surface potential (2.30a) interacts with the electron which generated the surface polarization charge, giving rise to a positive contribution to the energy of the electron itself which in the following will be referred to as *surface self-interaction energy*. This term can be calculated classically as the work necessary to introduce a charge q inside the dot at $\vec{r}_0$, by elementary charge steps dq:

$$E_S(\vec{r}_0) = \int_0^{V_S^{(I)}(\vec{r}_0;\vec{r}_0)} q dV_S^{(I)} = \int_0^q q\frac{dV_S^{(I)}}{dq}dq = \frac{1}{2}qV_S^{(I)}(\vec{r}_0;\vec{r}_0), \tag{2.32}$$

where the factor $1/2$ arises just because it is a self-interaction energy (which means that the electron interacts with a potential which depend on the charge of the electron itself).

If a second charge q' is present inside the dot at $\vec{r}$, an interaction contribution to the total system energy has to be taken into account, given by

$$E_P(\vec{r};\vec{r}_0) = q'V_S^{(I)}(\vec{r};\vec{r}_0). \tag{2.33}$$

This term will be referred to in the following as *surface interaction energy* because it represents the interaction of q and q' via the surface polarization charge.

The calculation of the dielectric potential due to the surface polarization charge can be performed for an oblate ellipsoid as well.

2.1.3 Infrared optical properties of ellipsoid quantum dots

It is known [132] that the transition probability between two quantum states $|a>$ and $|b>$ as effect of an electro-magnetic wave is proportional, in the dipole approximation, to the square modulus of the momentum operator between the two states. In other words, if $\hat{e}$ is the polarization vector of the incident wave, the relevant quantity is given by

$$p_{ba} = \hat{e} \cdot < b|\vec{p}|a > . \tag{2.34}$$

By using standard quantum mechanics [132] it is possible to show that the momentum matrix element (2.34) is proportional to the matrix element of the dipole operator $\vec{d} = q\vec{r}$:

$$p_{ba} = \frac{im^*}{\hbar}(E_b - E_a)\ \hat{e} \cdot < b|\vec{r}|a >, \tag{2.35}$$

where E_a and E_b are the energies of the states $|a>$ and $|b>$ respectively. Moreover, it is possible to show that, depending on the particular symmetry group of the considered Hamiltonian, the matrix element (2.35) or, equivalently, (2.34), is not different from zero for any couple of the initial and final states. Instead, non-zero values can be obtained provided that the initial and final states satisfy well defined conditions, known as *selection rules*. The transitions for which this matrix element is null, can be obviously allowed if higher order terms than the dipole one are considered in the transition probability expansion, but they correspond to very small probabilities if compared with transitions which are not forbidden in the dipole approximation. The selection rules can be determined by requiring that

$$\hat{e} \cdot < b|\vec{r}|a > \neq 0. \tag{2.36}$$

Because the considered system has axial symmetry around the z axis, it is interesting to study the inequality (2.36) for waves linearly polarized along the z axis or circularly polarized in the x-y plane, in which cases it becomes respectively

$$< b|z|a > \neq 0 \tag{2.37}$$

and

$$< b|\frac{x \pm iy}{\sqrt{2}}|a >\neq 0. \tag{2.38}$$

This means that the selection rules can change according to the particular polarization of the electro-magnetic wave.

The determination of the selection rules for radiation-induced transitions in ellipsoid quantum dots requires the calculation of the matrix elements which appear in eqs. (2.37) and (2.38) on the quantum confines states (2.18c). Therefore, we can identify the initial and final states with three quantum numbers, namely, $|a >\equiv |n'l'm' >$ and $|b >\equiv |nlm >$. Let us consider the case of a prolate ellipsoid. From eq. (2.4) we get

$$z = f\xi\eta \tag{2.39}$$

and

$$\begin{aligned}\frac{x \pm iy}{\sqrt{2}} &= \frac{f\sqrt{(\xi^2-1)(1-\eta^2)}\cos\varphi \pm if\sqrt{(\xi^2-1)(1-\eta^2)}\sin\varphi}{\sqrt{2}} \\ &= \frac{f\sqrt{(\xi^2-1)(1-\eta^2)}}{\sqrt{2}}\exp(\pm i\varphi).\end{aligned} \tag{2.40}$$

The matrix element for light linearly polarized along the prolate ellipsoid major axis (cfr. eq. (2.37)) becomes

$$\begin{aligned}< nlm|z|n'l'm' > = \int_1^{\bar{\xi}} d\xi \int_{-1}^{1} d\eta \int_0^{2\pi} d\varphi f^3(\xi^2-\eta^2)\Psi^*_{n,l,m}(\xi,\eta,\varphi)\cdot \\ f\xi\eta\Psi_{n',l',m'}(\xi,\eta,\varphi) = \mathcal{A}_{n,l,m}\mathcal{A}_{n',l',m'}f^4 I_1 I_2,\end{aligned} \tag{2.41}$$

where it has been considered that

$$d^3\vec{r} = \sqrt{\det \mathbf{G}}d\xi d\eta d\varphi = f^3(\xi^2-\eta^2)d\xi d\eta d\varphi. \tag{2.42}$$

It has been set

$$\begin{aligned}I_1 = \int_1^{\bar{\xi}} d\xi\ je_{l,m}(h_{n,l,m},\xi)\ \xi\ je_{l',m'}(h_{n',l',m'},\xi)\int_{-1}^{1} d\eta(\xi^2-\eta^2)\eta\cdot \\ S_{l,m}(h_{n,l,m},\eta)S_{l',m'}(h_{n',l',m'},\eta)\end{aligned} \tag{2.43}$$

and

$$I_2 = \int_0^{2\pi} d\varphi \exp[i(m' - m)\varphi]. \tag{2.44}$$

It is straightforward to see that $I_2 = 2\pi\delta_{m,m'}$, which leads to the selection rule

$$m = m'. \tag{2.45}$$

Moreover, we must consider that the integral I_1 contains the integration over η which is extended to an even interval. This means that because $\eta(\xi^2 - \eta^2)$ is odd with respect to η, the functions $S_{l,m}$ and $S_{l',m'}$ must have opposite parity. This leads[2] to the condition

$$(-1)^{l-m}(-1)^{l'-m'} = -1 \Leftrightarrow l - l' = 2k + 1, \quad k = 0, \pm 1, \pm 2, \ldots, \tag{2.46}$$

where eq. (2.45) has been taken into account.

If the radiation is circularly polarized in the x-y plane the matrix element of the operator (2.40) (cfr. eq. (2.38)) has to be calculated. We get:

$$\begin{aligned} < nlm| \frac{x \pm iy}{\sqrt{2}} |n'l'm' > = & \int_1^{\bar{\xi}} d\xi \int_{-1}^{1} d\eta \int_0^{2\pi} d\varphi f^3(\xi^2 - \eta^2) \cdot \\ & \Psi^*_{n,l,m}(\xi, \eta, \varphi) \frac{f\sqrt{(\xi^2 - 1)(1 - \eta^2)}}{\sqrt{2}} \exp(\pm i\varphi) \Psi_{n',l',m'}(\xi, \eta, \varphi) \\ = & \frac{\mathcal{A}_{n,l,m}\mathcal{A}_{n',l',m'} f^4}{\sqrt{2}} I_3 I_4, \end{aligned} \tag{2.47}$$

where it has been set

$$\begin{aligned} I_3 = & \int_1^{\bar{\xi}} d\xi \; je_{l,m}(h_{n,l,m}, \xi)\sqrt{(\xi^2 - 1)} \; je_{l',m'}(h_{n',l',m'}, \xi) \int_{-1}^{1} d\eta (\xi^2 - \eta^2) \cdot \\ & \sqrt{(1 - \eta^2)} \; S_{l,m}(h_{n,l,m}, \eta) S_{l',m'}(h_{n',l',m'}, \eta) \end{aligned} \tag{2.48}$$

and

$$I_4 = \int_0^{2\pi} d\varphi \exp[i(m' - m \pm 1)\varphi]. \tag{2.49}$$

[2]Let us remember that, as pointed out in appendix B, the wave function (2.18c) has parity $(-1)^l$ while $S_{l,m}$ has parity $(-1)^{l-m}$.

In this case $I_4 = 2\pi\delta_{m'\pm1,m}$, which leads to the selection rule

$$m' = m \pm 1. \tag{2.50}$$

As for the case of linearly polarized radiation, a second selection rule can be obtained by requiring that the integrand function in the integral I_4 is even. We get:

$$(-1)^{l-m}(-1)^{l'-m'} = 1 \Leftrightarrow l - l' \pm 1 = 2k, \quad k = 0, \pm1, \pm2, \ldots, \tag{2.51}$$

where eq. (2.50) has been taken into account. Let us note that the previous equation is equivalent to eq. (2.46). Therefore, the selection rules for radiation-induced transitions can be summarized [121] as follows:

$$\Delta l = l - l' = \pm1, \pm3, \ldots \text{ for any polarization} \tag{2.52a}$$

and

$$\Delta m = m - m' = \begin{cases} 0 & \text{for radiation linearly polarized along the } z \text{ axis} \\ \pm1 & \text{for radiation circularly polarized in the } x\text{-}y \text{ plane} \end{cases}. \tag{2.52b}$$

For oblate ellipsoids exactly the same selection rules hold, due to the fact that from the mathematical point of view the oblate ellipsoid can be obtained from the prolate one by performing the transformations $\xi =\rightarrow -i\xi$ and $h \rightarrow ih$, as pointed out in appendix B.

The description of the allowed radiation-induced transitions can be better done by introducing the oscillator strength

$$f_{ba} = \frac{2m^*}{3\hbar^2}(E_b - E_a)| < b|\vec{r}|a > |^2. \tag{2.53}$$

It is an adimensional quantity, proportional to the square modulus of the optical matrix element of the dipole operator between the two states. From eq. (2.53) it is seen that an absorption process is characterized by a positive oscillator strength, while it is negative for an emission process. The main feature of the oscillator strengths is that they satisfy the sum rule

$$\sum_b f_{ba} = 1, \tag{2.54}$$

where the sum is extended over a complete set of states. This is a quite interesting property, because it allows to individuate which transitions from or towards a given state $|a>$ are the most important ones in determining the system optical properties. Let us note that if we define

$$f_{ba}^{(\pm 1)} = \frac{2m^*}{3\hbar}(E_b - E_a)\left| < b|\frac{x \pm iy}{\sqrt{2}}|a > \right|^2 \tag{2.55a}$$

and

$$f_{ba}^{(0)} = \frac{2m^*}{3\hbar}(E_b - E_a)| < b|z|a > |^2, \tag{2.55b}$$

it can be shown that for any system with axial symmetry around the z axis each individual component of the oscillator strength satisfy the sum rule

$$\sum_b f_{ba}^{(\alpha)} = \frac{1}{3} \quad \alpha = 0, \pm 1 \tag{2.56a}$$

and that

$$\sum_{\alpha = 0,\pm 1} f_{ba}^{(\alpha)} = f_{ba} \tag{2.56b}$$

For the spherical quantum dot only transitions with $\Delta l = \pm 1$ are allowed. The lower degree of symmetry of the ellipsoid quantum dot relax this selection rule, making in principle allowed any transition for which Δl is odd. Actually, as we will see, the transition probabilities rapidly decrease with Δl, restricting the observable transitions to very few. Moreover, it is worth noting that the full rotational symmetry of the spherical quantum dot implies that the oscillator strength components (2.55a) and (2.55b) are equal. For the ellipsoid quantum dot the effect of the anisotropy is that $f_{ba}^{(0)} \neq f_{ba}^{(+1)} = f_{ba}^{(-1)}$, reflecting the axial symmetry of the system.

2.1.4 Two-electron ground state

Let us consider two conduction-band electrons moving inside the ellipsoid quantum dot. The ground state for the non-interacting system is simply given by the product of two single-particle ground-state wave functions:

$$\Psi_0^{(2)}(\vec{r}_1, \vec{r}_2) = je_{0,0}(h_{1,0,0}, \xi_1) S_{0,0}(h_{1,0,0}, \eta_1) je_{0,0}(h_{1,0,0}, \xi_2) S_{0,0}(h_{1,0,0}, \eta_2). \tag{2.57}$$

The two-electron Hamiltonian actually contains interaction terms, as follows:

$$H^{(2)} = \frac{p_1^2}{2m^*} + \frac{p_2^2}{2m^*} + \frac{e^2}{4\pi\varepsilon_0\varepsilon_I}\frac{1}{|\vec{r}_1 - \vec{r}_2|} - \frac{1}{2}e\Phi_S(\vec{r}_1) - \frac{1}{2}e\Phi_S(\vec{r}_2) - e\Phi_P(\vec{r}_1, \vec{r}_2), \tag{2.58}$$

where $\Phi_S(\vec{r}) = V_S^{(I)}(\vec{r};\vec{r})$ is the surface self-interaction potential (cfr. eq. (2.32)) and $\Phi_P(\vec{r}_1, \vec{r}_2) = V_S^{(I)}(\vec{r}_1;\vec{r}_2)$ is the surface electron-electron interaction potential. In eq. (2.58) it has been considered that the classical energy needed to realize the electrostatic configuration with both the electrons inside the dot is given by the sum of their Coulomb repulsion, the interaction of the two electrons with their respective surface charge (being a self-interaction effect, a factor 1/2 arises for these contributions, as pointed out at the end of subsec. 2.1.2) and the interaction of one electron with the surface charge generated by the second one. If $\varepsilon_I > \varepsilon_{II}$ (that is, $s = \varepsilon_I/\varepsilon_{II} > 1$), all the electrostatic terms raise the system total energy. Moreover, the Coulomb repulsion and the electron-electron interaction via the surface polarization charge tend to push the electrons far from each other while the self-interaction polarization terms have the opposite effect, pushing both electrons towards the quantum dot centre. This appears clear from Fig. 2.3a, where the contour plot of the surface self-interaction energy for $\chi = 2.0$ is shown, and Fig. 2.3b where the contour plot of the electron-electron surface interaction energy is shown for three different positions of one of the two electrons (indicated with a big dot).

If quantum dots with sufficiently small dimensions are considered, the electrostatic terms can be treated as a first order correction to the kinetic energy because the main contribution to the ground-state energy arises from quantum confinement. Within this picture (called the *strong confinement regime* [16]) the wave function (2.57) is assumed to describe with a good approximation the system of two almost non-interacting particles. Nevertheless, the more the dot dimensions increase, the more both the polarization terms and the Coulomb interaction correlate the two electrons. This means that the wave function (2.57) realistically describes the two-electron system only in the strong confinement regime[3], but it is not suitable for studying large

[3] A qualitative criterion for the strong confinement regime of electrons can be given

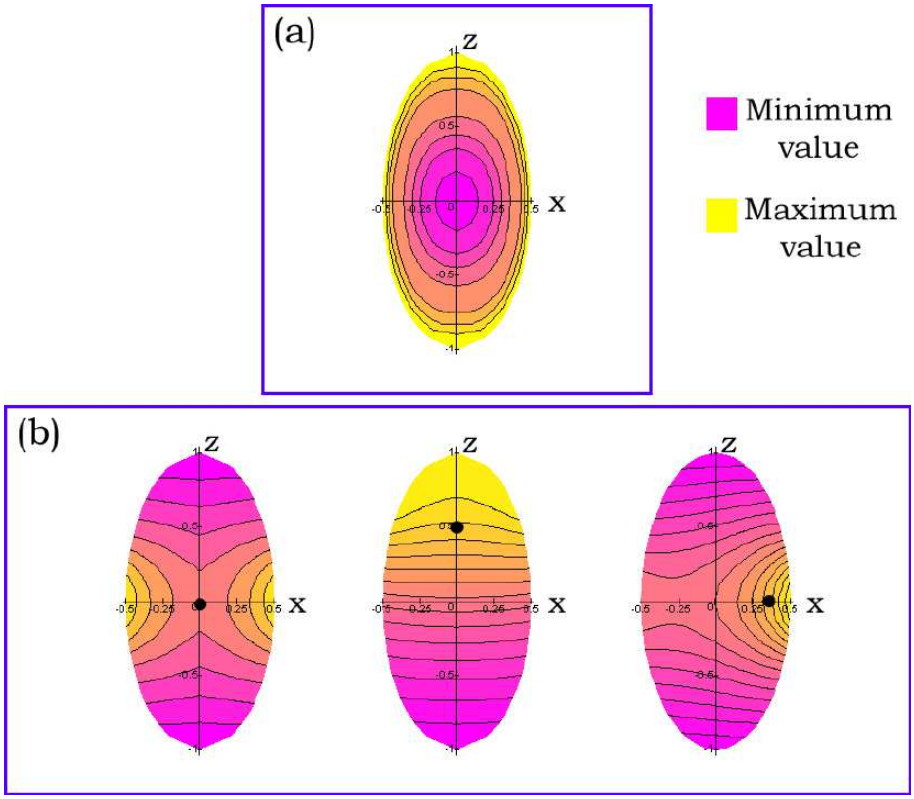

Figure 2.3: (a) The contour plot of the surface self-interaction energy is shown for a prolate ellipsoid with $\chi = 2.0$. (b) The contour plot of the surface electron-electron interaction energy is shown for three different positions of one of the two electrons (indicated with a big dot).

dots. Therefore the effect of both the dot dimensions and its anisotropy has been investigated by using the variational method. The trial wave function has been chosen as follows [130]:

$$\Psi^{(2)}\left(\vec{r}_1, \vec{r}_2\right) = \Psi_0^{(2)}\left(\vec{r}_1, \vec{r}_2\right) \Psi_{\text{corr}}\left(\vec{r}_1 - \vec{r}_2\right), \tag{2.59}$$

by assuming that the typical dot dimensions are much less than the electron Bohr radius $a_e = 4\pi\varepsilon_0\varepsilon_I\hbar^2/m^*e^2$ [16]. For example, for CdSe we have $a_e \simeq 4$ nm and we must require that $a, c << a_e$.

where $\Psi_0^{(2)}$ is given in eq. (2.57) and the correlated motion of the electrons is described via the factor

$$\Psi_{\text{corr}}\left(\vec{r}_1 - \vec{r}_2\right) = 1 - \alpha\left[1 + u\left(\vec{r}_1 - \vec{r}_2\right)\right]\exp\left[-u\left(\vec{r}_1 - \vec{r}_2\right)\right], \quad (2.60a)$$

$$u\left(\vec{r}_1 - \vec{r}_2\right) = \sqrt{\beta\left[\left(x_1 - x_2\right)^2 + \left(y_1 - y_2\right)^2\right] + \gamma\left(z_1 - z_2\right)^2}. \quad (2.60b)$$

The function (2.59) reflects the system ground-state properties. In fact (i) it depends only on $\varphi_1 - \varphi_2$ (that is, it is invariant for rotations of both the electrons of the same angle around the z axis), (ii) it is invariant for reflection of both the electrons (that is, with respect to the transformation $(\vec{r}_1, \vec{r}_2) \to (-\vec{r}_1, -\vec{r}_2)$), (iii) it is symmetric with respect to the exchange of the two electrons (corresponding to the singlet spin state), (iv) it is null if any of the two electrons is on the ellipsoid boundary, (v) it is continuous with all its first and second partial derivatives. α, β and γ are three variational parameters ($0 \leq \alpha \leq 1$, $\beta, \gamma \geq 0$), whose value must be determined by requiring that the energy functional

$$E\left[\alpha, \beta, \gamma\right] = \frac{\left\langle \Psi^{(2)} \middle| H^{(2)} \middle| \Psi^{(2)} \right\rangle}{\left\langle \Psi^{(2)} \mid \Psi^{(2)} \right\rangle} \quad (2.61)$$

be minimum. The particular choice of the correlated part of the wave function (2.59) can be justified [130] by considering that (i) if $\alpha = 0$ it becomes the uncorrelated wave function, (ii) if $\alpha \neq 0$ it describes the correlated system for which the probability of finding the two electrons at the same position is $|1 - \alpha|^2$ times smaller than that of finding them far from each other (this probability being null if $\alpha = 1$), (iii) if $\beta \neq \gamma$ it can account for the quantum dot anisotropy and therefore for the dependence of the electron-electron correlation on it, (iv) if the distance between the two electrons is very large, the wave function becomes the uncorrelated one.

2.2 Numerical results

2.2.1 Single-particle states

The solution of eqs. (2.10a) and (2.10b) for prolate spheroidal coordinates and eqs. (2.16a) and (2.16b) for oblate spheroidal coordinates has been performed

by using the numerical procedure described in appendix B. In this way the exact numerical[4] single-particle confined states for an ellipsoidal quantum dot as a function of the anisotropy have been first calculated [120, 121].

The spectra both for prolate ellipsoids with fixed a and oblate ellipsoids with fixed c as a function of χ are shown for the ground state and some excited states in Fig. 2.4 and Fig. 2.5 respectively.

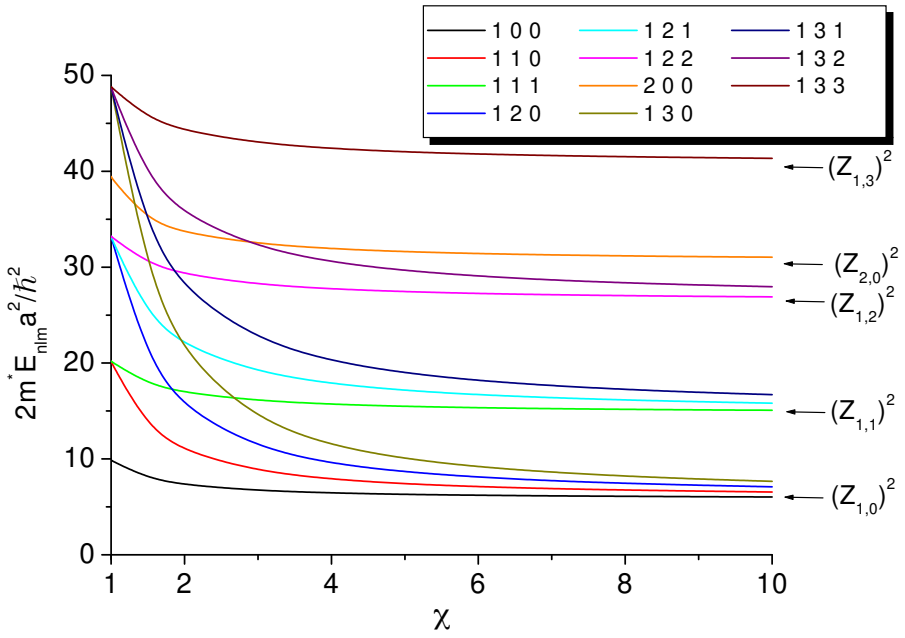

Figure 2.4: The prolate ellipsoid quantum dot spectrum as a function of χ. The energies are calculated with fixed a and are shown in units of $\hbar^2/2m^*a^2$.

Some evident effects induced by the anisotropy clearly come out. First, the degeneracy of the states with the same l but different m is removed as a consequence of the loss of rotational symmetry around an arbitrary axis, the only degeneracy being with respect to the sign of m. Second, it is seen that if $\chi > 1$ the states with the same n and m but different l become almost

[4] A brief discussion about the numerical accuracy of the results can be found in appendix B.

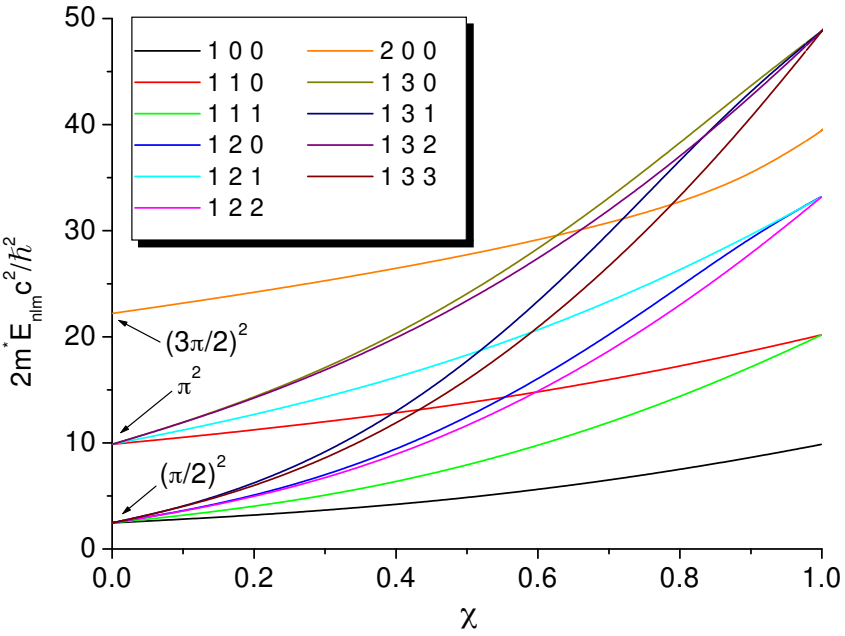

Figure 2.5: The oblate ellipsoid quantum dot spectrum as a function of χ. The energies are calculated with fixed c and are shown in units of $\hbar^2/2m^*c^2$.

degenerate as large values of χ are considered. Similarly, as χ approaches zero, states with the same n group into two sets of almost degenerate states, each set containing all the states with odd or even value of $l-m$. An explanation can be given by considering that if with fixed a we increase χ or, equivalently, c (prolate ellipsoids), more and more elongated quantum rods are obtained, the limit geometry for $\chi \to +\infty$ being a cylindrical quantum wire with radius a. For such a geometry, the quantum confined states and their relative eigenvalues can be written respectively as:

$$\Psi^{\mathrm{QW}}_{n,m,k_z} = \mathcal{C}_{n,m,k_z} J_{|m|}\left(\frac{Z_{n,|m|}}{a}\rho\right)\exp(im\varphi)\exp(ik_z z) \tag{2.62a}$$

and

$$E^{\mathrm{QW}}_{n,m}(k_z) = \frac{\hbar^2}{2m^*}\left(\frac{Z^2_{n,m}}{a^2} + k_z^2\right), \tag{2.62b}$$

where (ρ, z, φ) are the cylindrical coordinates ($0 \leq \rho < +\infty$, $-\infty < z < +\infty$, $0 \leq \varphi < 2\pi$), J_s the s-th cylindrical Bessel function, $Z_{n,s}$ its n-th zero and $\mathcal{C}_{n,m,k_z}$ a normalization constant. It is seen that a mini-band energy structure appears, with the edge of each mini-band depending on the two quantum numbers n (related to the number of nodes of the radial part of the wave function) and m ($m\hbar$ being the z component of the particle angular momentum). On increasing c, each ellipsoid confined state changes continuously in such a way that its limit is just a cylindrical quantum wire state having the same m and the same number of nodes of the wave function along the radial coordinate. In other words, all the ellipsoid quantum states with the same n and m but different l reconstruct a mini-band of the cylindrical quantum wire, which explains why, for example, the states with $n = 1$, $l = 0, 1, 2, 3, \ldots$, $m = 0$ appear nearly degenerate as $c \to +\infty$. The bottoms of the cylindrical quantum wire mini-bands are indicated in Fig. 2.4 by the arrows, showing that the numerical results clearly confirm the picture presented above. In the same way it can be explained the electronic spectrum structure if with fixed c ellipsoids with smaller and smaller χ are considered (that is, with increasing a). In this case the limit structure is given by two parallel planes (slab) with distance $2c$, for which the eigenfunctions and eigenvalues are respectively

$$\Psi^{\mathrm{SLAB}}_{n',m,k} = \mathcal{D}_{n',m,k} J_{|m|}(k\rho) \exp(im\varphi) \cdot \begin{cases} \cos\left(\dfrac{\pi}{2c} n' z\right) & \text{if } n' = 2n-1 \\ \sin\left(\dfrac{\pi}{2c} n' z\right) & \text{if } n' = 2n \end{cases} \tag{2.63a}$$

and

$$E^{\mathrm{SLAB}}_{n'}(k) = \frac{\hbar^2}{2m^*} \left(\frac{n'^2 \pi^2}{4c^2} + k^2 \right), \tag{2.63b}$$

where $n = 1, 2, 3, \ldots$, $k \geq 0$ ($k = \sqrt{k_x^2 + k_y^2}$), $m = 0, \pm 1, \pm 2, \ldots$. and $\mathcal{D}_{n',m,k}$ is a normalization constant. This shows that a two-dimensional mini-band structure appears, the bottom of each mini-band depending on n'. Let us note that, as eqs. (2.63) bring out, for a given m and n, two families of states are obtained, with opposite parity, given by $(-1)^m$ and $(-1)^{m+1}$ respectively. Because the sphere-ellipsoid-slab correspondence must be continuous and,

therefore, preserve parity, each ellipsoid state with given n and m goes in the first of the second family depending on whether $(-1)^l = (-1)^m$ (namely, $l-m$ is even) or $(-1)^l = (-1)^{m+1}$ (namely, $l-m$ is odd). Therefore, the family of states $\{n, l = 0, 1, 2, \ldots, m\}$ reconstruct, in the limit $\chi \to 0$, two slab mini-bands, corresponding to even and odd $l-m$. It is possible to show that this correspondence preserves, as it is expected, also the number of nodes of the wave functions. A scheme of the ellipsoid - cylindrical quantum wire and ellipsoid - slab correspondences is for clarity sketched in Fig. 2.6. This correspondences confirm the validity of the procedure which has been followed. The picture given above can also explain a third, interesting property of the ellipsoid quantum dot spectrum. In fact, some accidental degeneracies appear both for $\chi > 1$ and $\chi < 1$. This is because starting from the spherical quantum dot spectrum (obtained with $c = a$) and by increasing or decreasing χ, it has to be modified in such a way to reproduce the cylindrical quantum dot spectrum for large values of χ or the slab spectrum for small values of it. Because the energy levels in the two spectra are differently ordered, the appearance of levels crossings is needed, which explains the presence of accidental degeneracies. All these results bring out a very strong dependence of the system electronic properties on the dot anisotropy [120, 121].

A quantitative estimation of how the shape can modify the system properties can be done by considering constant volume properties. The volume of the ellipsoid is given by:

$$V = \frac{4}{3}\pi a^2 c = \frac{4}{3}\pi \frac{c^3}{\chi^2}, \tag{2.64}$$

where it has been considered that $\chi = c/a$. From eq. (2.64) we obtain that

$$c = \left(\frac{3V}{4\pi}\right)^{1/3} \chi^{2/3}. \tag{2.65}$$

Moreover, it is possible to define the "equivalent" sphere radius R_{eq}, namely the radius of the sphere with the same volume of the considered ellipsoid. It is given by the equation:

$$\frac{4}{3}\pi R_{\mathrm{eq}}^3 = V \Rightarrow R_{\mathrm{eq}} = \left(\frac{3V}{4\pi}\right)^{1/3}. \tag{2.66}$$

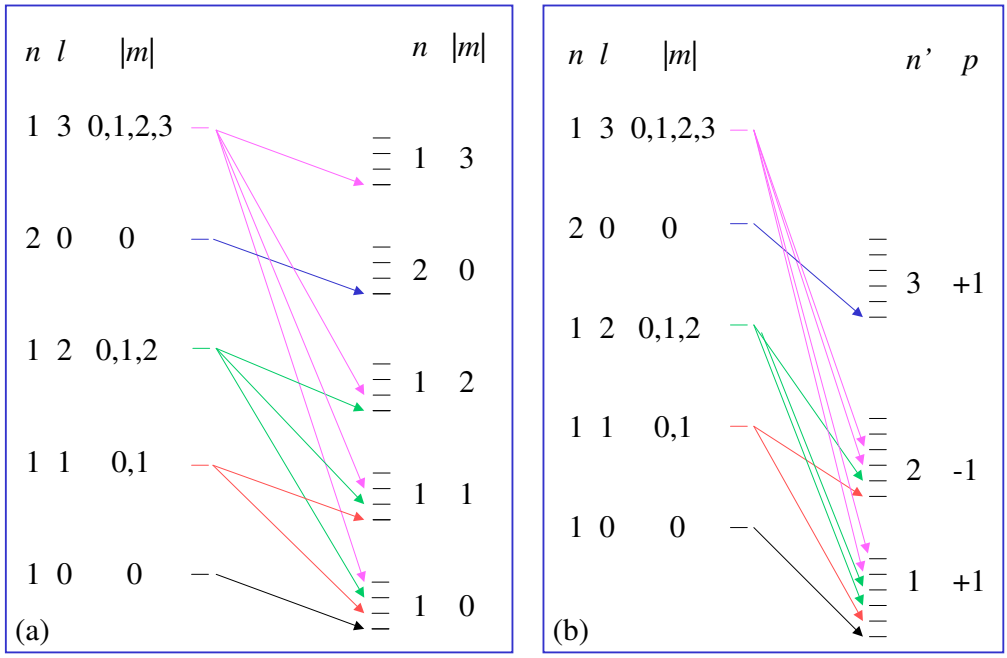

Figure 2.6: A simple scheme for the correspondence between the ellipsoid quantum dot spectrum and the spectra of its limit structures: (a) cylindrical quantum wire of radius a, (b) slab with distance $2c$ (p represents the parity of the considered state).

Combining eqs. (2.18a), (2.65) and (2.66) we obtain that the quantum confined spectrum of an ellipsoids family with constant volume V takes the form:

$$E^v_{n,l,m} = \frac{\hbar^2}{2m^*}\frac{1}{R^2_{\text{eq}}}\frac{\widetilde{\varepsilon}^v_{n,l,m}(\chi)}{\chi^{4/3}}. \tag{2.67}$$

If the spherical quantum dot is considered, we get

$$\lim_{\chi\to 1}\frac{\widetilde{\varepsilon}^v_{n,l,m}(\chi)}{\chi^{4/3}} = z^2_{n,l} \tag{2.68}$$

(compare with eq. (2.19b)) and the typical scaling of the confined eigenval-

ues with $1/R_{\rm eq}^2 \propto V^{-2/3}$ is retrieved. Nevertheless, if ellipsoid geometries are considered, an additional anisotropy dependence appears, as shown in Fig. 2.7, where the volume confined ground-state energy is shown as a function of χ for two different ellipsoids families with constant volume ($V = 905$ nm^3 and $V = 2145$ nm^3). If $\chi = 1$ we get the energies for spheres with radius $a = c = 6$ nm and $a = c = 8$ nm respectively. The spherical conduction-band effective mass for CdSe, which is $m^* = 0.13m_e$ (m_e is the free-electron mass) has been used. Moreover, in Fig. 2.8 it is shown the ellipsoid quantum dot spectrum obtained by keeping the volume constant at $V = 905$ nm^3. Two effects clearly come out. The first one is a volume effect, which corresponds to the fact that for fixed χ the bigger the volume the lower the confinement energy. The second and the most important one, is a shape effect, that is, the strong dependence of this energy on the structure geometry. In particular,

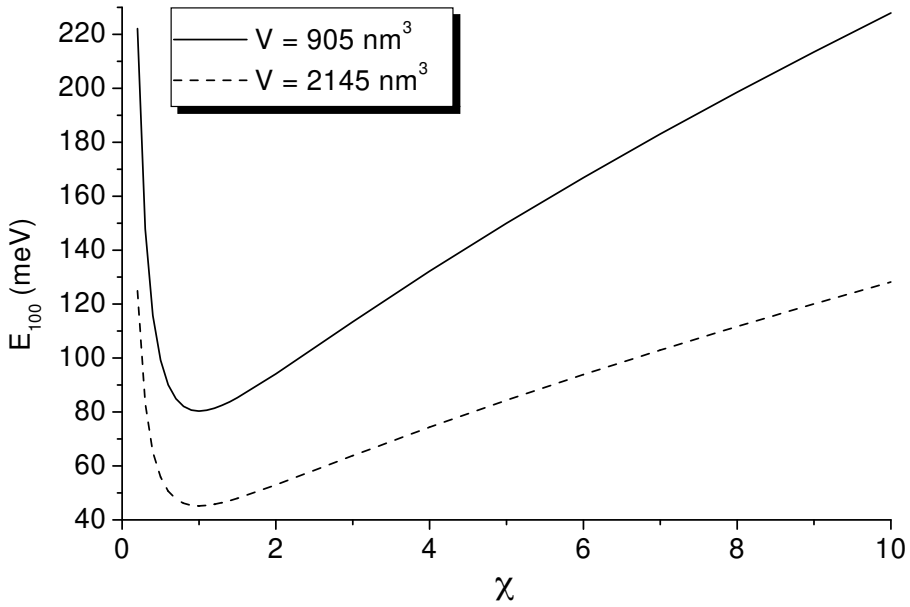

Figure 2.7: Constant volume energies for two different ellipsoids families with volume $V = 905$ nm^3 and $V = 1245$ nm^3. The energy is shown to be a function of both the system volume and the dot anisotropy.

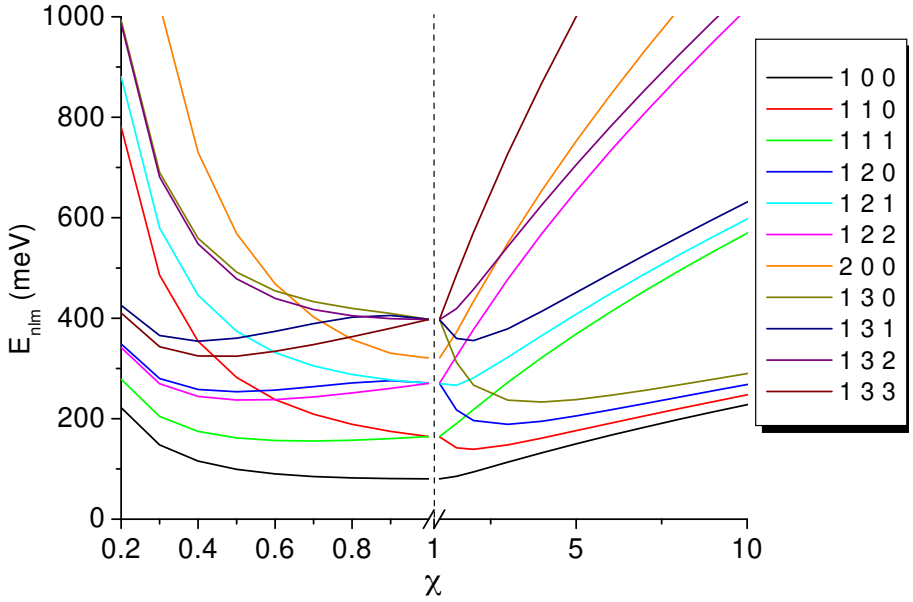

Figure 2.8: Constant volume energy spectrum calculated by keeping the ellipsoid volume fixed at $V = 905$ nm^3.

for a fixed volume the spherical geometry ($\chi = 1$) shows the lowest value of the ground-state energy while it is larger for anisotropic structures ($\chi \neq 1$). Therefore, we can conclude that as far as isotropic structures are concerned, quantum confinement can be explained in the simplest scheme as a pure volume effect (that is, the smaller the volume, the bigger the energy), the energy levels shift being proportional to $V^{-2/3}$, if V is the structure volume. But this picture becomes misleading if quantum dots with anisotropic shape are considered, the electronic levels being strongly dependent on the geometry even if the structure volume is kept constant. It can be useful to get interpolation formulas for the quantum confined energy levels. It has been found [130] that the following equations interpolate the numerical results within 0.4%

for $0.5 \leq \chi \leq 5.0$:

$$\widetilde{\varepsilon}^{v}_{1,0,0}(\chi) = 2.97035 + 6.59569|\chi + 0.02361|^{1.95395}, \tag{2.69a}$$
$$\widetilde{\varepsilon}^{v}_{1,1,0}(\chi) = 11.0548 + 8.20660|\chi + 0.05827|^{1.88390}, \tag{2.69b}$$
$$\widetilde{\varepsilon}^{v}_{1,1,1}(\chi) = 3.16983 + 15.71608|\chi + 0.0416|^{1.97543}. \tag{2.69c}$$

It is straightforward to verify that the limit (2.68) is verified within less than 0.1%.

In Fig. 2.9 the contour plot in the x-z plane of the wave function square modulus for the ground state and two excited states for $\chi = 2.0$ is shown.

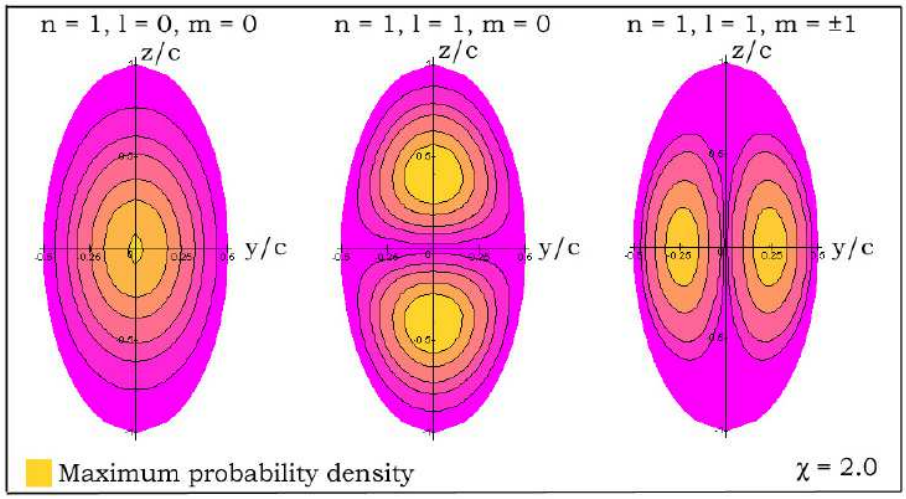

Figure 2.9: Contour plot of the wave function for the ground state and two excited states for $\chi = 2.0$. An "angular" distortion with respect to the spherical dot clearly appears, giving rise in particular to $l = 1$ non-equivalent states.

The full spatial configuration of the probability density associated to these states is obtained just by rotating these plots around the z axis. It is seen that the ground-state probability density, which for the spherical quantum dot has spherical symmetry, is deformed by the ellipsoidal boundary and its contour levels assume an elliptical shape. But the dot anisotropy has even more evident effects on the excited states $n = 1, l = 1, m = 0$ and

$n = 1, l = 1, |m| = 1$. These states, which for the spherical quantum dot can be obtained one from a rotation of the other one, are differently modified in such a way that for prolate ellipsoids the first one is more localized along the z direction while the second one in the x-y plane. This is a quite important property because, as we are going to see, it significantly modifies the transitions probabilities, in such a way that the system becomes sensitive to the light polarization [121].

2.2.2 Dielectric corrections to single-particle states

The single-particle energies shown in the previous subsection do not contain the contribution due to the dielectric mismatch described in subsec. 2.1.2. It has been pointed out that the difference between the quantum dot dielectric constant and that of the surrounding medium results in a surface polarization charge generated by the electron moving inside the dot. The electrostatic potential of this charge gives rise to a self-interaction contribution to the electron energy, that has to be taken into account. This can be done within a perturbative scheme [95, 108, 126], provided that the dimensions of the dot and the dielectric mismatch are chosen in such a way that the dielectric self-energy constitutes a small correction to the electron kinetic energy. Let us note that in the calculations which will be shown, it has been assumed that ε_I is the bulk dielectric constant. This could give incorrect results for the dielectric contributions. In fact, many works [25, 133–136] have demonstrated that on reducing the dot dimensions the dielectric constant gets lower values. Nevertheless, all these calculations show that for dot dimensions $R > 5 - 6$ nm the difference between the confined and the bulk dielectric constants is negligible. Therefore, because we are going to consider large dots, no significant correction is expected to come out from a size-dependent dielectric constant. The total single-electron energy can be written as [130]

$$E^{(1)}_{n,l,m} = E^{v}_{n,l,m} + E^{(n,l,m)}_{S}, \tag{2.70}$$

where $E^v_{n,l,m}$ are the eigenvalues of the kinetic energy operator calculated in the previous subsection and

$$E_S^{(n,l,m)} = \frac{\left\langle \Psi_{n,l,m}(\vec{r}) \left| -\frac{1}{2} e\Phi_S(\vec{r}) \right| \Psi_{n,l,m}(\vec{r}) \right\rangle}{\langle \Psi_{n,l,m}(\vec{r}) \mid \Psi_{n,l,m}(\vec{r}) \rangle}. \tag{2.71}$$

The self-interaction potential is given by eqs. (2.30a), (2.31a) and (2.32) and it does not actually depend on φ. The first order corrections to the $n = 1, l = m = 0$ and $n = 1, l = 1, m = 0, \pm 1$ energies have been numerically calculated as a function of χ and of the dielectric mismatch $s = \varepsilon_I/\varepsilon_{II}$. The corrections can be written as

$$E_S^{(n,l,m)} = \frac{1}{2} \frac{e^2}{4\pi\varepsilon_0\varepsilon_I c} e_S^{(n,l,m)}(s,\chi), \tag{2.72}$$

where $e_S^{(n,l,m)}(s,\chi)$ is an adimensional quantity which has been fitted with a polynomial expansion in the form:

$$e_S^{(n,l,m)}(s,\chi) = a_0^{(n,l,m)}(s) + a_1^{(n,l,m)}(s)\chi + a_2^{(n,l,m)}(s)\chi^2 + a_3^{(n,l,m)}(s)\chi^3, \tag{2.73}$$

where $1 \leq \chi \leq 5$. In this interval this expansion reproduces numerical results within 0.2%. The coefficients $a_i^{(n,l,m)}(s)$ for the three considered states are given in the tables 2.1, 2.2 and 2.3 for some values of s. For $\chi \to 1$ and $s = 3$ exactly the same result as in [126] for Si spherical quantum dots ($\varepsilon_I = 12$) embedded in a SiO_2 amorphous matrix ($\varepsilon_{II} = 4$) is obtained.

s	$a_0^{(1,0,0)}$	$a_1^{(1,0,0)}$	$a_2^{(1,0,0)}$	$a_3^{(1,0,0)}$
0.1	-0.47356	-0.81860	-0.08409	$+0.00935$
0.5	-0.24803	-0.43431	-0.03175	$+0.00343$
1.5	$+0.22243$	$+0.41346$	$+0.00936$	$-9.66578 \cdot 10^{-4}$
3.0	$+0.78634$	$+1.65047$	-0.04828	$+0.00494$
5.0	$+1.41225$	$+3.34807$	-0.22987	$+0.02251$
8.0	$+2.22401$	$+6.00116$	-0.61168	$+0.05794$
10.0	$+2.75832$	$+7.75776$	-0.87992	$+0.08161$

Table 2.1: The coefficients of eq. (2.73) for $n = 1, l = m = 0$ calculated for some values of s.

s	$a_0^{(1,1,\pm1)}$	$a_1^{(1,1,\pm1)}$	$a_2^{(1,1,\pm1)}$	$a_3^{(1,1,\pm1)}$
0.1	-0.45959	-1.06202	-0.08592	$+0.01142$
0.5	-0.25605	-0.52421	-0.03706	$+0.00478$
1.5	$+0.24063$	$+0.45746$	$+0.01652$	-0.00217
3.0	$+0.87043$	$+1.72082$	-0.01485	$+1.57609 \cdot 10^{-4}$
5.0	$+1.54924$	$+3.42313$	-0.18007	$+0.01558$
8.0	$+2.43742$	$+6.02219$	-0.52917	$+0.04689$
10.0	$+2.96229$	$+7.82346$	-0.81275	$+0.07215$

Table 2.3: The coefficients of eq. (2.73) for $n = 1, l = 1, |m| = 1$ calculated for some values of s.

s	$a_0^{(1,1,0)}$	$a_1^{(1,1,0)}$	$a_2^{(1,1,0)}$	$a_3^{(1,1,0)}$
0.1	-0.73749	-0.76860	-0.09947	$+0.01084$
0.5	-0.39373	-0.35488	-0.06676	$+0.00756$
1.5	$+0.25187$	$+0.46482$	-0.00474	$+3.0815 \cdot 10^{-4}$
3.0	$+0.81584$	$+1.84286$	-0.09099	$+0.00814$
5.0	$+1.40464$	$+3.65983$	-0.28333	$+0.02536$
8.0	$+2.17478$	$+6.40324$	-0.66170	$+0.05921$
10.0	$+2.72084$	$+8.15061$	-0.90728	$+0.07999$

Table 2.2: The coefficients of eq. (2.73) for $n = 1, l = 1, m = 0$ calculated for some values of s.

In Fig. 2.10a the corrections to the three considered states are shown as a function of s, for a CdSe ellipsoid quantum dot ($\varepsilon_I = 10.0$) with $a = 2.5$ nm and $c = 5.0$ nm ($\chi = 2.0$). The energy levels calculated without taking into account the dielectric contribution are also shown for comparison. It comes out that the correction to the kinetic energy eigenvalues become quite important as the dielectric mismatch increases and, therefore, cannot be neglected as far as the electronic spectrum is calculated. Nevertheless, if we consider the infrared transition energies (which are the relevant quantities from the

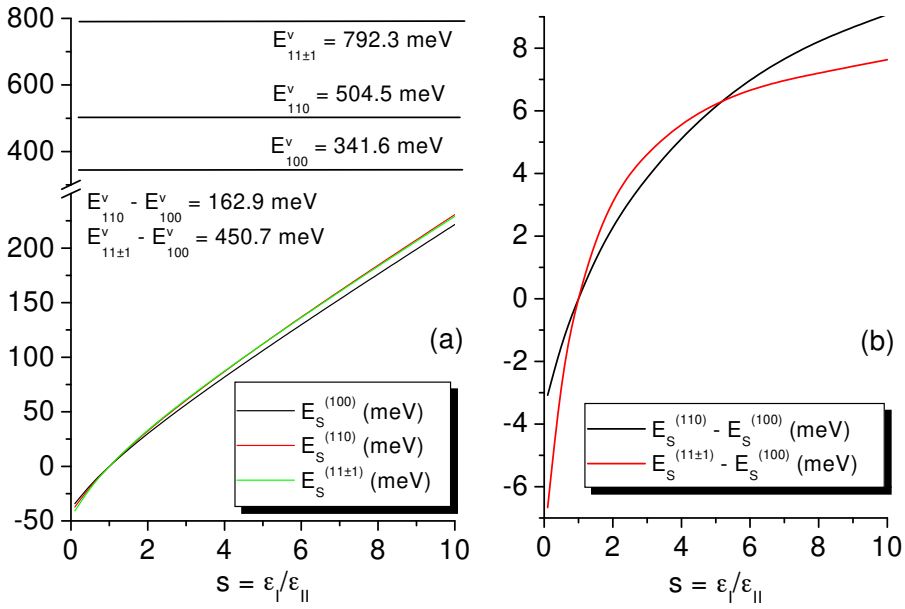

Figure 2.10: (a) The correction due to the dielectric self-interaction to the ground and two excited states of a CdSe ellipsoid quantum dot ($\varepsilon_I = 10.0$) with $a = 2.5$ nm and $c = 5.0$ nm ($\chi = 2.0$). The energy levels calculated without taking into account the dielectric contribution are also shown for comparison. (b) The correction to the first two allowed transition energies, as calculated by making the difference of the curves shown in (a).

experimental point of view), the result shows that these energies have quite small variations for effect of the dielectric contribution. These means that the electronic spectrum is in practice almost rigidly shifted upwards, while the absorption/emission energies keep almost unchanged [121]. Moreover, let us note that the corrections $E_S^{(110)}$ and $E_S^{(11\pm1)}$ (respectively the red and green curves in Fig. 2.10a) are almost coincident. The corrections to the transition energies relative to the first two allowed transitions are shown in Fig. 2.10b, where it is evident that these corrections are of the order of just few meVs. The explanation of why the single-particle transition energies are almost insensitive to the dielectric mismatch is that, as Fig. 2.3 shows, the surface

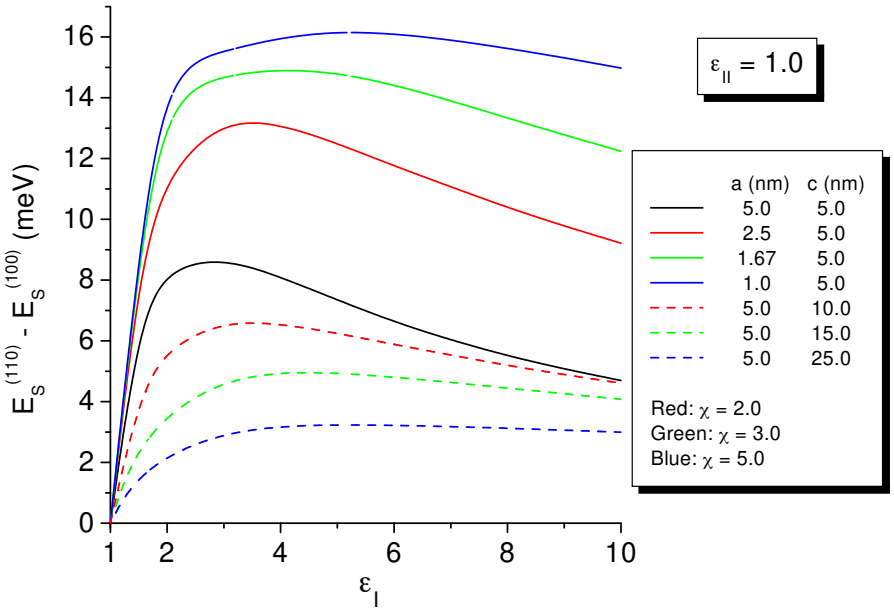

Figure 2.11: Variation of the transition energy relative to the transition $|100> \rightarrow |110>$ for ellipsoid quantum dots embedded in air ($\varepsilon_{II} = 1$) as a function of the dots dielectric constant $s = \varepsilon_I$ for different geometries.

self-interaction potential is a slowly varying function in the space if points not too near to the dot boundary are considered. Therefore, unless we considered very excited states (for which the probability of finding the electron near the surface becomes higher and higher with the energy), the mean value of this potential is almost constant, independently from the state. This is true for the spherical quantum dot as well. In order to clarify how both the geometry and the dielectric mismatch affect the self-interaction energy correction, in Fig. 2.11 it is shown the variation of the transition energy relative to the transition $|100> \rightarrow |110>$ for ellipsoid quantum dots embedded in air ($\varepsilon_{II} = 1$) as a function of the dots dielectric constant $s = \varepsilon_I$ for different geometries. Similarly, Fig. 2.12 shows the same variation but with fixed $\varepsilon_I = 10.0$ (CdSe quantum dots) as a function of s (namely, of the inverse external dielectric constant).

2.2.3 Infrared properties

The calculation of the quantum confined eigenvalues and eigenfunctions for an electron moving inside an ellipsoid dot allows the investigation of some interesting features of the infrared (conduction-band) transitions in such systems. By using the wave function (2.18c) and the eigenvalues (2.18a) the optical matrix elements (2.41) and (2.47) have been calculated for both linearly polarized radiation along the z axis and circularly polarized radiation in the x-y plane relative to transitions from the ground state $|100>$ (absorption process). In this case, according to the selection rules (2.52), the allowed transitions are

$$|100> \rightarrow |nlm> \qquad l = 1, 3, 5, \ldots \qquad |m| = 0, 1, \tag{2.74}$$

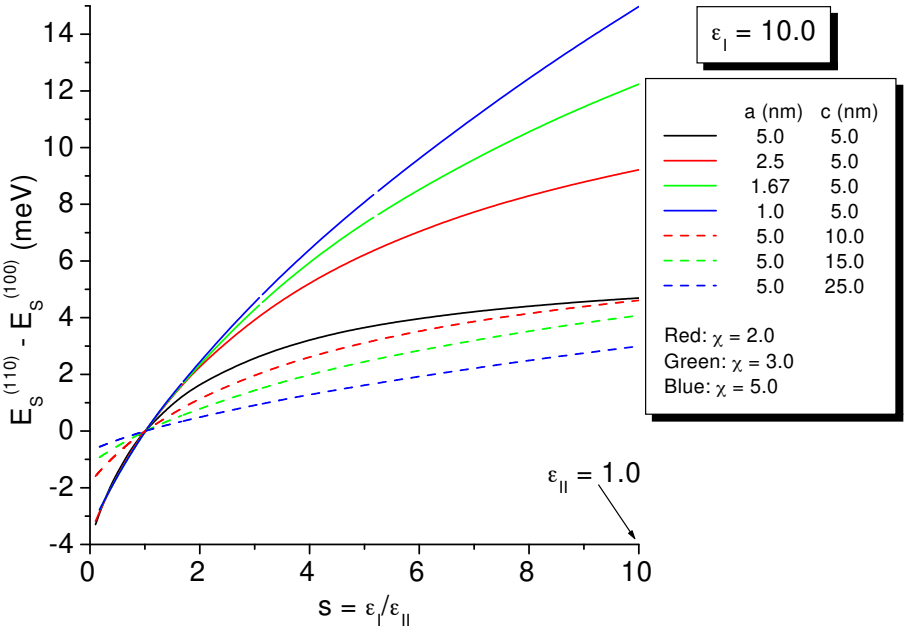

Figure 2.12: Variation of the transition energy relative to the transition $|100> \rightarrow |110>$ for CdSe ellipsoid quantum dots ($\varepsilon_I = 10.0$) as a function of s for different geometries.

where $|m| = 0$ if linearly polarized radiation along the z axis is absorbed, while $|m| = 1$ if circularly polarized radiation in the x-y plane is absorbed. It is worth pointing out that if a given transition is allowed in the dipole approximation with linearly polarized light, it cannot be allowed with circularly polarized light and vice-versa. Therefore, for a given $l = 1, 3, 5, \ldots$, the only non-zero matrix elements of the dipole operator components z, $\frac{x \pm iy}{\sqrt{2}}$ between the ground state and the states $|n\ l\ m = 0, \pm 1 >$ are (in units of c):

$$p_{\parallel} = \left| \frac{1}{c} < 100|z|nl0 > \right|^2 \tag{2.75a}$$

and

$$p_{\perp} = \left| \frac{1}{c} < 100| \frac{x \pm iy}{\sqrt{2}} |nl \mp 1 > \right|^2 . \tag{2.75b}$$

It is straightforward to show that $p_{\parallel}$ and $p_{\perp}$ are functions only of χ and not of a and c separately. The same holds for the oscillator strengths (2.55a) and (2.55b). Because we expect that, differently from the case of the spherical quantum dot, the system response to electro-magnetic radiation must depend on its polarization, it is useful to introduce the optical anisotropy, defined as

$$\rho = \frac{p_{\parallel} - p_{\perp}}{p_{\parallel} + p_{\perp}} = \rho_{\parallel} - \rho_{\perp}, \tag{2.76}$$

where

$$\rho_{\parallel} = \frac{p_{\parallel}}{p_{\parallel} + p_{\perp}} \tag{2.77a}$$

and

$$\rho_{\perp} = \frac{p_{\perp}}{p_{\parallel} + p_{\perp}}. \tag{2.77b}$$

The optical anisotropy ranges between -1 and 1. Positive values correspond to the case in which processes induced by radiation linearly polarized along the z axis are predominant with respect to those induced by radiation circularly polarized in the x-y plane. Negative values correspond to the opposite case. Finally, it is zero for an isotropic system, in which the system response to the radiation does not depend on the polarization. The transitions we are going to consider are given in eq. (2.74) with $n = l = 1$, namely $|100 > \rightarrow |110 >$

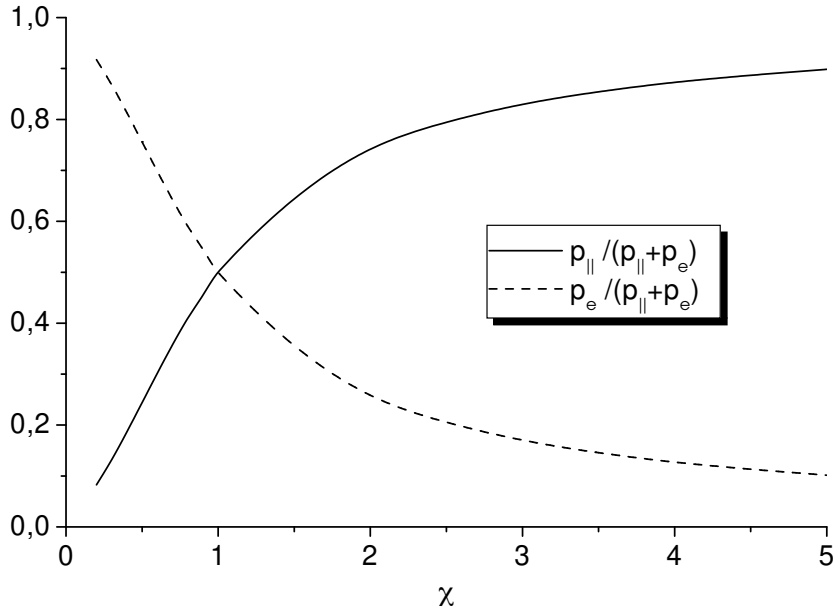

Figure 2.13: $\rho_{\|}$ and $\rho_{\perp}$ as a function of χ. Both for prolate and oblate ellipsoid quantum dots the processes induced by the polarization along the major axis are predominant.

(linear polarization) and $|100> \rightarrow |11 \pm 1>$ (circular polarization). These are the first ones allowed from the ground state. In Fig. 2.13 the quantities $\rho_{\|}$ and $\rho_{\perp}$, defined in eqs. (2.77a) and (2.77b) respectively, are shown as a function of χ. The difference between the two curves gives the optical anisotropy of eq. (2.76) relative to the optical transitions between the ground state and the states with $n = l = 1$. It is seen that the predominant processes are always those which are induced by radiation polarized along the ellipsoid major axis [121] (namely, linearly polarized radiation along the z axis for prolate ellipsoids and circularly polarized radiation in the x-y plane for oblate ellipsoids). This gives a clear evidence to the fact that by realizing anisotropic systems, polarization-dependent processes are obtained. The more the dot geometry is different from the spherical one, the more "anisotropic" is its response to polarized radiation. This result is related to the quantum states

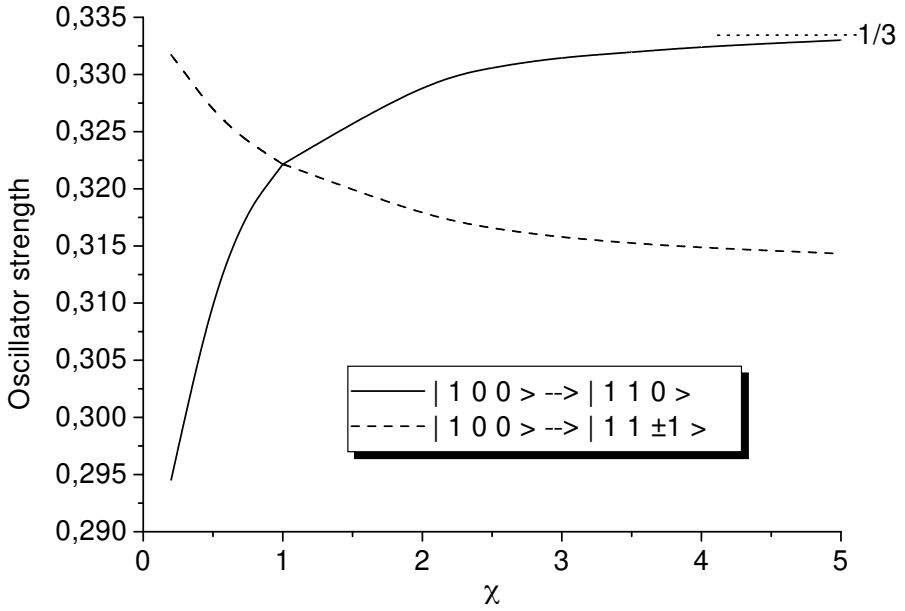

Figure 2.14: The oscillator strengths (2.55a) and (2.55b) as a function of χ. The dependence on the dot geometry is not very strong, but reveals interesting features (see text).

deformation due to the geometry, which leads to $n = 1, l = 1$ states whose spatial configuration is strongly dependent on m (see Fig. 2.9). In Fig. 2.14 the oscillator strengths (2.55a) and (2.55b) are shown for the same transitions. It comes out that there is not a very strong variation with the dot geometry, unless very anisotropic systems are considered. Nevertheless, we can see that for prolate ellipsoids ($\chi > 1$) the oscillator strength relative to the transition allowed with linearly polarized light (namely, $f^{(0)}_{|100>\to|110>}$) saturates towards 1/3 which means, according to the sum rule (2.56a), that higher energy transitions with linearly polarized light (for example towards the states $|130>$ or $|210>$) become more and more inefficient as χ increases. The opposite behaviour has the oscillator strength relative to the transition allowed with circularly polarized light (namely, $f^{(\pm1)}_{|100>\to|11\pm1>}$), showing that higher energy transitions allowed with circularly polarized polarization can

be observed if the dot anisotropy is increased. The role of the polarizations is inverted if oblate ellipsoids are considered. This also shows as polarization dependent measurements (for example of the oscillator strength) can allow to distinguish between prolate and oblate ellipsoids.

Finally, let us note that if the sum rule (2.54) is performed for the transitions from the ground state to the three states with $n = l = 1$, values of about 0.96 are obtained. If the transitions towards the states with $n = 1$, $l = 3$ are included, the value of the sum becomes about 0.99. This clearly shows how for confined systems the oscillator strengths become concentrated over very few, sharp transitions.

2.2.4 Two-electron ground state calculation

In this subsection the results relative to the two-electron ground-state properties in a prolate ellipsoid quantum dot are presented and discussed [130].

In the single-particle picture (see subsecs. 2.2.1 and 2.2.2) the total single-electron energy $E^{(1)}_{n,l,m}$ is the sum of two contributions, the confinement (kinetic) energy $E^{v}_{n,l,m}$ (calculated by exactly solving the Schrödinger equation within the ellipsoid region) and the self-interaction energy $E_s^{(n,l,m)}$ (calculated as a first order correction to the kinetic energy), as shown in eq. (2.70). Starting from this single-particle picture, the two-electron ground state has been investigated, looking in particular for the dependence of the electron-electron correlation on the dot geometry. The ground-state energy has been first calculated in the strong confinement regime, that is, by taking the Coulomb interaction, self-interaction potential and surface interaction mean values on the uncorrelated ground-state wave function (2.57). We get

$$E_0^{(2)} = 2E^{v}_{1,0,0} + E_C^{(1,0,0)} + 2E_S^{(1,0,0)} + E_P^{(1,0,0)}, \tag{2.78}$$

where

$$E_C^{(1,0,0)} = \frac{\left\langle \Psi_0^{(2)}(\vec{r}_1,\vec{r}_2)\,|-eV_C(|\vec{r}_1-\vec{r}_2|)|\,\Psi_0^{(2)}(\vec{r}_1,\vec{r}_2)\right\rangle}{\left\langle \Psi_0^{(2)}(\vec{r}_1,\vec{r}_2)\,|\,\Psi_0^{(2)}(\vec{r}_1,\vec{r}_2)\right\rangle} = \frac{e^2}{4\pi\varepsilon_0\varepsilon_I c} e_C^{(1,0,0)}(\chi)\,, \tag{2.79}$$

$$E_P^{(1,0,0)} = \frac{\left\langle \Psi_0^{(2)}(\vec{r}_1,\vec{r}_2)\,|-e\Phi_P(\vec{r}_1,\vec{r}_2)|\,\Psi_0^{(2)}(\vec{r}_1,\vec{r}_2)\right\rangle}{\left\langle \Psi_0^{(2)}(\vec{r}_1,\vec{r}_2)\,|\,\Psi_0^{(2)}(\vec{r}_1,\vec{r}_2)\right\rangle} = \frac{e^2}{4\pi\varepsilon_0\varepsilon_I c} e_P^{(1,0,0)}(\chi)\,. \tag{2.80}$$

As for the surface self-interaction correction, a polynomial interpolation has been calculated for the surface electron-electron interaction:

$$e_P^{(1,0,0)}(s,\chi) = b_0(s) + b_1(s)\chi + b_2(s)\chi^2 + b_3(s)\chi^3, \tag{2.81}$$

with $1 \leq \chi \leq 5$. The coefficients b_i are given in Table 2.4 for some values of s. As $\chi \to 1$ the previous formulas give $e_P^{(1,0,0)} = s-1$ as it is for the spherical quantum dot [126]. Finally, the Coulomb energy has been calculated, giving

$$e_C^{(1,0,0)}(\chi) = 1.77404 + 1.11755\,|\chi - 1.00962|^{0.85486}\,. \tag{2.82}$$

Even in this case the spherical quantum dot limit [108] is obtained as $\chi \to 1$.

The strong confinement regime description presented above treats the electrostatic contributions to the two-electron ground state as "small" corrections to their kinetic energy. However, it is known [16] that as the dot dimensions increase, this calculation scheme cannot realistically describe the system, because the electrostatic terms become comparable with the electrons kinetic energy. Therefore, as explained in subsec. 2.1.4, a variational calculation has been performed by choosing the trial wave function as shown in eq. (2.59) to take into account correlation effects for geometries which cannot be described within the strong confinement picture. The energy functional (2.61) has been minimized, for different values of χ, with respect to

s	b_0	b_1	b_2	b_3
0.1	-0.27246	-0.63340	$+0.00514$	$+0.00119$
0.5	-0.15523	-0.35255	$+0.00801$	$-1.06126 \cdot 10^{-5}$
3.0	$+0.60112$	$+1.52815$	-0.14044	$+0.01235$
10.0	$+2.39414$	$+7.62111$	-1.10527	$+0.09866$
15.0	$+3.55329$	$+12.20102$	-1.90988	$+0.16719$

Table 2.4: The coefficients of eq. (2.81) for some values of s.

the three parameters α, β, γ ($\alpha_{\min}, \beta_{\min}, \gamma_{\min}$ will indicate their respective values at the minimum point). First the results obtained without taking into account the dielectric effects will be shown, so that a better understanding of the role played by the Coulomb repulsion can be reached. The implications of dielectric effects will be discussed later. In Fig. 2.15 the result of this calculation performed for CdSe ellipsoidal quantum dots ($m^*/m_e = 0.13$, $\varepsilon_I = 10.0$), with fixed $a = 12$ nm, as a function of $c = a\chi$ is shown. The black line represents the energy functional calculated at its minimum point (that is, $E^{(2)} \equiv E[\alpha_{\min}, \beta_{\min}, \gamma_{\min}]$), the red one the same energy but calculated by setting $\beta = 0$ (that is, $E[\alpha_{\min}, 0, \gamma_{\min}]$, which takes into account only the electron-electron correlation along the z direction) and the green one the ground-state energy in the strong confinement regime (which is given by eq. (2.78) and corresponds to setting $\alpha = 0$ in eq. (2.61)). It comes out that on increasing χ or, equivalently, c, the ground-state energy (black line) becomes coincident with the energy calculated taking into account only the electron-electron correlation along the z direction (red line). This means that for $\chi >> 1$ the electron-electron correlation in the x-y plane is negligible, as expected. In fact, on increasing c with fixed a, longer and longer quantum rods are obtained. The total ground-state energy arises from the contribution of both the confinement energy which is minimum if both the electrons are in the ellipsoid centre, and their Coulomb repulsion, which pushes the electrons far from each other, towards the ellipsoid boundary. The minimum energy configuration is reached with the two electrons placed along the z axis, in such a way that they stay as much as possible far from each other and from the ellipsoid boundary. On the contrary, as $\chi \to 1$ (spherical quantum dot limit) we obtain that $E[\alpha_{\min}, 0, \gamma_{\min}]$ becomes coincident with the uncorrelated ground-state energy. In other words, if only the electron-electron correlation along a particular direction (the z axis in this case) is taken into account, the same result as using the strong confinement regime approach is obtained. This reflects the spherical symmetry of the problem, which cannot give rise to a ground-state configuration in which the two electrons are placed along some privileged direction. It is worth noting that a variational approach for the two-electron ground state in CdS spherical quantum dots has been done, using a different trial wave function, in [108]. These energies

have been calculated by using the variational approach explained in subsec. 2.1.4 and exactly the same results have been obtained. A quite important check for the calculation is that, in this case, $\beta_{\min}/\gamma_{\min} \simeq 1$ within at most 1%.

The inset of Fig. 2.15 shows the values of α calculated with fixed $a = 12$ nm as a function of c, without ($s = 1$, black line) and with ($s = 10$, red line) dielectric effects. On increasing c it is seen that $\alpha \to 1$, which corresponds to a null probability of finding the electrons at the same point. This further brings out the strong relation between the electron-electron correlation and

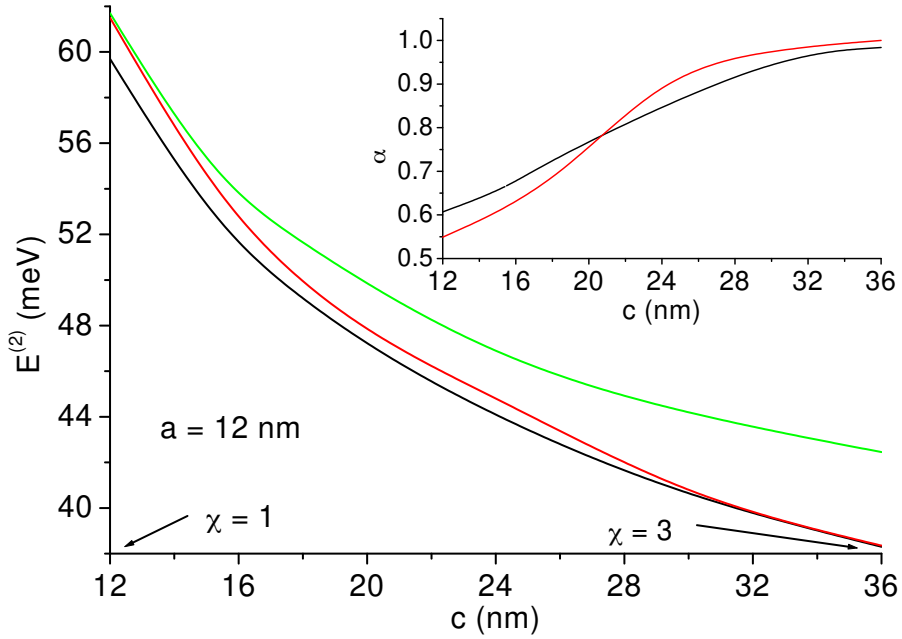

Figure 2.15: The ground-state energy calculated by using the variational method is shown (black line) for CdSe quantum dots, with fixed $a = 12$ nm as a function of c. Dielectric effects have not been included. The energies calculated by taking into account only the electron-electron correlation along the z axis ($\beta = 0$, red line) and for uncorrelated electrons ($\alpha = 0$, green line) are shown for comparison. The inset shows the value of α at the minimum point as a function of c calculated without ($s = 1$, black line) and with ($s = 10$, red line) dielectric effects.

the dot geometry.

The projection of the pair correlation function (that is, the probability of finding one electron at $\vec{r}_1$ if the second one is at $\vec{r}_2$ given by $|\Psi(\vec{r}_1, \vec{r}_2)|^2$) in the x-z plane is plotted for a CdSe ellipsoid quantum dot with $a = 12$ nm and $c = 24$ nm in Fig. 2.16. The results obtained both without and with dielectric effects (these last ones will be discussed later) are shown respectively in the parts a and b of the figure. The pair correlation function is plotted for different positions of the fixed electron (indicated with a big dot), to better understand the ground-state spatial configuration. The yellow regions correspond to a maximum of the function. As already stressed previously, the configuration with maximum probability is with the two electrons placed along the ellipsoid major axis.

The electron-electron interaction affects also the correlation energy, defined as $E_{\text{corr}} = E^{(2)} - E_0^{(2)}$ (that is, the difference between the black line and the green one in Fig. 2.15). In Fig. 2.17a the ratio $E_{\text{corr}}/E^{(2)}$ (that is, the relative error done if the uncorrelated ground-state energy is assumed) for three values of a as a function of χ is shown. It is an increasing function of both a and c. All the obtained results clearly show that for long quantum rods the system description within the strong confinement regime becomes misleading. The same variational technique has been used including dielectric effects for studying how they can affect the electron-electron correlation. The numerical results obtained for the two-electron ground state of CdSe ellipsoidal nanocrystals, with fixed $a = 12$ nm and $s = 10$ as a function of c are shown in Table 2.5. For each value of c, the kinetic energy $2K$, the Coulomb repulsion E_c, the surface self-interaction energy $2E_s$ and the surface electron-electron interaction energy E_p are calculated both within the described variational technique and in the strong confinement regime ($\alpha = 0$). It comes out that the more the two electrons have the possibility to be far from each other (on increasing c) the more the correlation energy associated with their Coulomb repulsion increases. Moreover, there is a quite relevant contribution to this correlation energy arising from the surface electron-electron interaction for high dot anisotropies. This can be explained by considering that this interaction pushes the electrons far from each other, even if it is less strong than the direct Coulomb repulsion. Therefore this contribution to the correlation

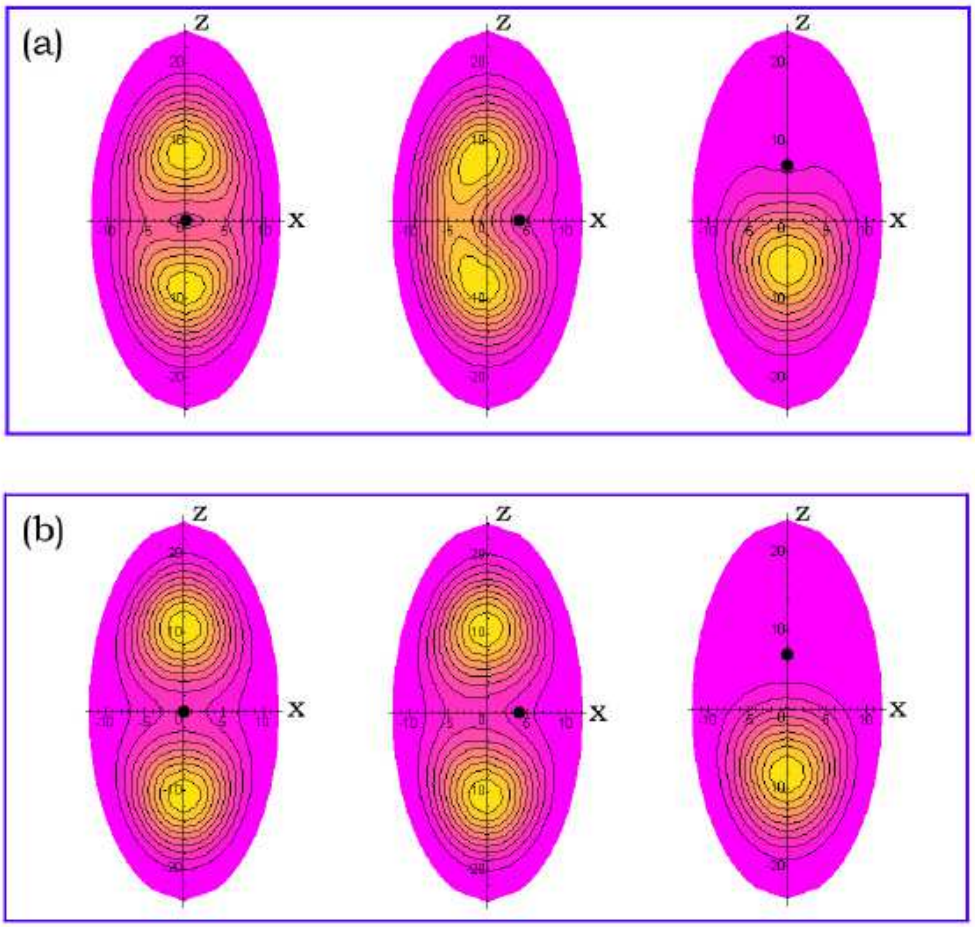

Figure 2.16: Projection of the pair correlation function in the x-z plane for a CdSe ellipsoidal quantum dot with $a = 12$ nm and $c = 24$ nm. The results obtained both (a) without and (b) with dielectric effects are shown. The position of one electron is taken fixed and is indicated with a big dot. The yellow regions correspond to a maximum of this function. The effect of the dielectric mismatch spatial configuration of the two electrons clearly comes out (see text).

energy becomes more significant on increasing c, because in this case the electrons quantum confinement decreases and their surface interaction is able to push them far from each other, towards the ellipsoid boundary. This is also

	$c = 12.0012$ nm		$c = 18$ nm	
	$\alpha = \alpha_{\min}$	$\alpha = 0$	$\alpha = \alpha_{\min}$	$\alpha = 0$
$2K$ (meV)	41.34	40.17	34.12	32.55
E_c (meV)	18.34	21.53	14.97	19.10
$2E_s$ (meV)	117.4	116.5	102.8	101.7
E_p (meV)	107.4	108.0	92.42	93.57

	$c = 24$ nm		$c = 36$ nm	
	$\alpha = \alpha_{\min}$	$\alpha = 0$	$\alpha = \alpha_{\min}$	$\alpha = 0$
$2K$ (meV)	33.11	29.65	32.24	27.27
E_c (meV)	11.02	17.21	6.478	15.18
$2E_s$ (meV)	94.49	92.35	84.87	81.30
E_p (meV)	80.22	83.90	62.72	71.90

Table 2.5: Two-electron ground-state kinetic ($2K$), Coulomb (E_c), surface self-interaction ($2E_s$) and surface interaction (E_p) energies calculated for CdSe ellipsoidal quantum dots with fixed $a = 12$ nm and $s = 10$ as a function of c. Both the strong confinement regime and the variational results are shown. It comes out that on increasing the dot major axis a quite relevant contribution to the correlation energy arises from the surface interaction energy.

supported from the fact that, on the contrary, on increasing c the surface self-interaction energy calculated on the uncorrelated wave function becomes smaller and smaller than the one calculated at the minimum point, showing that the electrons are farther and farther from the ellipsoid centre. This result is confirmed by comparing the values of $\alpha_{\min}$ in the inset of Fig. 2.15 calculated without ($s = 1$, black line) and with ($s = 10$, red line) dielectric effects. It is clear that by including dielectric effects, for nearly spherical quantum dots smaller values are obtained (because the surface self-interaction potential pushes the electrons towards the ellipsoid centre), while on increasing c greater values are obtained, because of the additional contribution to the electron-electron correlation energy due to the surface interaction. The same

comparison can be done on the pair correlation function, as in Fig. 2.16. It comes out that the inclusion of dielectric effects in the minimization of the functional (2.61) leads to a ground-state wave function where the distance between the two electrons has increased with respect to the case $s = 1$. A final check of these results is given in Fig. 2.17b, where the correlation energy obtained by taking into account only the Coulomb repulsion ($s = 1$, black line) and the one calculated by including dielectric effects ($s = 5$, red line and $s = 10$, green line) are shown. Only for nearly spherical quantum dots the correlation energy is smaller if dielectric effects are not included.

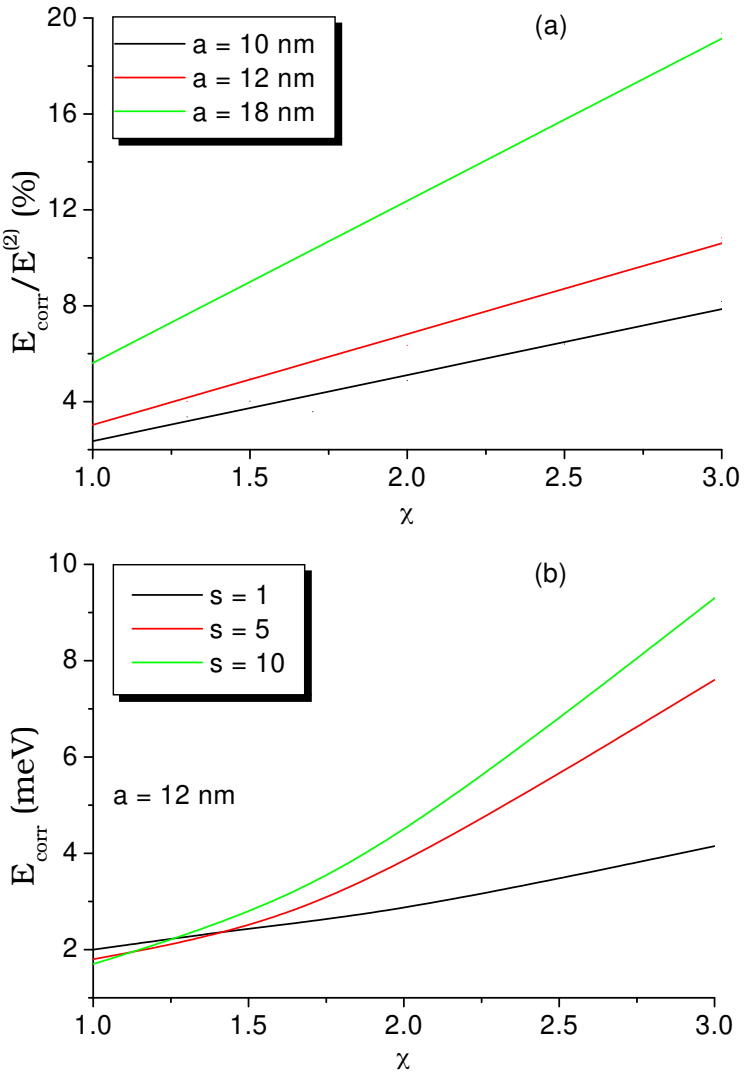

Figure 2.17: (a) The ratio $E_{\rm corr}/E^{(2)}$ (relative error done if the uncorrelated ground-state energy is assumed) for three values of a as a function of χ is shown. Dielectric effects have not been included. The effect of the Coulomb electron-electron correlation becomes relevant on increasing a and/or c. (b) The total correlation energy calculated for $a = 12$ nm as a function of χ is shown for three values of the dielectric mismatch s. The contribution of the surface electron-electron interaction clearly comes out on increasing χ.

Finally, in Fig. 2.18 the energy difference Δ between the one- and two-electron ground-state energies is shown, for CdSe nanocrystals with $a = 12$ nm, as a function of χ and for several values of the dielectric mismatch s. It is a decreasing function of χ. This dependence becomes stronger and stronger as $\varepsilon_{II} \to 1$ ($s = 10$). If Δ is plotted as a function of ε_{II} we get that, in the same limit, a strong increase of Δ is observed, in accordance with the results shown in [137].

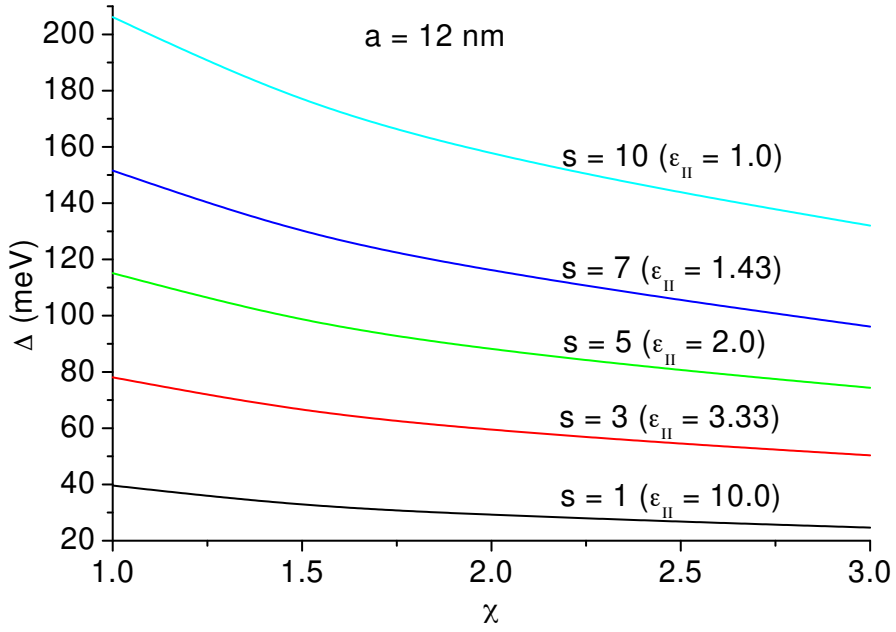

Figure 2.18: The difference Δ between the energies of the one- and two-electron ground state is shown for several values of s. It is a decreasing function of χ. This shape dependence becomes very strong as $\varepsilon_{II} \to 1$.

Chapter 3

A variational approach to quantum confinement

As already pointed out in chapter 1, small crystallites ($10 - 1000$ atoms) exhibit structural and physical properties distinct from those of the corresponding bulk system. The electronic properties are strongly size-dependent and quantum effects are relevant if the dimensions are smaller than a typical value (about 5 nm in silicon). For such a dimension, less than 15% atoms are surface atoms although this figure increases on reducing the dimensions. In other words, surface and bulk will compete for the material electronic properties control for small crystallites sizes. The crossover will depend on the particular material and it is not clear when it occurs, if it occurs neatly. When the surface is the dominating element, we can expect that the electronic properties are strongly "receptive" to environment changes: small crystallites become sensitive to the environment as far as an overlap occurs between the crystallite and the external molecule wave functions. It is expected that variations of dimensions and surface chemistry determine the fundamental properties of such structures opening the way to new adsorption, electro-physical and optical responses to a gas environment.

Porous silicon is a typical example of this class of materials [138]. It is obtained from crystalline doped (either p or n) silicon by an electro-chemical etching. The process results in a porous structure mainly composed by a not ordered network of silicon wires and dots [139] with dimensions as small as a

few nanometres. For example, in Fig. 3.1 TEM images of thin, high porosity Si layers are shown. Columnar Si structures are indicated by the arrows. The most spectacular feature of porous silicon is its ability of emitting very intense visible light at room temperature with an efficiency of several percent [140]. Although the spectrum is broad, the photoluminescence peak energy can be tuned from the infrared to the visible varying the processing conditions. It is widely accepted that the strong photoluminescence emission in porous silicon originates from localized electronic states in a quantum wire structure. The combination of small nanostructure dimensions and high surface to volume ratio makes porous silicon a good candidate both for technological sensor

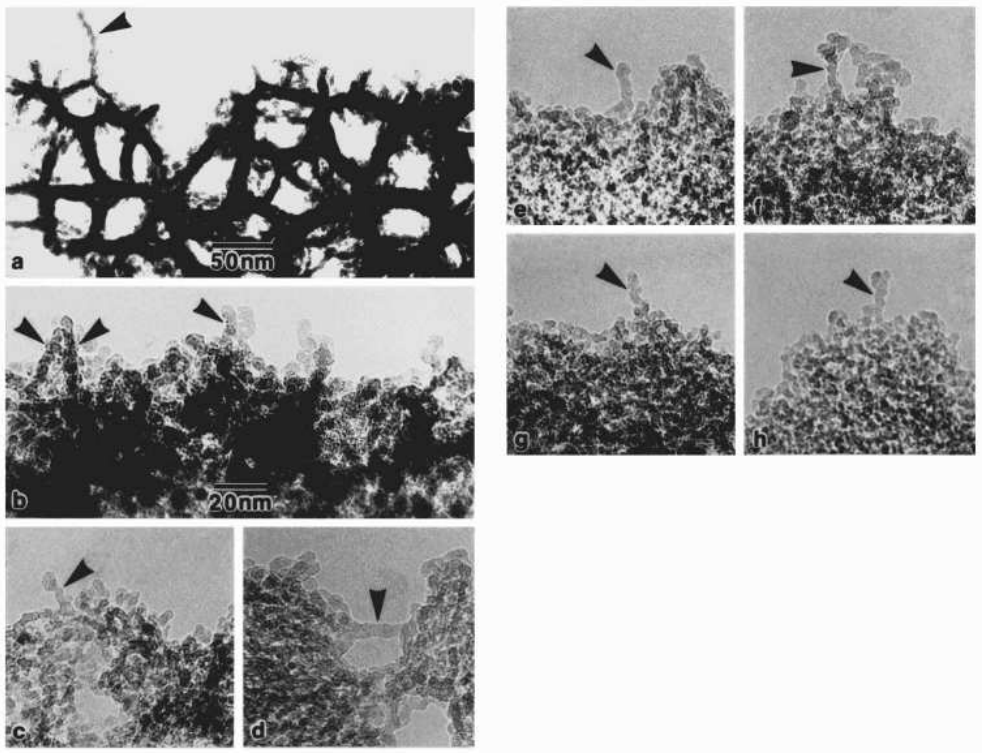

Figure 3.1: TEM images of thin, high porosity non-luminescent (a) and luminescent (b)-(h) Si layers. Columnar Si structures are indicated by the arrows (from ref. [140]).

applications [141–144] and to understand the quantum physical properties of the nanosystems.

It is important to stress that the study of the sensing properties of very small systems is a very general problem which concerns a wide class of materials. The fundamental point is the comprehension of how the electrical and optical properties of such materials are related to the lower dimensionality. Just to give a further example, in Fig. 3.2 scanning electron microscope images of silicon nanowires are shown. The wires are maintained by two-electrode pads (air bridge structure) and are fabricated by micro-machining a silicon-on-insulator (SOI) substrate [145]. The current-voltage characteristics of such wires show an anomalous behaviour of the electric conductivity, related to the interaction with the external environment (that is, the absorption of external molecules on the wire surface).

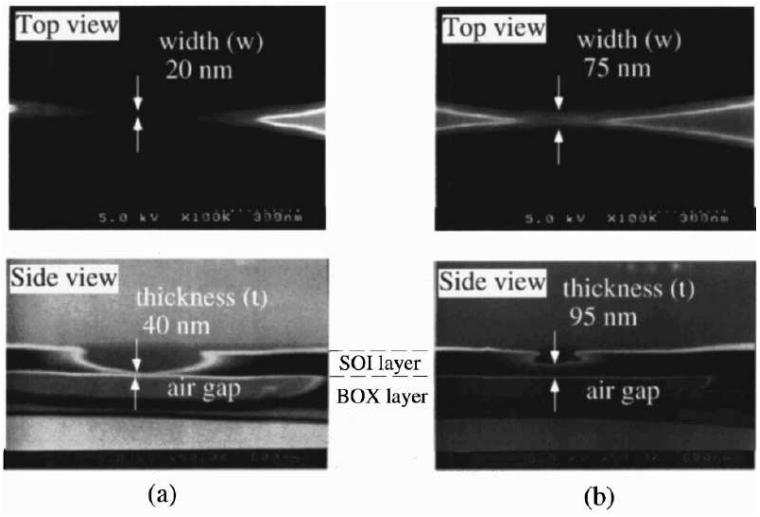

Figure 3.2: Scanning electron microscope images of silicon nanowires (a) 20 nm in width and 40 nm in thickness and (b) 74 nm in width and 95 nm in thickness. The wires are maintained by two-electrode pads (air bridge structure) and are fabricated by micro-machining a silicon-on-insulator (SOI) substrate (from ref. [145]).

In this chapter it is presented a theory for the description of the electronic spectrum in confined systems of arbitrary shape by taking into account also the effects of the environment (subsec. 3.1.1). Explicit calculations for nanometric deformed wires are shown (subsec. 3.1.2) . The aim is to explain the behaviour of both the absorption and emission of light in porous silicon and the modification induced by the external gas. The basic idea is that quantum confinement within an undulating wire can give rise to a localized electronic state within each undulation. The undulating morphology is supported from structural measurements, as those shown in Fig. 3.1. Moreover, the large Stokes shift between light absorption and emission [146], the temperature dependence of the electrical conductivity [147], the co-existence of phonon-assisted and no phonon optical transitions [148] and a number of time-resolved non-linear optical experiments which give information on the photo-generated carrier dynamics [149, 150], are all evidence of the presence of this type of states.

Some results obtained for the porous silicon absorption and emission spectra have been obtained, showing in particular how the presence of localized states within a quantum wire structure allows to explain the presence of the large Stokes shift mentioned above (subsec. 3.2.1). Moreover, some experimental results related to photoluminescence changes induced by an oxygen atmosphere are discussed and interpreted (subsec. 3.2.2). It is shown that the model is able to explain both the red-shift and the quenching of the photoluminescence, which gives a strong support to the theory.

Finally, the accuracy of the variational approach in determining accurately the ground-state properties of anisotropic systems is checked, by applying it to an ellipsoid quantum dot and comparing the results with the exact ones shown in chapter 2 (subsec. 3.2.3).

3.1 Theory

In this section it is described the general method which allows to approach the study of arbitrarily shaped nanostructures, with the possibility of taking into account in a quite simple way the effects due to the finite potential

barrier at the nanostructure boundary as well as the interaction with an external environment via the surface.

3.1.1 The variational approach

Let us consider a particle moving within a confined region of arbitrary form and indicate with S its surface. If finite boundary conditions at S are considered (namely, the probability of finding the particle outside that region in not zero), the effective-mass Schrödinger equation which describes the motion of the particle within an additional external potential $v(\vec{r})$ is

$$-\frac{\hbar^2}{2m^*}\overrightarrow{\nabla}^2\Psi(\vec{r}) + v(\vec{r})\Psi(\vec{r}) = E\Psi(\vec{r}), \tag{3.1}$$

together with the boundary condition

$$\left[\frac{1}{\Psi(\vec{r}_S)}\frac{\partial\Psi}{\partial n}\right]_{\text{in}} = \left[\frac{1}{\Psi(\vec{r}_S)}\frac{\partial\Psi}{\partial n}\right]_{\text{out}} = -\lambda(\vec{r}_S), \tag{3.2}$$

where $\vec{r}_S \in S$, $\partial/\partial n$ indicates the normal derivative at a given point of S and the subscripts "in" and "out" indicate that the normal derivative is calculated respectively from inside and outside the surface[1]. Eq. (3.2) gives the matching of the wave function at the dot boundary and can be rewritten as:

$$\left[\frac{\partial\Psi}{\partial n} + \lambda\Psi\right]_{\vec{r}\in S} = 0. \tag{3.3}$$

The function $\lambda(\vec{r})$ is defined on S and is nothing other than the logarithmic normal derivative of the wave function (changed of sign) calculated on S.

Let us consider the functional

$$E[\Psi] = \frac{\hbar^2}{2m^*}\frac{1}{\displaystyle\int_V \Psi^2 dV}\left[\int_V \left[(\overrightarrow{\nabla}\Psi)^2 + \widetilde{v}\Psi^2\right] dV + \oint_S \lambda\Psi^2 dS\right], \tag{3.4}$$

where all the integrals are done on the volume V of the confined system except the last at the right hand that is an integral on the surface S containing the

[1]It is worth stressing that the versus of the normal to S can be arbitrarily fixed but must be the same in the calculation of "in" and "out" normal derivatives.

system. $\widetilde{v}$ is the single-particle external potential in units of $\hbar^2/2m^*$. It can be shown [151–154] that the condition that the functional (3.4) is stationary with respect to an arbitrary variation $\delta\Psi$ of Ψ (namely, $\delta E = 0$) implies that the wave function Ψ satisfies both the Schrödinger equation (3.1) in the volume of the system and the boundary condition (3.3). Therefore, by looking for the extremum points of $E[\Psi]$ it is possible to automatically take into account the finite boundary conditions at S. This is a very important conceptual point. In fact, the "standard" solution of the problem would require the solution of eq. (3.1) both inside and outside the nanostructure and, as a second step, the determination of the particle spectrum by imposing the matching condition (3.2). This last step, even if in principle possible, can become very demanding for complicated geometries, due to the fact that it is not possible, in general, to find a suitable coordinates system in which both the Schrödinger equation and the boundary condition are separable (an exception is given, for example, by the quantum confinement of a particle within an ellipsoid quantum dot with hard wall boundary conditions, as shown in chapter 2). Instead, within the variational approach we are discussing, the probability density outside the wire can be accounted for just by performing a suitable choice of the function λ. In other words, the knowledge of the wave function Ψ inside the nanostructure (namely, the volume V) together with its normal logarithmic derivative on the surface S is enough to completely describe the system, the actual values of Ψ outside V not being needed. This makes the functional (3.4) very general and suitable to study the electronic structure of quantum nanostructures of any shape. Let us stress once again that this flexibility is due just to the inclusion of the boundary condition in an integral form in eq. (3.4), which prevents from performing the wave function matching (3.2) at S.

There is another fundamental point of this theory which is worth bringing out. The surface physics is lumped in the function λ which can be interpreted as the spatial wave function decay outside the system[2]. This decay depends

[2]If simple geometries, like a spherical quantum dot or a cylindrical quantum wire, are considered, the exact solution of the problem for a step potential barrier ($\widetilde{v} = \widetilde{v}_0 \equiv$ constant > 0 outside the nanostructure and 0 elsewhere) can be found. It comes out that quantum states confined within the nanostructure exponentially decay outside it with an

on the microscopic details of the gas-surface interaction which, in the case of porous silicon, can be extremely complex. In general, one can say that gas adsorption gives rise to a modification of both the density of surface states and of surface electric dipoles. A particle (electron or hole) inside the nanostructure will be confined by an effective potential barrier (confining potential) whose variations are localized near the surface S with a height which depends on both the nature of the adsorbed gas and the surface passivation. When an oxidizing or reducing gas interacts with the nanostructure surface, the local charge transfer induces electric dipoles which can give either a positive or a negative contribution to the confining potential. These potential height variations may significantly change the quantum wire electronic structure to a point where a clear signature is detectable in the optical and transport properties. This effect becomes important on reducing the nanostructure dimensions. In this respect the gas sensing mechanism is strictly related to the dimensionality of the system.

It is not easy, in general, to understand how the external gas can modify the nanostructure surface properties and, in particular, the barrier height. Microscopic models and atomistic calculations can be performed only if the total number of atoms is low. The advantage of this model is that the modifications at the nanostructure surface are averaged and taken into account just via the function λ, following the basic idea that the macroscopic property which is changing as effect of the presence of the external gas is the barrier height and, therefore, the wave function decay outside the nanostructure. The drawback is that the information about what it is happening at microscopic level is lost.

If $v_0(\vec{r}_S)$ is the barrier height at a point $\vec{r}_S$ of the surface layer, the wave function decay $\lambda(\vec{r}_S)$ is approximately given by

$$\lambda(\vec{r}_S) = \sqrt{\frac{2m^*}{\hbar^2}[v_0(\vec{r}_S) - E]}, \tag{3.5}$$

where E is the eigenvalue corresponding to the quantum confined state[3]. The

exponential law $\exp(-\lambda|\vec{r}|)$ [155].

[3]For a spherical quantum dot and a cylindrical quantum wire eq. (3.5) is independent from $\vec{r}_S$ and is a good approximation to the actual value of λ.

form (3.5) of λ makes the solution of the variational problem difficult, because it is necessary to proceed by attempts to obtain the self-consistency between the fixed value of the energy in (3.5) and that calculated by minimizing the functional (3.4).

It is worth pointing out that, for states localized inside the wire (the ones we are interested in), $\lambda > 0$ (as we have said previously, λ^{-1} can be interpreted as the wave function decay outside the wire). Under this assumption it can be shown that the condition $\delta E = 0$ leads to a minimum of the functional (3.4).

3.1.2 Deformed cylindrical wire

Let us consider a deformed cylindrical quantum wire with rotational symmetry around the z axis. If we indicate with ρ, z, φ the cylindrical coordinates, the wire boundary can be described by using the following parametric equations:

$$\begin{cases} x = R(u)\cos\varphi \\ y = R(u)\sin\varphi \\ z = u \end{cases}, \tag{3.6}$$

where $-\infty < u < +\infty$ and $0 \leq \varphi < 2\pi$. The parametric equations (3.6) are equivalent to the single equation $\rho = R(z)$. The interest in solving eq. (3.1) with the boundary condition (3.3) for such system is given from the fact that, as already pointed out previously, absorption and emission spectra of porous silicon can be explained as an effect of quantum confinement. One possibility is, as we are going to see, that the wire-like configuration shown in Fig. 3.1 induces quantum confinement in correspondence of wire bulges, as it can be easily explained with the uncertainty principle. Let us consider a deformed quantum wire as shown in Fig. 3.3. We indicate with R_0 the radius of the undeformed part of the wire, with Δz the bulge width and with βR_0 the bulge depth. It must be stressed that the geometry shown in Fig. 3.3 represents just a simplified, average nanostructure. It is expected that in a real sample (as shown in Fig. 3.1) there are many bulges and that the wire and bulge dimensions follow a certain distribution. Nevertheless, as it will be explained better in the following (see subsec. 3.2.1), the hypothesis is that

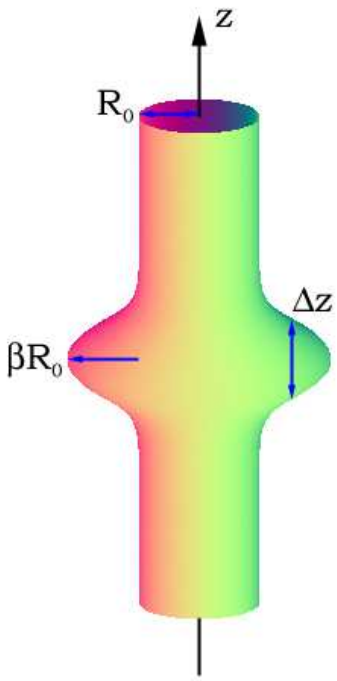

Figure 3.3: A deformed quantum wire. Explicit calculations will be performed by assuming a Gaussian shape. R_0 represents the radius of the undeformed part of the wire, Δz the width of the bulge and βR_0 its depth.

the distance between two neighbouring bulges is large enough to make their "interaction" negligible and that the distribution of their dimensions is sharp enough to make the average description "realistic".

If a particle is moving along the wire axis, near the bulge it must decrease its kinetic energy accordingly to the uncertainty principle (in fact, the presence of the bulge increases the uncertainty on the particle distance from the wire axis). This means that the geometrical deformation shown in Fig. 3.3 will act as an attractive potential for the particle motion along the z axis. The contrary would happen if a bottleneck ($\beta < 0$) were considered instead of the bulge ($\beta > 0$). Starting from the hard wall ground-state wave function of a straight wire ($\beta = 0$, see eq. (2.62a) with $k_z = 0$, $m = 0$ and $n = 1$) it is possible to give a variational ansatz for the particle wave function Ψ, as

follows [151–153]:

$$\Psi(\vec{r}) = J_0 \left[Z \frac{\rho}{R(z)} \right] f(z), \tag{3.7}$$

where J_0 is the zero-order cylindrical Bessel function and Z a variational adjustable parameter used to minimize the total energy consistently with the boundary condition on the wire surface S ($\rho = R(z)$). The choice of the variational wave function (3.7) is justified by the fact that if $Z = Z_{1,0}$ (first zero of J_0) an hard wall wave function is obtained (namely, the function (3.7) becomes zero on the wire boundary $\rho = R(z)$) and that if a straight wire is considered (namely, $R(z) = R_0$ for any z) it becomes the corresponding eigenfunction (2.62a). This wave function takes into account also the fact that because of the cylindrical symmetry of the problem, the ground state must be independent from φ.

The function $f(z)$ describes the particle motion along the wire axis (namely, the z axis). Two classes of states are expected as far as $f(z)$ is concerned. To the first class belong localized states whose z extension is limited within the bulge ($\beta > 0$), according to the qualitative explanation given previously. To the second class belong delocalized states characterized by a z extension which comprises the entire wire, that is, they are very near to be plane waves. As such, they have higher energies and a large density of states and therefore they are the primary candidates for photon absorption. The localized states have the lowest energies and are the ones involved in the photon emission. The large Stokes shift observed for instance in porous silicon can be therefore described in terms of these states whose character is entirely determined by the quantum wire geometry and the surface layer chemistry, as we are going to see in subsec. 3.2.1.

The described typology of electronic structure may have important effects on the carrier transport. Both the direct and frequency dependent conductivity may be significantly modified by the gas environment through the surface barrier variations. The corresponding conductivity variations are, in this case, very sensitive to the nanostructures dimensions: smaller nanostructures will respond better than large nanostructures [156]. However, a theoretical quantitative assessment of these variations requires an understanding of the actual carrier transport mechanism [157].

The nanostructure energy spectrum can be calculated by inserting in eq. (3.4) the wave function (3.7). The volume and surface integrals which appear in eq. (3.4) imply integrals over ρ, z and φ. It is not difficult to show that the integrals over ρ and φ can be analytically performed. The result is that the energy functional (3.4) depends only on $f(z)$. By taking its variation with respect to $f(z)$ and by requiring that $\delta E/\delta f = 0$, it comes out that the function $g(z) = f(z)R(z)$ must satisfy the one-dimensional Schrödinger equation [151–154] (it is supposed that no additional external potential $\widetilde{v}(z)$ is present)

$$-\frac{d^2g}{dz^2}(z) + \widetilde{v}_{\text{eff}}(z)g(z) = \widetilde{\varepsilon}g(z), \tag{3.8}$$

which contains the effective potential

$$\begin{aligned}\widetilde{v}_{\text{eff}}(z) = &-h_1(Z)\left[\frac{R''(z)}{R(z)} - \frac{R'(z)^2}{R(z)^2}\right] + \frac{2}{3}\frac{R'(z)^2}{R(z)^2}h_2(Z) - \frac{1+R'(z)^2}{R(z)^2}h_3(Z)\\ &+h_4(Z)\frac{\lambda(z)}{R(z)}\sqrt{1+R'(z)^2} + \frac{R''(z)}{R(z)} + \frac{Z^2}{R(z)^2},\end{aligned} \tag{3.9}$$

where

$$h_0(Z) = \frac{1}{J_0(Z)^2 + J_1(Z)^2}, \tag{3.10a}$$

$$h_1(Z) = J_1(Z)^2 h_0(Z), \tag{3.10b}$$

$$\begin{aligned}h_2(Z) = &\left[ZJ_0(Z)J_1(Z) + J_1(Z)^2\left(\frac{Z^2}{2} - 1\right) +\right.\\ &\left.\frac{Z^2}{2}J_0(Z)^2\right]h_0(Z),\end{aligned} \tag{3.10c}$$

$$h_3(Z) = 2ZJ_0(Z)J_1(Z)h_0(Z), \tag{3.10d}$$

$$h_4(Z) = 2J_0(Z)^2 h_0(Z). \tag{3.10e}$$

It depends on both the wire surface curvature and the wave function decay λ^{-1}, that is, the surface chemistry.

It must be pointed out that the trial wave function (3.7) does not obviously span all the single-particle Hilbert space. This means that once the effective Schrödinger equation is solved and the minimum energy with respect to Z is found, this does not correspond to the absolute minimum of the

energy, which instead is always overestimated. Nevertheless, if the starting trial wave function is well chosen, this leads to a very good estimation of the ground-state energy, as we shall see later.

If hard wall boundary conditions are used, that is, $\Psi(\vec{r})|_{\vec{r}\in S} = 0$, the potential (3.9) becomes:

$$\widetilde{v}_{\text{eff}}(z) = \frac{Z_{1,0}^2}{R(z)^2} + \frac{1 + Z_{1,0}^2}{3}\frac{R'(z)^2}{R(z)^2}. \tag{3.11}$$

This potential is the sum of two terms. The first one gives the dependence on the deformed wire radius $R(z)$ and corresponds to a pure adiabatic approximation (which consists in substituting in the straight wire spectrum given in eq. (2.62b), the constant radius $a \equiv R_0$ with the z dependent radius). The second term, proportional to $R'(z)^2$, gives the dependence from the wire curvature. In Fig. 3.4 and 3.5 the plot of the potential (3.11) for different bulge geometries is shown. The potential is measured with respect to its asymptotic value, given by $Z_{1,0}^2/R_0^2$, namely the mini-band edge for the straight wire. The bulge aspect ratio $\delta = \beta R_0/\Delta z$ has been defined (let us note that on increasing δ sharper and sharper deformations are considered). It is clear that more confining potentials are obtained if higher values of both β and Δz are considered, provided that not too high aspect ratios values are reached. In fact, as Fig. 3.5 and 3.4 show, small values of Δz and/or high values of β can give rise to positive maxima[4].

[4]A theorem states that for a potential with a negative minimum (referred to its asymptotic value) the existence of a bound state in one and two dimensions is guaranteed [158], no matter how weak the potential is, provided that it has no positive maxima. If positive maxima appear, it is possible that there is no localized state associated to the potential. The implication of this theorem in this case is that one may have a wire with a bulge without any localization. This gives a strong dependence of the system properties on the wire geometry. The results which will be shown demonstrate that for the typical geometries involved in porous silicon structures the existence of the positive maxima in the effective potential is not able to delocalize the ground state (see the discussion at p. 100 for further details).

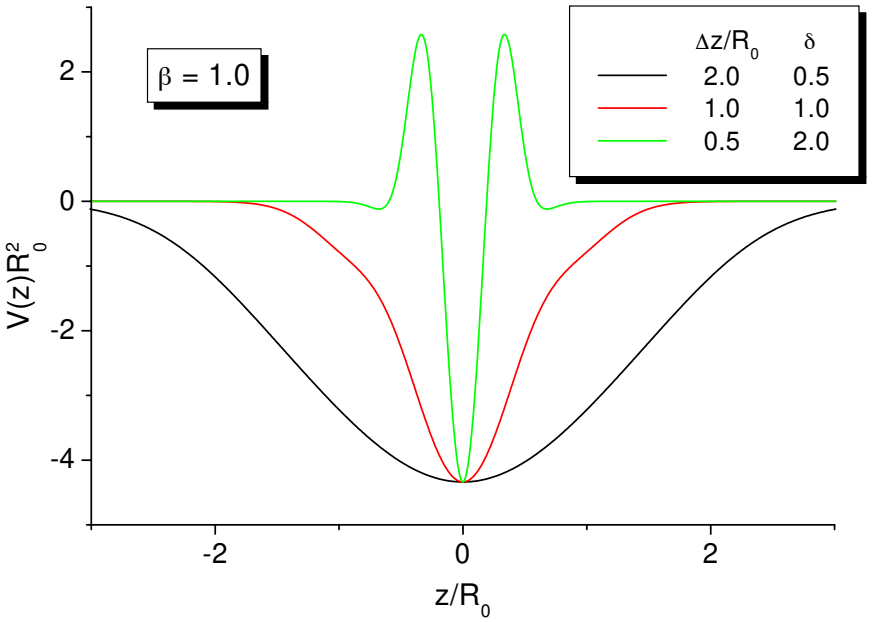

Figure 3.4: The single-particle potential as derived from the variational approach presented above if hard wall boundary conditions are assumed. The potential is referred to its asymptotic value. Different bulge geometries are considered for comparison. β is kept fixed at 1.0, δ is the bulge aspect ratio.

3.2 Results

In this section the main results which come out by studying porous silicon optical properties within the calculation scheme previously discussed are shown. First, the attention will be focused on the light absorption-emission path, showing how it is possible to explain the Stokes shift existing between the absorption and emission spectra. This is done even in the simplest scheme of hard wall boundary conditions.

By preventing the wave function from having a tail outside the quantum wire, it is not obviously possible to study the interaction between the nanostructure and an external environment. The modification of the electronic properties of the nanostructure, in fact, can be understood only by imaging

that the electron or hole wave function interacts with the wave function of an incident external molecule, so that some physical or chemical reaction can take place at the wire surface. Therefore, calculations in the case in which the electron or hole wave function has a non-zero decay length λ^{-1} outside the wire have been performed. It is seen how the model can account for the red-shift and quenching of the photoluminescence in presence of oxygen.

Finally, the validity of the model with hard wall boundary conditions

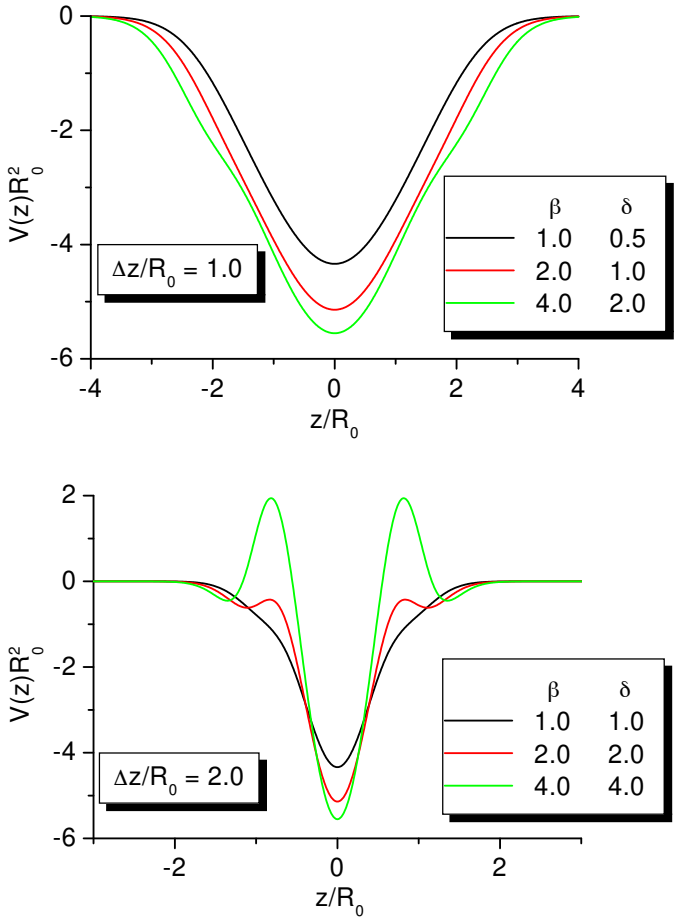

Figure 3.5: The same as in Fig. 3.4, but by keeping fixed $\Delta z/R_0$.

is checked by applying it to an ellipsoid quantum dot, for which the exact calculation has been performed in chapter 2.

3.2.1 Emission and absorption spectra of porous silicon

By using the variational method explained in subsec. 3.1.2, the spectrum of a single particle confined within the region of Fig. 3.3 has been studied [151, 152, 154]. A Gaussian wire shape has been assumed, namely

$$R(z) = R_0 \left[1 + \beta \exp\left(-\frac{2z^2}{\Delta z^2} \right) \right], \tag{3.12}$$

where, as seen previously, R_0 is the radius of the undeformed part of the wire and the deformation region extends for Δz along the z axis around the point $z = 0$ with a maximum deformation βR_0 with respect to the undeformed wire (see Fig. 3.3).

In order to explain the absorption and emission spectra usually observed in porous silicon, the effective single-particle Schrödinger equation, which comes out from the variational procedure depicted in subsec. 3.1.2 has been preliminarily solved. Hard wall boundary conditions have been used. The numerical solution of this equation has been performed by a mid point shooting method (see references in appendix B). Under suitable conditions on the wire bulge, localized states within the bulge itself appear, which lie just below the mini-band corresponding to quantum states delocalized over all the wire. The geometrical parameters affect both the position of the confined energy level with respect to the mini-band edge and the number of such states (excited confined levels can also come out). This is shown in Fig. 3.6, where the localized ground and first excited states energies are shown for different geometries. It comes out that not any deformation is able to bind a particle within the bulge. In particular, the smoother the geometry, the less localized the particle. This is confirmed by considering that the extension along the z direction of these localized states increases if smoother and smoother geometries are considered. This is shown in Fig. 3.7 where the wave function square modulus calculated for different geometries is plotted. Actually, let

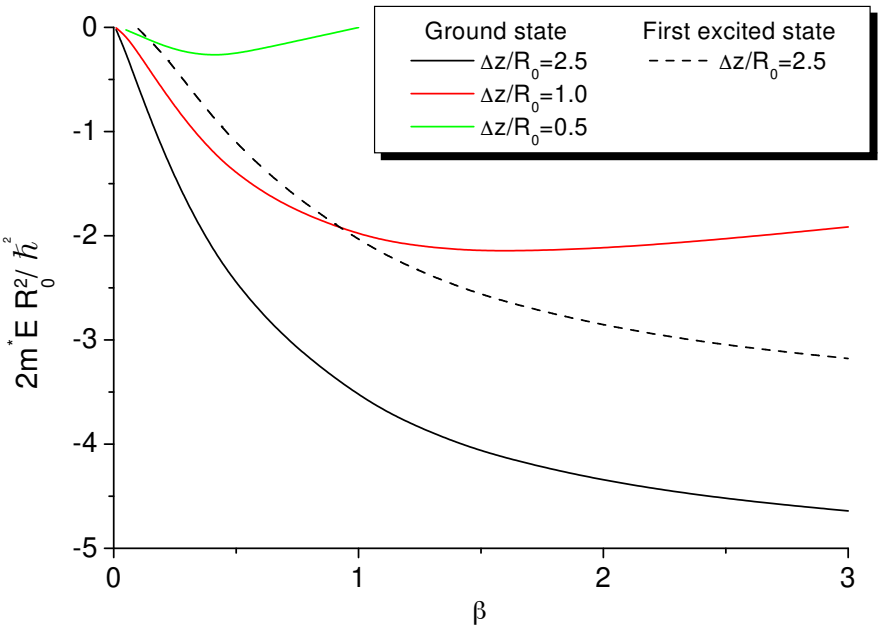

Figure 3.6: The ground-state energy for quantum states localized within the bulge of Fig. 3.3, for three different wire geometries (solid lines). Among these geometries, only the one with $\Delta z/R_0 = 2.5$ can support a localized excited state (dashed line).

us note that if very sharp geometries are considered, the confined energies tend to decrease their modulus, as if the localization became less strong (this corresponds to the presence of positive maxima in the effective potential, as shown in Fig. 3.4 and Fig. 3.5). Nevertheless, we must say that we are not interested to such geometries, because the ones involved in porous silicon structures, as we are going to see, have aspect ratios ranging from nearly 0 to 0.5. However, the decreasing of the wave function localization for very sharp geometries could be a spurious effect. In fact, it has been shown [151, 154] that the variational approach which has been presented can be improved by substituting the variational ansatz (3.7) with a more complicated wave function in the form of a series expansion. This gives rise to a system of coupled differential equations, which can be solved within a perturbative scheme. It comes out that as far as not very sharp geometries (such as those of interest

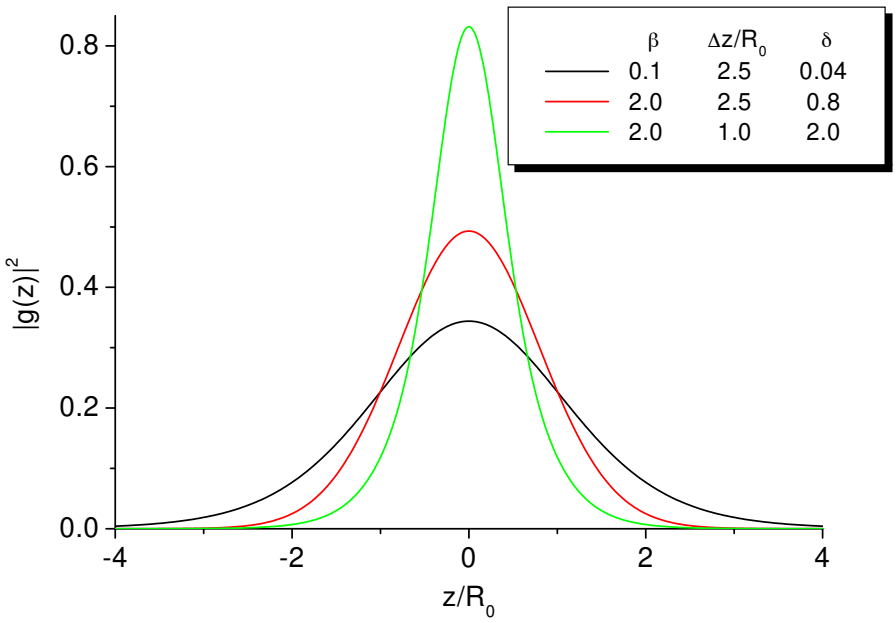

Figure 3.7: Wave function square modulus calculated for different bulge geometries. It comes out that the higher the aspect ratio, the stronger the localization within the bulge. This picture is valid provided that small aspect ratios are considered.

for porous silicon) are considered, the variational ansatz (3.7) gives a very accurate result, the higher order corrections being completely negligible. Significant corrections can instead be given for very sharp geometries, because the wave function (3.7) has been written starting from the ground-state wave function of the straight wire and, therefore, is expected to give reasonable results only for those geometries which are not very far from the undeformed one.

The main result which comes out from the calculation of the single-particle spectrum is that the presence of the deformation modifies quite significantly the properties of the wire, because it induces localized states within the bulge, completely absent in the straight wire. This acquires much more relevance if we think, as indicated previously, that the porous silicon

morphology is just that of disordered arrays of deformed quantum wires. The large Stokes shift usually observed, namely the fact that the absorption and emission processes occur at different energies, can be explained just by assuming the existence of localized states as the cooperative effects of quantum confinement within a wire-like structure, which gives rise to a mini-band structure (as for the straight wire) and shape effects, which give rise to localized states whose energies lie below the mini-band edges. Because each mini-band is characterized by a large density of states, absorption processes occur between delocalized states, followed by a relaxation towards localized states. Finally, light emission between localized states occurs. By considering this widely accepted absorption/emission path, porous silicon optical absorption and emission spectra have been studied. It must be stressed that the theory contains four free parameters, namely the wire length L, R_0, β and Δz, which must be set[5]. The calculated energies obviously depend on the wire length L. For an undulating wire composed of many and different bulges, a clear separation between localized and delocalized (mini-band) states is possible only when the average distance L between bulges is greater that Δz. When this condition is satisfied, different bulges are independent from each other. The calculations have been performed for a single bulge considered as an average nanostructure in a wire of length L. The bulge extension Δz has been chosen to be the measured average nanostructure dimension. Moreover, R_0 has been calculated in such a way to obtain the observed absorption energies (let us remember that the light absorption occurs between mini-band edges, whose position is fixed by the undeformed wire radius R_0, provided that $L >> \Delta z$). Having fixed Δz and R_0, the aspect ratio δ (and, therefore, β) has been adjusted in such a way to reproduce the measured photoluminescence peak. The wire length L has been increased up to a value beyond which the calculated eigenvalues are independent from L, simulating in this way the decoupling between bulges. The application of this procedure requires, for a given sample, the measurement of the average nanostructure dimension, the

[5]Let us note that the numerical solution of the Schrödinger-like equation obtained by the variational approach previously presented must be done on a finite structure of length L. The results which are going to be shown have been obtained by assuming the wave function zero at the wire extrema ($z = \pm L/2$).

optical band-gap and the photoluminescence peak energy. The comparison with the experimental data allows to fit the porous silicon absorption and emission energies, which sets the four parameters discussed above. It comes out that the experimental data can be reproduced if the following relations among the geometrical parameters hold [151]:

$$R_0(\text{Å}) = 5.704 + 0.307\ \Delta z(\text{Å}) \tag{3.13a}$$

$$\delta = \frac{\beta R_0}{\Delta z} = 0.497 - 0.010\ \Delta z(\text{Å}) \tag{3.13b}$$

$$L = 260\ \text{Å} \tag{3.13c}$$

The absorption and emission energies have been calculated, as it has been said, by assuming that the particle cannot penetrate into the outer region (hard wall boundary conditions). This is physically meaningful because the barrier potential at the surface of the porous silicon is very high.

The comparison with the absorption and emission energies calculated by using eqs. (3.13) with the experimental data is shown in Fig. 3.8. The black and red curves represent transitions between localized states within the bulge (the considered geometries support more than one localized state). The green curve represents transitions between delocalized states. The Stokes shift (difference between the green curve and the black curve in figure) clearly comes out. Moreover, it can be observed that the transition between localized excited states (red curve) has energy very near to that of the first transition between delocalized states (green curve), which can play a fundamental role in the particle capture and transport. Some more details can be found in refs. [151–154].

3.2.2 The effect of an external environment

The effect of bulge localization has also implications related to the gas-surface interaction [153, 159, 160]. Let v be the confining potential barrier at the nanostructure surface. As said above, this potential will contain many contributions, one of the most important ones coming from surface dipoles. These dipoles, which are generated by the local charge transfer between the gas molecules and the surface atoms, can either increase or decrease the po-

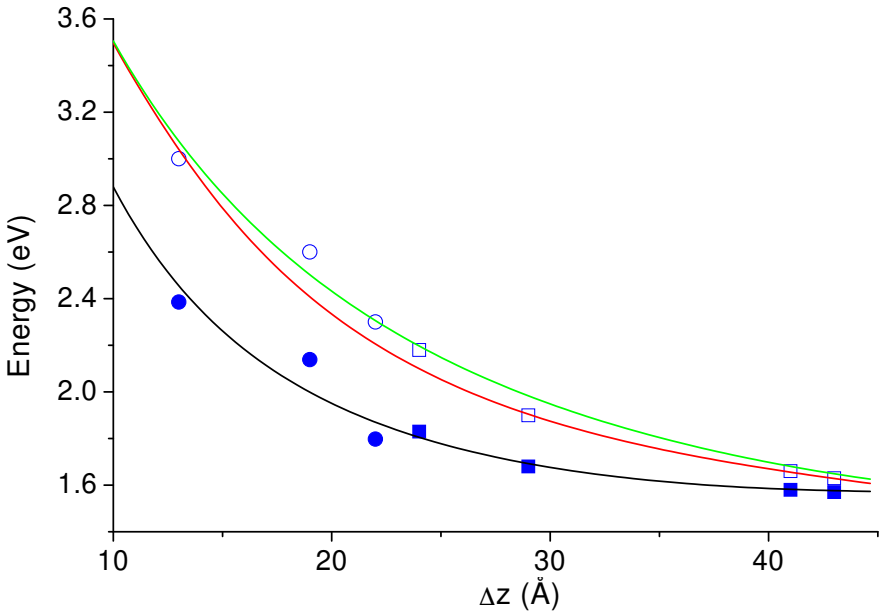

Figure 3.8: Calculated absorption and emission energies as a function of the bulge extension Δz. The black and red curves correspond to transitions between localized states within the bulge, while the green one to transitions between delocalized states. The open symbols are the experimental absorption data while the full symbols the experimental photoluminescence peaks (squares from ref. [161] and circles from ref. [162]).

tential v. The actual potential variations will therefore depend on the electronegativity differences between the surface species and the gas molecules. In Fig. 3.9 the results of the calculation for the emission energies as a function of the confining potential height v for three different geometries are shown. The barrier height has be assumed independent from z ($v = v_0$). The effect of quantum confinement consisting in an increase of the emission energies on reducing the nanostructure dimensions is very evident. Moreover, it can be observed the effect of the dimension on the curves slope variations. The smaller the dimensions, the higher the slope. This result suggests that, by taking the photoluminescence or a property related to it as a sensing signal,

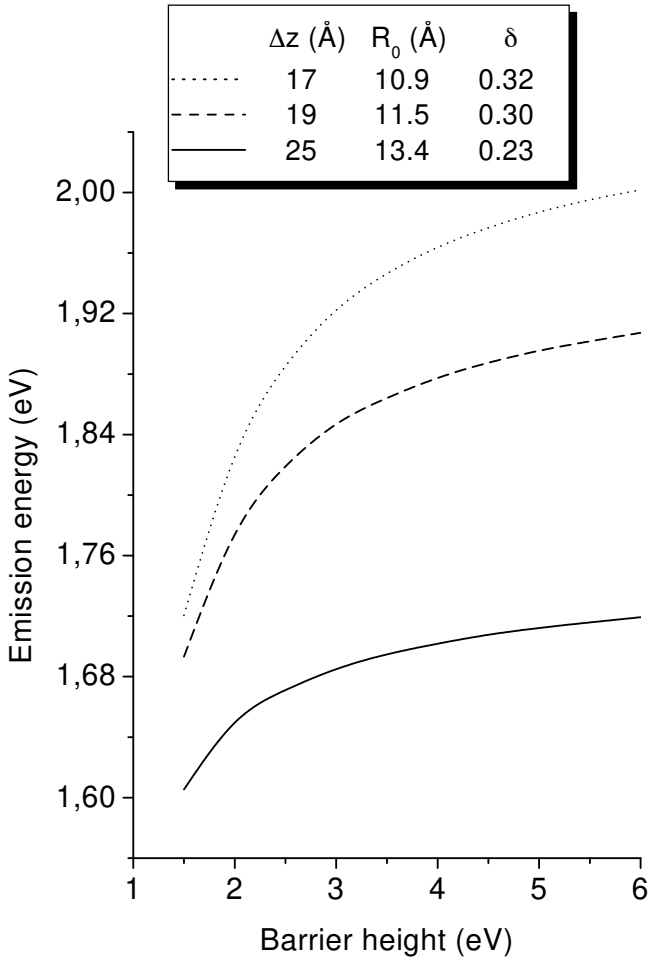

Figure 3.9: Calculated emission energies as a function of the surface barrier height for different nanostructure geometries and dimensions.

only small nanostructures may have a measurable sensitivity to the confining potential variations and therefore to the environmental changes.

Within this model, it is possible also to interpret the two main results which experimentally come out if porous silicon is put in an external oxygen environment, namely the photoluminescence red shift and quenching. At this purpose, it has been developed a specific calculation shown in Fig.

3.10, where the quantum wire has been taken of finite length L and the confining potential has been progressively reduced from 4.5 to 3.0 eV over a length $L_0 < L$ (see the inset of the figure). This progressive reduction takes into account the fact that by exposing a porous silicon sample to an oxygen atmosphere, the gas progressively covers the wire, starting from the bulge (because of the presence of localized states within it, it is expected to be the most sensitive region of the wire to an external environment). The coverage produces a reduction of the barrier height at the wire surface with respect to its value in presence of an inert atmosphere (assumed to be 4.5 eV). The figure shows both the emission and the absorption energies as a function of the coverage, defined as the ratio L_0/L. First, the photoluminescence red shift clearly comes out. It is an increasing function of the coverage. Second, it is very interesting to note that the curves corresponding to the absorption and emission energies have different slopes. In particular, the emission energy is sensitive to the barrier height variations only if the coverage length is of the order of Δz. For higher coverage lengths, it is almost constant, reflecting the fact that the emission originates from states localized within the bulge. On the contrary, the absorption energy has significant variations for any coverage length, reflecting the fact that the absorption occurs from states extending over the entire wire. Since these last states are also higher in energy, their penetration inside the surface barrier will increase with the coverage, making more efficient the electrons and holes access to surface traps and non-radiative recombination centres [163]. As a consequence, the photoluminescence quenching will increase on reducing the nanostructure average dimensions.

It is worth pointing out that other properties, such as impurity states within a deformed wire, can be studied within this model. For example it has been shown [164] that the impurity binding energy becomes larger than that of a particle localized in the bulge without the impurity and larger than that of a particle bounded to the impurity in a straight cylinder. It is possible that, even when the impurity is very far from the bulge, the wave function is localized only in the bulge region or on the impurity depending on the geometrical parameters of the wire and on the dielectric constant. This means that we can have an ionization of the impurity due to the irregularity of

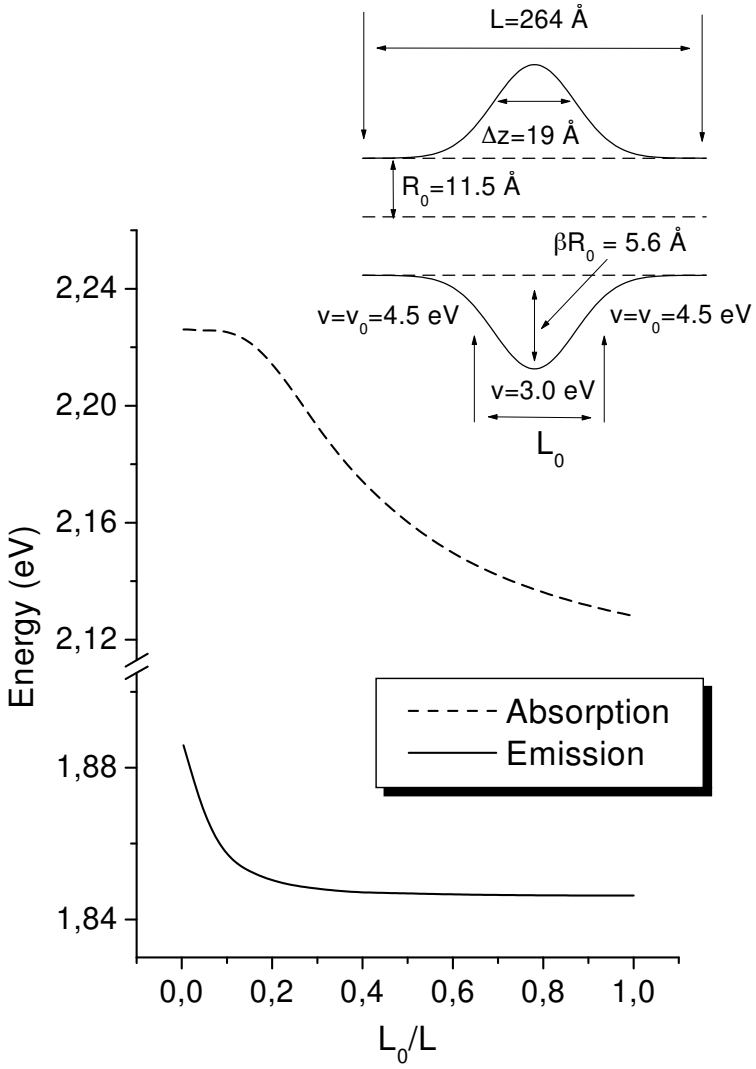

Figure 3.10: Calculated absorption and emission energies as a function of the coverage defined as the ratio L_0/L, where L and L_0 are defined in the inset. The gas coverage has been taken into account as a variation of the barrier height at the wire surface, modelled as $v(z) = v_0[1 - \sigma \exp(-2z^2/L_0^2)]$ where $v_0 = 4.5$ eV and $\sigma = 0.33$. The inset gives the details of the dimensions used.

the wire. This purely geometrical effects may have significant consequences on the charge carrier transport in these systems (particularly at very low temperatures where a Coulomb blockade may be effective) and is a possible nanostructure charging mechanism for porous silicon.

3.2.3 A check for the variational approach

It is important to stress that, by using the variational approach previously discussed, all the energies are overestimated. It is reasonable to ask how accurate is this overestimation. This is strongly related to how good the variational ansatz for the wave function (see eq. (3.7)) is. A possible way to check the approach, is to apply it to an exactly solvable geometry, so that the approximate variational results can be compared with the exact ones. For this purpose, the ground-state energy for a particle confined in an ellipsoid quantum dot has been calculated [120] (the exact calculation has been performed as shown in chapter 2).

The ellipsoid quantum dots shown in Fig. 2.1 can be studied by using spherical coordinates (r, ϑ, φ). In this coordinates system their surface has equation $r = R(\vartheta)$ where $R(\vartheta) = c/\sqrt{\chi^2 + (1-\chi^2)\cos^2\vartheta}$ represents the distance of the generic point of the ellipsoid surface from its centre. Because the ground-state trial wave function with hard wall boundary conditions $\Psi(\vec{r})$ must become $\Psi^{\mathrm{SPHERE}}_{1,0,0}(r, \vartheta, \varphi)$ (see eq. (2.19a)) in the limit $\chi \to 1$, we can set

$$\Psi_0(r, \vartheta, \varphi) = j_0\left[\frac{\pi}{R(\vartheta)} r\right] f(\vartheta). \tag{3.14}$$

In eq. (3.14) it has been considered that for the spherical quantum dot ground state we have $l = m = 0$, that the first zero of the zero-order spherical Bessel function is $z_{1,0} = \pi$ (so that the wave function (3.14) vanishes on the boundary $r = R(\vartheta)$) and that, because the problem is now invariant only for rotations around the z direction, the ground state does not depend on φ. The function $f(\vartheta)$ in eq. (3.14) takes into account the deformation effects which the ellipsoid geometry induces with respect to the completely symmetric spherical case. The function $f(\vartheta)$ has to be determined in such a way that the energy functional

$$E[f] = \frac{\left\langle \Psi_0 \left| -\frac{\hbar^2}{2m^*} \overrightarrow{\bigtriangledown}^2 \right| \Psi_0 \right\rangle}{\langle \Psi_0 \mid \Psi_0 \rangle} \tag{3.15}$$

is stationary with respect to an arbitrary variation δf of f. This, according to the variational principle, gives an upper bound to the ground-state energy. Let us note that the functional (3.15) is obtained from the more general one (3.4) with hard wall boundary conditions.

By taking the variation of eq. (3.15) with respect to f we obtain that

$$\begin{aligned} \langle \Psi_0 \mid \Psi_0 \rangle \, \delta E[f] + (\langle \Psi_0 \mid \delta\Psi_0 \rangle + \text{ c. c.}) \, E[f] = \\ \left(\left\langle \Psi_0 \left| -\frac{\hbar^2}{2m^*} \overrightarrow{\bigtriangledown}^2 \right| \delta\Psi_0 \right\rangle + \text{ c. c.} \right), \end{aligned} \tag{3.16}$$

where c. c. indicates the complex conjugate of the correspondent term in parenthesis and $\delta\Psi_0 = j_0 \left[\pi r / R(\vartheta)\right] \delta f(\vartheta)$. The stationariness of the functional (3.15) with respect to this variation of $f(\vartheta)$ is given by the condition $\delta E[f] = 0$. Moreover, because the variation $\delta f(\vartheta)$ is a function just of ϑ we can compute in eq. (3.16) the integrals over $d\varphi$ and dr. The final equation, which follows from simple algebraic manipulations and by considering that $\delta f(\vartheta)$ is arbitrary, is

$$-\frac{d}{d\vartheta}\left(\sin\vartheta \frac{df}{d\vartheta}\right) + \frac{\pi \sin\vartheta}{2\mathrm{Si}\,(2\pi)} \left[1 + \frac{\left(dR/d\vartheta\right)^2}{R^2(\vartheta)}\right] f(\vartheta) = \widetilde{\varepsilon} \, \frac{(\sin\vartheta)\, R^2(\vartheta)}{2\pi \mathrm{Si}\,(2\pi)} f(\vartheta), \tag{3.17}$$

where $\mathrm{Si}(u) = \displaystyle\int_0^u \frac{\sin\rho}{\rho} d\rho$ and $\widetilde{\varepsilon} = 2m^* E/\hbar^2$. Eq. (3.17) must be solved with the normalization condition

$$\langle \Psi_0 \mid \Psi_0 \rangle = \int_0^\pi (\sin\vartheta) \frac{R^3(\vartheta)}{\pi} f^2(\vartheta) d\vartheta = 1. \tag{3.18}$$

For $\chi \to 1$ (that is, $R(\vartheta) \to R$ constant) eq. (3.17) admits the solution $f(\vartheta) =$ constant with $\widetilde{\varepsilon} = \pi^2/c^2$, that is, the ground-state energy for the sphere, as expected. Finally, eq. (3.17) contains a term with the first derivative of $f(\vartheta)$ which can be eliminated by setting $f(\vartheta) = g(\vartheta)/\sqrt{\sin\vartheta}$. This leads to

$$-\frac{d^2g}{d\vartheta^2}+\left\{\frac{\pi}{2\mathrm{Si}\,(2\pi)}\left[1+\frac{(dR/d\vartheta)^2}{R^2(\vartheta)}\right]-\frac{1}{4\sin^2\vartheta}-\frac{1}{4}\right\}g(\vartheta)=\widetilde{\varepsilon}\frac{R^2(\vartheta)}{2\pi\mathrm{Si}(2\pi)}g(\vartheta), \tag{3.19}$$

which shows that the confinement of the particle in the ellipsoid can be viewed as the motion in an effective ϑ-dependent potential. The particle in this picture behaves as if it had a position-dependent effective mass $\widetilde{m}(\vartheta) = m^*R^2(\vartheta)/2\pi\, Si(2\pi)c^2$.

The analogy with the deformed quantum wire described in subsec. 3.1.2 is clear. The starting point is a geometry where the Schrödinger equation together with the boundary condition associated to it is separable. For this geometry the complete set of eigenfunctions and their relative eigenvalues are known. In this case we start from a spherical quantum dot, in the previous one from a cylindrical quantum wire. Then, the variational trial wave function is chosen as the starting geometry ground state where the constant radius (of the sphere or the cylinder in the two cases) is replaced with a position-dependent radius which describes the surface of the deformed nanostructure. This quantum state contains an unknown function which must take into account the effects related to the deformation. By substituting the trial wave function in the energy functional an effective single-particle Schrödinger equation is obtained, where the deformation acts as an effective potential, which depends on the position-dependent radius and its first derivative. An effective position-dependent mass can appear or not, depending on the considered geometry.

In Fig. 3.11 it is shown the comparison between the ground-state energy (as a function of χ) calculated with the exact method (black line) with the one calculated using the variational approach (red line) described above. As we can see, the results are in very good accordance provided we do not consider geometries with χ very far from 1. Anyway, as expected, the variational solution always gives an upper bound to the exact one. Moreover, the variational approach gives a very accurate estimation of the ground-state energy, provided that the considered geometry does not have very large deviations from the starting one.

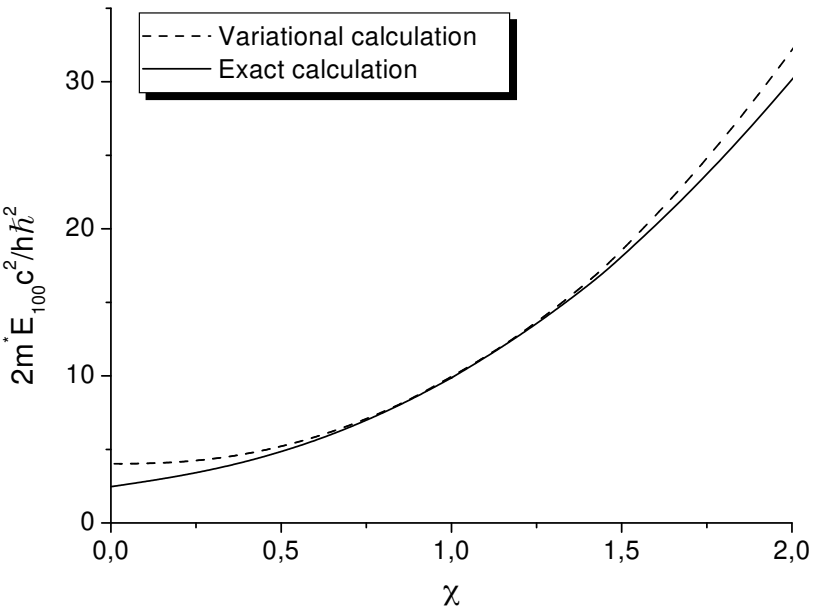

Figure 3.11: Ground-state energy for a particle confined in an ellipsoid quantum dot as calculated with the exact approach (black line) and the variational one (red line).

Chapter 4

Topological surface states

In chapters 2 and 3 it has been shown that the physical properties of a nanostructure are strongly related, besides to the system dimensionality and dimensions, to its shape. The properties of an ellipsoid quantum dot are very different from those of a spherical quantum dot, as well as the presence of a bulge in a cylindrical quantum wire can give rise to localized states completely absent in a perfectly cylindrical structure. The main result is that it is not possible to have out of consideration the system geometry, if the material properties at the nanometric scale must be studied.

So far, only the properties related to bulk quantum states have been investigated. On the other hand, it is known that the electrical and optical properties of a given material are determined by the presence of surface states as well [165]. The study of surface defects is very important from both the physical and technological point of view. In fact, despite the fabrication techniques have reached an high degree of precision, the presence of structural defects cannot be avoided at all. Therefore, in presence for example of interfaces such as Si/SiO_2, quantum states localized on the surface appear, due to a missing atom, to the presence of an impurity, and so on. This constitutes a technological limit to the device performances because the carriers can be trapped in quantum states localized on the interface. While the structural defects, which are extended over distances of few lattice constants, are widely studied [165], there are not many studies about defects which are extended over many lattice constants. This last ones will be referred to in the

following as *topological*, because they are related to the surface geometry. A typical problem can be that of studying a deformed plane interface (thinking, for example, to an Si/SiO_2 interface in which the separation between Si and SiO_2 is not perfectly plane but characterized by Si *bulges* into the SiO_2 layer and/or vice-versa) or, more in general, a nanostructure whose lateral surface is deformed in such a way that its curvature depends on the position. We can ask if a purely geometrical effect can be brought out if surface states are concerned. The answer to this question is the topic of this chapter.

The quantum states of a particle constrained to move in a thin region around a two-dimensional surface embedded in the three-dimensional space can be studied by assuming that the constraint to the surface is given by an attractive potential sufficiently strong to confine the particle into the surface neighbourhood. From the mathematical point of view this problem has been studied [166, 167] by using concepts of differential geometry. The results indicate that, depending on the mean and Gauss surface curvature, the kinetic energy operator gives rise to an extra topological potential acting as a confinement source for the motion along the surface. Since such a potential is only due to the surface curvature, its action is independent from both the particle charge and mass.

This purely mathematical problem gains a strong physical meaning if we consider nanostructured systems such as quantum wires and dots. In many of these systems there is a surface, generally closed, whose reconstruction and interaction with the external environment produces a potential, located near the surface, able to bind particles along the surface normal. Moreover, when a nanostructure is exposed to an oxidizing or reducing gas, a distribution of surface dielectric dipoles can be induced whose overall effect may be that of giving a potential pushing the particle towards the surface [168]. An example, in this respect, is given by light-emitting porous semiconductors such as silicon [140] (discussed in chapter 3) and gallium arsenide [169], whose porosity is obtained by an electro-chemical etching. The resulting nanostructures, either quantum dots or wires or even a combination of the two depending on the preparation process, have surfaces with a geometry highly irregular with a complex chemistry, which induces the formation of dangling bonds and partially ionic bonds [170]. Another instance is surely that of an accumula-

tion layer, in particular that corresponding to the steepest band slope with an extension of few nanometres. Such type of layer may be found in both the two-dimensional systems [171] and nanostructures [145]. Unfortunately, even if some physical hints can be given to understand that the existence of that potential is not just a mathematical trick, it is a very difficult task to construct it because of the large number of parameters and effects which should be taken into account. At this stage it is not possible to be more than speculative on this potential because its precise assessment would require more experimental information on the nanostructured surface chemistry.

The interest here is to search for those geometries responsible for the particle localization on these nanostructure surfaces and discuss the implications for both the optical and transport properties. It is expected, in fact, that the surface trapping of electrons and/or holes could both open new channels for optical emission and/or absorption and modify the electrical conductivity of the material. Moreover, in view of the possible applications of porous silicon layers as the active material in a sensor device [141, 156], the presence of these states is of particular relevance for the surface reactivity towards a gas environment. It will be found, within the effective-mass approximation, that, depending on the surface curvature, a particle can have different probabilities of being in different points of the surface [172–174]. This fact is described through a topological effective potential which tends to localize the particle mainly into those surface regions with maximum curvature. It must be stressed that these are a new type of surface states whose origin is linked to the surface topology rather than to either the breaking of the lattice periodicity or surface defects.

In sec. 4.1 the concept of topological surface state is introduced, showing the coordinate system suitable for studying such states as well as the surface differential geometry quantities needed in such a study. Next, the derived equations are applied to three different surface geometries (a deformed quantum wire, a deformed plane and an ellipsoid quantum dot), to show how the existence of surface confined states of topological nature can arise in very different systems. The main numerical results are presented and discussed (secs. 4.2, 4.3 and 4.4).

4.1 Topological surface states

In this section the main concepts of differential geometry on which the research on topological surface states is based are recalled. The original work by da Costa [166] is followed.

Given the surface S with parametric equation $\vec{r} = \vec{r}(q_1, q_2)$, a point $\vec{R}$ in the space can be determined through the relation

$$\vec{R} = \vec{r}(q_1, q_2) + q_3 \hat{N}(q_1, q_2) \tag{4.1}$$

where $\hat{N}(q_1, q_2)$ is the versor of the normal to S in the point with coordinates (q_1, q_2) and q_3 is the algebraic distance of the point from the surface. In practice, a point $P \equiv \vec{R}$ in the neighbourhood of S can be parameterized by fixing a point $Q \equiv \vec{r} \in S$ and by moving along the normal to S at that point, as shown in Fig. 4.1. It is clear that, in general, this represents just a local mapping of the space. In fact, a one-to-one correspondence cannot be obtained because the normals to S at different points cross, so that the curvilinear coordinates of $\vec{R}$ will not be univocally defined. However, for the geometries we are going to study it can be shown that a well-defined mapping of the region of interest can be established.

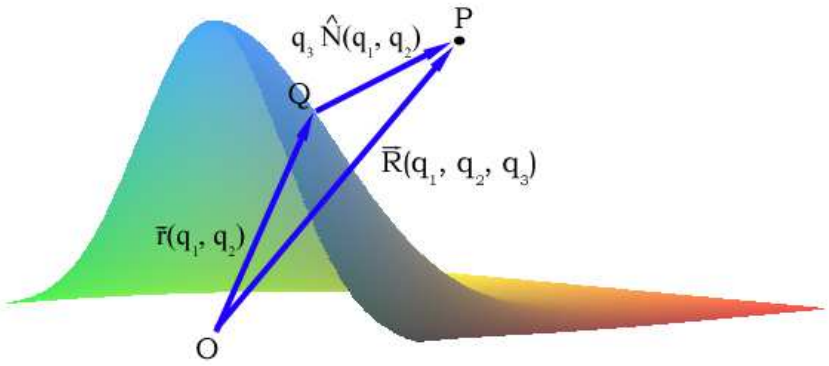

Figure 4.1: The three-dimensional curvilinear coordinates chosen to parameterize the neighbourhood of a surface S. q_1, q_2 are the curvilinear coordinates of a point $Q \equiv \vec{r} \in S$. The generic point $P \equiv \vec{R}$ can be identified by moving along the normal to S at Q.

From standard surface differential geometry it is known that the square distance between two points on S is given by the first differential form by Gauss [175], that is,

$$ds^2 = \sum_{i,j=1}^{2} g_{ij} dq_i dq_j \tag{4.2}$$

where g_{ij} are the components of the metric tensor, defined as follows:

$$\mathbf{g} = \left\| \frac{\partial \vec{r}}{\partial q_i} \cdot \frac{\partial \vec{r}}{\partial q_j} \right\|. \tag{4.3}$$

The area of the surface element is

$$dS = \sqrt{\det \mathbf{g}}\, dq_1 dq_2, \tag{4.4}$$

with

$$\det \mathbf{g} = \left| \frac{\partial \vec{r}}{\partial q_1} \times \frac{\partial \vec{r}}{\partial q_2} \right|^2. \tag{4.5}$$

The normal versor to S at a given point $\vec{r} \equiv (q_1, q_2)$ is given by

$$\hat{N}(q_1, q_2) = \frac{1}{\sqrt{\det \mathbf{g}}} \left(\frac{\partial \vec{r}}{\partial q_1} \times \frac{\partial \vec{r}}{\partial q_2} \right). \tag{4.6}$$

The scalar product between an elementary displacement $d\vec{r}$ on the surface and the correspondent variation $d\hat{N}$ of the versor $\hat{N}$ changed of sign is given by the second differential form by Gauss [175]:

$$-d\vec{r} \cdot d\hat{N} = \sum_{i,j=1}^{2} h_{ij} dq_i dq_j, \tag{4.7}$$

where h_{ij} are the components of the tensor

$$\mathbf{h} = \|h_{ij}\| = \left\| \hat{N} \cdot \frac{\partial^2 \vec{r}}{\partial q_i \partial q_j} \right\|. \tag{4.8}$$

It is easy to show, starting from eq. (4.6), that the derivatives of the versor $\hat{N}(q_1, q_2)$ lie in the tangent plane, so that they can be written as

$$\frac{\partial \hat{N}}{\partial q_i} = \sum_{j=1}^{2} \alpha_{ij} \frac{\partial \vec{r}}{\partial q_j}, \quad i = 1, 2 \tag{4.9}$$

where it has been introduced the matrix

$$\boldsymbol{\alpha} = \left\|\alpha_{ij}\right\| = \frac{1}{\det \mathbf{g}} \begin{Vmatrix} g_{12}h_{21} - g_{22}h_{11} & g_{21}h_{11} - g_{11}h_{21} \\ g_{12}h_{22} - g_{22}h_{12} & g_{12}h_{21} - g_{11}h_{22} \end{Vmatrix}. \tag{4.10}$$

In the considered three-dimensional neighbourhood of S the metric tensor is given by

$$\mathbf{G} = \left\|G_{ij}\right\| = \left\|\frac{\partial \vec{R}}{\partial q_i} \cdot \frac{\partial \vec{R}}{\partial q_j}\right\| \quad i,j = 1,2,3. \tag{4.11}$$

The explicit expressions of the G_{ij}'s are

$$G_{ij} = g_{ij} + q_3 \left[\boldsymbol{\alpha}\mathbf{g} + (\boldsymbol{\alpha}\mathbf{g})^T\right]_{ij} + q_3^2 \left[\boldsymbol{\alpha}\mathbf{g}\boldsymbol{\alpha}^T\right]_{ij} \qquad \text{with } i,j = 1,2. \tag{4.12}$$

Here the superscript "T" indicates the transposed matrix. Moreover, since the variable q_3 has been chosen as normal to the surface tangent plane, the other components of $\mathbf{G}$ are

$$\begin{array}{l} G_{i3} = G_{3i} = 0 \quad \text{with } i = 1,2 \\ G_{33} = 1 \end{array}. \tag{4.13}$$

This shows that, independently from the considered surface S, the coordinate system which has been chosen is orthogonal.

It is possible now to write the Laplacian operator using the curvilinear coordinates (q_1, q_2, q_3) [123] and to obtain the following time-independent effective-mass[1] Schrödinger equation:

$$-\frac{\hbar^2}{2m^*} \sum_{i,j=1}^{3} \frac{1}{\sqrt{\det \mathbf{G}}} \frac{\partial}{\partial q_i} \left(\sqrt{\det \mathbf{G}}\, \bar{G}_{ij} \frac{\partial \psi}{\partial q_j}\right) + V(q_3)\psi = E\psi, \tag{4.14}$$

where $\bar{G}_{ij}$ is the ratio between the algebraic complement of the element G_{ij} and $\det \mathbf{G}$ and $V(q_3)$ is the confining potential in the direction normal to the

[1] See appendix A about the effective-mass approximation. It must be stressed that since the followed approach is not an atomistic one, the validity of the results which are going to be discussed is limited to those deformations whose extension comprises several atomic distances. With this restrictions, a bulk effective mass can be used in eq. (4.14).

surface[2]. By using eq. (4.13), eq. (4.14) can be rewritten as

$$-\frac{\hbar^2}{2m^*}\sum_{i,j=1}^{2}\frac{1}{\sqrt{\det\mathbf{G}}}\frac{\partial}{\partial q_i}\left(\sqrt{\det\mathbf{G}}\,\bar{G}_{ij}\frac{\partial\psi}{\partial q_j}\right)-\frac{\hbar^2}{2m^*}\left[\frac{\partial^2\psi}{\partial q_3^2}+\frac{\partial}{\partial q_3}\left(\ln\sqrt{\det\mathbf{G}}\right)\frac{\partial\psi}{\partial q_3}\right]+V(q_3)\psi=E\psi. \tag{4.15}$$

By using eq. (4.12), the volume element dV is given by

$$dV=\sqrt{\det\mathbf{G}}\;dq_1dq_2dq_3=\sqrt{\det\mathbf{g}}\left[1+(\mathrm{tr}\boldsymbol{\alpha})q_3+(\det\boldsymbol{\alpha})q_3^2\right]dq_1dq_2dq_3=H\,dSdq_3 \tag{4.16}$$

with $H=1+(\mathrm{tr}\boldsymbol{\alpha})q_3+(\det\boldsymbol{\alpha})q_3^2$. By defining

$$\psi(q_1,q_2,q_3)=\frac{\chi(q_1,q_2,q_3)}{\sqrt{H(q_1,q_2,q_3)}} \tag{4.17}$$

and inserting eq. (4.17) in eq. (4.15), the following equation for χ is obtained:

$$-\frac{\sqrt{H}}{\sqrt{\det\mathbf{G}}}\sum_{i,j=1}^{2}\frac{\partial}{\partial q_i}\left[\sqrt{\det\mathbf{G}}\bar{G}_{ij}\frac{\partial}{\partial q_j}\left(\frac{\chi}{\sqrt{H}}\right)\right]-\frac{\partial^2\chi}{\partial q_3^2}-\frac{1}{4H^2}\left(H_1^2-2HH_2\right)\chi+\widetilde{V}(q_3)\chi=\widetilde{\varepsilon}\chi, \tag{4.18}$$

with $\widetilde{\varepsilon}=2m^*E/\hbar^2$, $\widetilde{V}(q_3)=2m^*V(q_3)/\hbar^2$, $H_1=\dfrac{\partial H}{\partial q_3}$, $H_2=\dfrac{\partial^2 H}{\partial q_3^2}$. Upon assuming that the potential $V(q_3)$ is attractive and different from zero in a thin sheet around the surface (that is, the particle is confined in the direction normal to it), the limit $q_3\to 0$ can be carried out. In this limit it can be easily shown that eq. (4.18) can be solved by the separation of variables technique. This means that the wave function χ can be written as

$$\chi(q_1,q_2,q_3)=\sigma(q_1,q_2)p(q_3) \tag{4.19}$$

[2]The fact that the confining potential depends just on q_3 is an hypothesis done to simplify the problem.

with the function $p(q_3)$ solution of the one-dimensional Schrödinger equation

$$-\frac{\partial^2 p}{\partial q_3^2} + \widetilde{V}(q_3)p = \widetilde{\varepsilon}_n p \tag{4.20}$$

and $\sigma(q_1, q_2)$ solution of the following two-dimensional Schrödinger equation

$$-\frac{1}{\sqrt{\det \mathbf{g}}} \sum_{i,j=1}^{2} \frac{\partial}{\partial q_i} \left(\sqrt{\det \mathbf{g}}\, \bar{g}_{ij} \frac{\partial \sigma}{\partial q_j} \right) - \left(\frac{T^2}{4} - D \right) \sigma = (\widetilde{\varepsilon} - \widetilde{\varepsilon}_n)\, \sigma \tag{4.21}$$

where $T = \operatorname{tr} \boldsymbol{\alpha}$ and $D = \det \boldsymbol{\alpha}$. Here $\bar{g}_{ij}$ is the ratio between the algebraic complement of the element g_{ij} and $\det \mathbf{g}$. Eq. (4.21) can be written as

$$\left[-\overrightarrow{\nabla}^2_{q_1,q_2} + \widetilde{V}_T(q_1, q_2) \right] \sigma(q_1, q_2) = (\widetilde{\varepsilon} - \widetilde{\varepsilon}_n)\sigma(q_1, q_2), \tag{4.22}$$

where $\overrightarrow{\nabla}^2_{q_1,q_2} = \dfrac{\partial^2}{\partial q_1^2} + \dfrac{\partial^2}{\partial q_2^2}$ is the Laplacian operator in the (q_1, q_2) plane while $\widetilde{V}_T(q_1, q_2) = -\left(\dfrac{T^2}{4} - D \right)$ is a *topological potential* in the sense that it depends on the metric and curvature properties of the surface [172]. In fact, it can be easily shown that $T = -2M$ and $D = G$ where M and G are respectively the mean and Gauss curvature of the surface[3]. Eq. (4.21) has been derived also in refs. [166] and [167]. Collecting all these formulas, the probability of finding the particle in volume element dV reads

$$dP = |\psi(q_1, q_2, q_3)|^2\, dV = |\sigma(q_1, q_2)|^2\, |p(q_3)|^2\, dS dq_3. \tag{4.23}$$

[3]Let us recall [175] that, at each point of a regular surface S, the curvature radius varies over a continuous set of values but always assumes a maximum and a minimum value $R_{\max}$ and $R_{\min}$. In correspondence, there are a minimum and a maximum value of the curvature, $R_{\max}^{-1}$ and $R_{\min}^{-1}$ respectively. The surface mean curvature at the given point is defined as $M = \dfrac{1}{2}\left(\dfrac{1}{R_{\min}} + \dfrac{1}{R_{\max}} \right)$ while the Gauss curvature as $G = \dfrac{1}{R_{\min} R_{\max}}$, so that $\widetilde{V}_T(q_1, q_2) = -\dfrac{1}{4}\left(\dfrac{1}{R_{\min}} - \dfrac{1}{R_{\max}} \right)^2$. This shows that this potential has its minimum in the points where the maximum and minimum curvature have their maximum difference, and is zero for the plane and spherical geometries, for which $R_{\min} = R_{\max}$ at each point.

Since $\int |p(q_3)|^2 \, dq_3 = 1$, the quantity $|\sigma(q_1, q_2)|^2 \, dS$ gives then the probability of finding the particle on the surface element dS for arbitrary values of the coordinate q_3.

Let us stress that, provided that the coordinates system be well defined (which depends on the particular considered surface) and the existence of a potential which confines the particle in the neighbourhood of the surface be assumed, the mathematical calculations up to eq. (4.18) are exact. The actual approximation is in performing the limit $q_3 \to 0$ in eq. (4.18) and separating, in this way, its solution as shown in eq. (4.19) (this corresponds to the decoupling of the motion along the surface S from the motion along the direction normal to it). It is worth pointing out other two important points [172–174]. First, the equation for the surface wave function contains the topological potential (as indicated previously) which, as we are going to see, is able to confine the particle in the points of the surface where the maximum and minimum curvature have their maximum difference. This property is related just to the surface geometry and in this sense we can speak about a new class of surface states. Second, it could be look as if by deriving eq. (4.21) from eq. (4.18) we had switched from a three-dimensional system to a two-dimensional one. This is actually wrong and, perhaps, it is just this point the most interesting feature of topological surface states. If we had started from a two-dimensional surface, eq. (4.22) would not have contained the topological potential but just the two-dimensional Laplacian operator, describing in this way a free particle in two dimensions[4]. This becomes even clearer if we think that by performing the limit as $q_3 \to 0$ in eq. (4.18) after performing the transformation (4.19), the topological potential comes out

[4]Let us note that the two-dimensional Hamiltonian would depend in this case just on the surface metric properties (namely, on the g_{ij}'s and their derivatives). This means that the two-dimensional motion on two isometric surfaces (for which correspondent points can be found with the same g_{ij}'s) would be the same. Because the surface mean curvature is not in general the same for isometric surfaces (which is instead true for the Gaussian curvature), eq. (4.21) must somehow "remember" the three-dimensional nature of the problem. This is a very important conceptual point which has been stressed also in refs. [176] (with a great mathematical detail), [177] and, from the point of view of the quantum field theory, in ref. [178].

from the Hamiltonian part containing the derivatives of ψ with respect to q_3, reflecting the fact that its origin is related to the three-dimensional nature of the problem.

However, we are obviously considering a first-order approximation (namely, the limit $q_3 \to 0$), but this is enough to focus the main point, that is, a curvature-dependent localization.

4.2 Surface states on a deformed quantum wire

4.2.1 Theory

Let us consider the deformed quantum wire as in Fig. 3.3. As shown in chapter 3, this surface can be represented by the parametric equation (3.6)

$$\begin{cases} x = R(u)\cos\varphi \\ y = R(u)\sin\varphi \\ z = u \end{cases}$$

with, as in eq. (3.12),

$$R(u) = R_0\left[1 + \beta\exp\left(-\frac{2u^2}{\Delta z^2}\right)\right],$$

$0 \leq \varphi < 2\pi$ and $-\infty < u < +\infty$. It is worth recalling that the parameters of the surface are: R_0 (the radius of the undeformed part of the wire), β (βR_0 determines the extension of a wire bulge ($\beta > 0$) or that of a wire constriction ($\beta < 0$)) and Δz, which gives the extension of the deformed part along the z direction.

In chapter 3 it was shown that if the wave function decays exponentially outside the confining volume, localized states with energy in the mini-band gap of the confined semiconductor can appear. Their wave functions are localized along the z direction with the maximum on the bulge. Moreover, the conduction and valence mini-band edges are raised or lowered on reducing or increasing R_0 without a significant dependence on the other geometrical

parameters. The coexistence of these localized states together with extended states has allowed a possible explanation of the long-standing problem related to the large difference between the absorption and the emission energies found in porous silicon. The photoluminescence quenching and red shift [179] in the presence of oxygen have been described within the same model.

Now, the same structural model (see Fig. 3.3) together with equations of sec. 4.1 is used to study the existence of topological surface states in confined systems with a view, in particular, to the case of porous silicon.

For the surface given by eqs. (3.6) and (3.12), the matrixes $\mathbf{g}$, $\mathbf{h}$ and $\boldsymbol{\alpha}$ defined respectively in eqs. (4.3), (4.8) and (4.10) are:

$$\mathbf{g} = \begin{Vmatrix} \dfrac{1}{\mathcal{F}^2(u)} & 0 \\ 0 & R^2(u) \end{Vmatrix}, \tag{4.24a}$$

$$\mathbf{h} = \mathcal{F}(u) \begin{Vmatrix} -\dfrac{d^2R}{du^2} & 0 \\ 0 & R(u) \end{Vmatrix} \tag{4.24b}$$

and

$$\boldsymbol{\alpha} = \mathcal{F}(u) \begin{Vmatrix} \mathcal{F}^2(u)\dfrac{d^2R}{du^2} & 0 \\ 0 & -\dfrac{1}{R(u)} \end{Vmatrix}, \tag{4.24c}$$

with

$$\mathcal{F}(u) = \left[1 + \left(\frac{dR}{du}\right)^2\right]^{-\frac{1}{2}}. \tag{4.25}$$

The two-dimensional differential equation (4.21) applied to this case has terms with the second derivative with respect to φ and u and a term with the first derivative with respect to u. This last term can be eliminated by performing the substitution

$$\sigma(u,\varphi) = \frac{t(u)}{\sqrt{R\mathcal{F}}}\frac{\exp(im\varphi)}{\sqrt{2\pi}} \tag{4.26}$$

where it has been taken into account the fact that, because of the rotational symmetry of the surface (see Fig. 3.3), the angular part of the wave function is $\exp(im\varphi)/\sqrt{2\pi}$ with $m = 0, \pm 1, \pm 2, \ldots$ and $m\hbar$ the angular momentum of the particle along the z axis. The Schrödinger equation for $t(u)$ now reads

$$-\mathcal{F}^2 \frac{d^2t}{du^2} + \left[-\mathcal{F}^2\left(\frac{d\Gamma}{du} - \Gamma^2\right) - \frac{T^2}{4} + D + \frac{m^2}{R^2}\right] t(u) = (\widetilde{\varepsilon} - \widetilde{\varepsilon}_n)\, t(u), \quad (4.27)$$

with $\Gamma = -\dfrac{1}{2R\mathcal{F}} \dfrac{d\,(R\mathcal{F})}{du}$. It is interesting to observe that in this one-dimensional Schrödinger equation the particle behaves as it had a position dependent effective mass $\mathcal{F}^{-2} > 1$ in a topological potential given by

$$v(u) = -\mathcal{F}^2\left(\frac{d\Gamma}{du} - \Gamma^2\right) - \frac{T^2}{4} + D + \frac{m^2}{R^2}. \quad (4.28)$$

Since

$$\frac{d\,(R\mathcal{F})}{du} = -RT\frac{dR}{du} \quad (4.29)$$

the topological potential (4.28) depends on the curvatures and on the derivative of the average curvature of S and has the asymptotic behaviour

$$\lim_{u\to\pm\infty} v(u) = \frac{1}{R_0^2}\left(m^2 - \frac{1}{4}\right), \quad (4.30)$$

so that the effective potential defined as

$$v_{\text{eff}}(u) = v(u) - \frac{1}{R_0^2}\left(m^2 - \frac{1}{4}\right) \quad (4.31)$$

is zero asymptotically. It is easy to see that $v_{\text{eff}}(u)R_0^2$ and $\mathcal{F}(u)$ are adimesional quantities satisfying the scaling rules

$$v_{\text{eff}}(u)R_0^2 = \mathcal{V}\left(\beta, \frac{R_0^2}{\Delta z^2}, \frac{u}{R_0}\right), \quad (4.32a)$$

$$\frac{1}{\mathcal{F}^2(u)} = \mathcal{M}\left(\beta, \frac{R_0^2}{\Delta z^2}, \frac{u}{R_0}\right). \quad (4.32b)$$

With the introduction of the adimensional variables $w = u/R_0$ and $\zeta = R_0^2/\Delta z^2$, the differential equation (4.27) becomes [172] (the symbol $t(w)$ will be used instead of $t(wR_0)$)

$$-\frac{1}{\mathcal{M}(\beta,\zeta,w)}\frac{d^2t}{dw^2} + \mathcal{V}(\beta,\zeta,w)t(w) = \gamma\ t(w) \tag{4.33}$$

with

$$\gamma = \left[\widetilde{\varepsilon} - \widetilde{\varepsilon}_n - \frac{1}{R_0^2}\left(m^2 - \frac{1}{4}\right)\right] R_0^2 \tag{4.34}$$

and

$$R_0\int_{-\infty}^{+\infty} dw\mathcal{M}(\beta,\zeta,w)t^2(w) = \int_S dS\sqrt{\det \mathbf{g}}\ |\sigma(u,\varphi)|^2 = 1. \tag{4.35}$$

Therefore, it is possible to find in the plane (ζ,β), with $-1 \leq \beta < +\infty$ and $0 < \zeta < +\infty$, the region in which eq. (4.33) has localized states, i.e. wave functions $t(w)$ with finite norm localized where the potential $\mathcal{V}(\beta,\zeta,w)$ is negative. This can either occur in the bulge or in a bottleneck of the deformed wire, as we are going to see in the next subsection.

Before going on a discussion of the results related to equation (4.33), it is important to give the correct energy references. Although not explicitly indicated in eq. (4.15), the energy reference is the bottom (top) of the bulk conduction (valence) band. Let us consider first, from eq. (4.33), the case in which the wire surface has no deformations, that is, $\beta = 0$ in eq. (3.12). The eigenvalues are given by

$$\widetilde{\varepsilon}_{\text{surf}} = k_z^2 + \frac{1}{R_0^2}\left(m^2 - \frac{1}{4}\right) + \widetilde{\varepsilon}_n + E_c \tag{4.36}$$

where k_z is the quasi-momentum along the surface and E_c is the bulk conduction band minimum. This equation gives the surface mini-band structure which is analogous to the quantum wire mini-band structure [151]

$$\widetilde{\varepsilon}_{\text{bulk}} = k_z^2 + \frac{Z_{n,m}^2}{R_0^2} + E_c \tag{4.37}$$

where $Z_{n,m}$ is the n-th zero of the cylindrical Bessel function $J_m(x)$ (hard wall boundary conditions). There are two interesting points in eq. (4.36). The first

is that each state is labelled by the three numbers n, m, k_z reflecting the fact that, since the beginning, a three dimensional space has been considered. The second, and perhaps the most important, is that the surface mini-band edges depend on the wire radius R_0 as the quantum wire confinement mini-bands do in equation (4.37). From eqs. (4.36) and (4.37) some conclusions can be drawn as far as the mini-band alignments ($k_z = 0$) is concerned. By assuming that the eigenvalues $\widetilde{\varepsilon}_n$ of the potential $\widetilde{V}(q_3)$ in eq. (4.20) are negative, that is, the potential $V(q_3)$ goes rapidly to zero going from the wire surface to the centre, it is seen that the surface mini-band edge with $m = 0$ lies in the gap of both the bulk and confined structures ($Z_{1,0} = 2.4048$), as sketched in Fig. 4.2. The complete surface electronic structure which comprises localized and delocalized surface states may have some of those states with energies which are resonant with the volume confined ones. The actual volume and surface electronic structure alignment would require a precise knowledge of the potential $V(q_3)$. However, the prediction that charge carriers can quickly and easily be transferred from volume to surface states (and vice-versa) may have interesting consequences for both the optical and transport properties.

4.2.2 Results

The energy spectrum of the topological surface states discussed in the last subsec. has been studied [172–174] by solving eq. (4.33) numerically with an ordinary mid-point shooting method (see the appendix B for references). All the calculated localization energies are measured from the respective mini-band edge (4.36) and in the following the corresponding adimensional value γ defined in eq. (4.34) will be used. This means that the actual value of the localization energy is given by $(\hbar^2/2m^*R_0^2)\gamma$ or, if we measure R_0 in Å and take $m^*/m_e = 0.2588$ (spherical conduction effective mass used for porous silicon, where m_e is the free electron mass), by $14.725\gamma/R_0^2$ eV.

Let us consider a bulge ($\beta > 0$) and fix $m = 0$. The calculation of the ground-state energy shows that not every geometry can support a localized state. More precisely, for any fixed value of ζ, it comes out that there exists a minimum value $\beta_{\min}$ of β such that only if $\beta > \beta_{\min}$ a localized ground state is obtained. In other words, it is possible to draw, in the plane (ζ, β), the

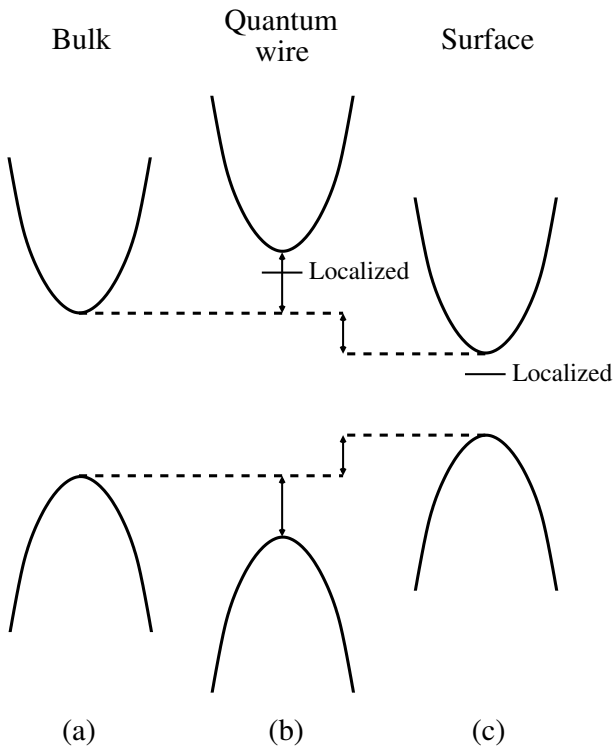

Figure 4.2: A schematic drawing showing the alignment of: (a) bulk band structure, (b) quantum wire mini-band structure and (c) surface mini-band structure. The straight lines in (b) and (c) indicate the presence of localized states, while the arrows indicate the mini-band edge shifts with respect to the bulk band edges.

curve $\beta = \beta_{\min}$ which separates the region corresponding to those geometries which support a localized ground state from the region corresponding to geometries for which a localized state does not exist. This is shown in Fig. 4.3a. It is interesting to observe that, for a given wire radius R_0, a decrease of the bulge extension Δz (corresponding to an increase of ζ) must be paired by a corresponding decrease of its minimum relative depth $\beta_{\min}$. As it has already been stressed, the phase diagram of Fig. 4.3a shows that not all geometries can support a localized surface state. Let us take, as an example, porous silicon for which the geometries compatible with the light emission

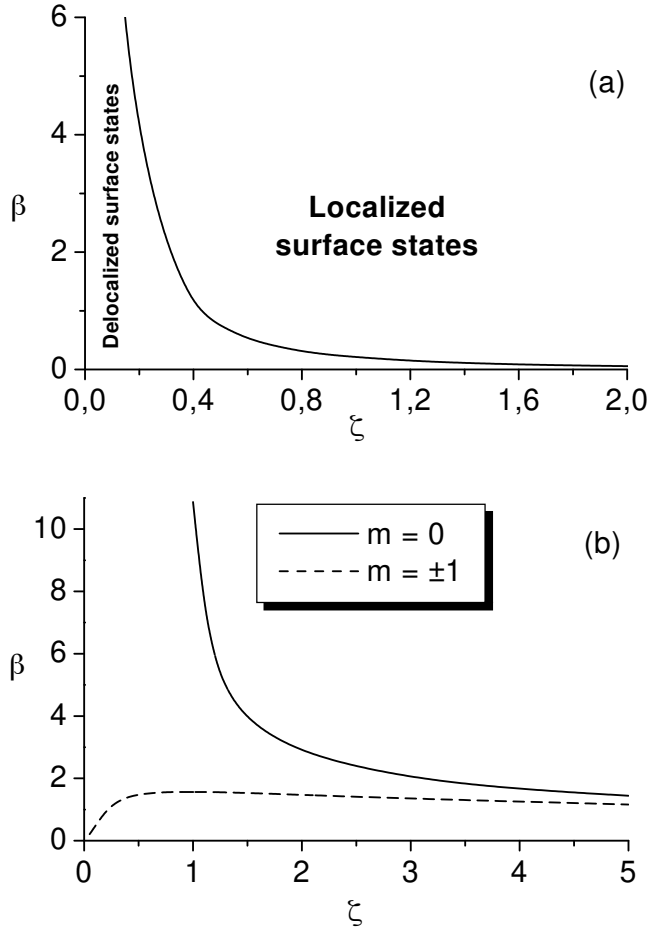

Figure 4.3: Existence diagram for: (a) the ground localized surface state for $\beta > 0$ (bulge) and $m = 0$; (b) the first excited localized surface state for $\beta > 0$ and both $m = 0$ and $m = \pm 1$. All the pairs (ζ, β) belonging to the region above the respective curves give a localized state. The first excited state with $m = \pm 1$ exists for all positive values of ζ.

have already been determined (see chapter 3 and ref. [151]). In this case the bulge dimensions are characterized by having Δz ranging from 1.0 nm to 4.5 nm, R_0 from 0.9 nm to 1.9 nm with $0.81 > \zeta > 0.18$ and $0.5 > \beta > 0.1$.

With this range of parameters it is seen from Fig. 4.3a that surface states can exist in a restricted region around $\zeta \sim 0.8$.

The calculated ground-state energies with $m = 0$ as a function of ζ and for several values of β are shown in Fig. 4.4a where it can be seen that the general trend is towards an increase of the modulus of the localization energies on increasing the overall bulge dimensions, that is, the surface curvature.

In the range $1.5 \leq \zeta \leq 5.0$ and $0.4 \leq \beta \leq 1.0$ it has been found the following interpolation formula, which reproduces numerical results of Fig. 4.4a (ground state with $m = 0$) with an error at most of 4%

$$\gamma = [a(\beta) + b(\beta)\zeta]\zeta, \tag{4.38}$$

with

$$a(\beta) = 0.01287 + 0.14874\beta - 0.17673\beta^2 + 0.16472\beta^3, \tag{4.39a}$$

$$b(\beta) = 0.0133 - 0.09564\beta - 0.15285\beta^2 - 0.12083\beta^3. \tag{4.39b}$$

The wave functions corresponding to the calculated energies are localized on the bulge centre, the point of maximum curvature, as it will be shown in a following figure. Moreover, it has been verified that if the limit $R_0 \to +\infty$ for fixed Δz and βR_0 (that is, for given bulge dimensions as Fig. 3.3 shows) is considered, the system energy decreases asymptotically towards a finite value. This reflects the fact that in the shown limit the surface becomes an open undulating plane (let us remember that a cylinder of infinite radius or, equivalently, of null curvature is a plane).

The case of a constriction ($-1 < \beta < 0$) is particularly interesting because it has been found that a localized state is formed for any value of both β and ζ. For example, the localization energies for $m = 0$ and $\beta = -0.4$ as a function of ζ have been calculated and compared with those of a bulge with $\beta = 0.4$. The results show that the modulus of the localization energies on a constriction is always bigger than the one on the corresponding bulge and the surface state always exists, even for very small values of ζ. The bulge with $\beta = 0.4$ cannot sustain a localized state when $\zeta < 1.0$.

Let us now analyze the lowest energy state with $m = \pm 1$. The calculated localization energies as a function of ζ for several values of $\beta > 0$ are shown

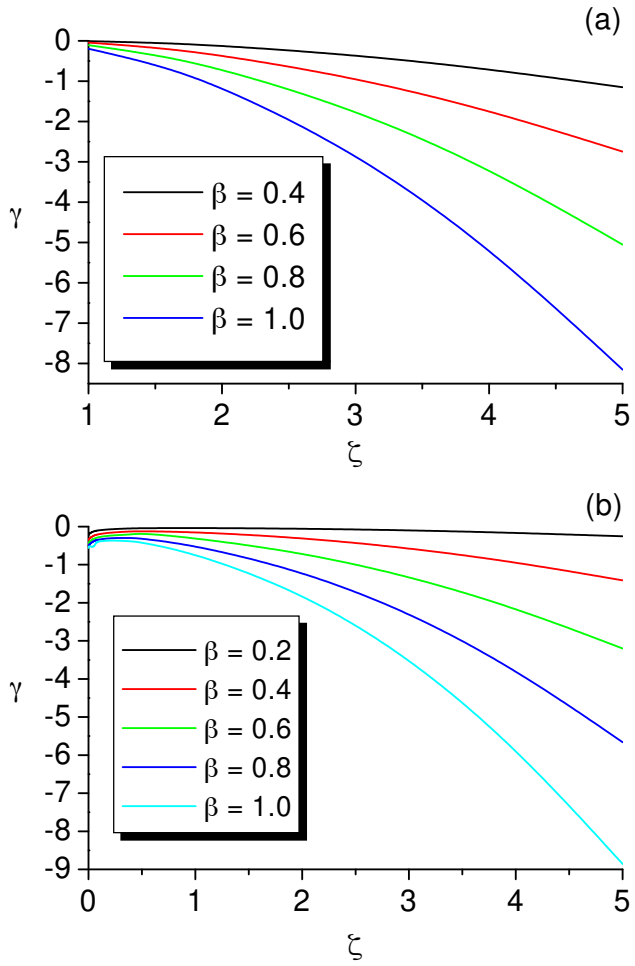

Figure 4.4: Ground-state localization energies for $m = 0$ (a) and $m = \pm 1$ (b) with $\beta > 0$ (bulge) as a function of $\zeta = R_0^2/\Delta z^2$. The energies are measured from the bottom of the respective mini-band. Surface localized states for $m = \pm 1$ are formed also for $\zeta < 1$.

in Fig. 4.4b. The are two interesting points here. The first is that a localized state is always formed, whatever are the values of the geometrical parameters β and ζ (this explains why in Fig. 4.3a an existence diagram for this state is not shown). The second is that the modulus of localization energies are larger

than those with $m = 0$, as a direct comparison with Fig. 4.4a immediately reveals. States with higher values of m, in other words, are more localized on the bulge. This result, which is apparently paradoxical if we think that $m\hbar$ represents the z component of the angular momentum of the particle, is related to the fact that the effective potential (4.28) naturally contains the confinement contribution $m^2/R^2(u)$ whose weight increases with m in such a way to enlarge the energy difference between the mini-band edges (because its asymptotic value is positive and given by m^2/R_0^2) and, at the same time, make the potential deeper (because for a bulge the functional form of this term is that of a potential well). To gain more insight on this question, the square modulus of the lowest energy normalized wave functions for same values of both β and ζ with $m = 0$ and $m = \pm 1$ have been calculated. The results are shown in Fig. 4.5 where from the panels (a) and (b) it is seen that, as expected, the wave function shrinks on increasing either ζ or β. The same effect is shown in the panel (c) of the same figure where, given β and ζ, the wave function localization increases upon going from $m = 0$ to $m = \pm 1$.

The richness of the surface electronic structure which is being studied is testified by the existence, for a given m, of several excited states. For the first excited state with both $m = 0$ and $m = \pm 1$, it has been calculated the existence diagram in the (ζ, β) plane whose curves are shown in Fig. 4.3b. The first excited state with $m = 0$ does exist only for $\zeta > 1$ whereas the first excited state with $m = \pm 1$ can be found for any value of ζ.

All the presented results show that on the surface of a deformed quantum wire a very rich surface electronic structure comes out from the surface topology. The consequences of the existence of such surface topological states are numerous. For the optical properties, they may play the role of surface traps or even of active centres for non radiative recombinations. For the transport properties, the existence of both localized and delocalized states may induce a surface channel for the AC electrical conductivity as it has been demonstrated for porous silicon [157]. Moreover, it has been shown [180] that the resistivity of a mesoporous silicon structure is several orders of magnitude higher than that of the substrate, and this has been explained within a charged surface traps model. Finally, because of the possibility of an easy charge transfer between the quantum wire bulk and its surface layers, the surface chemical

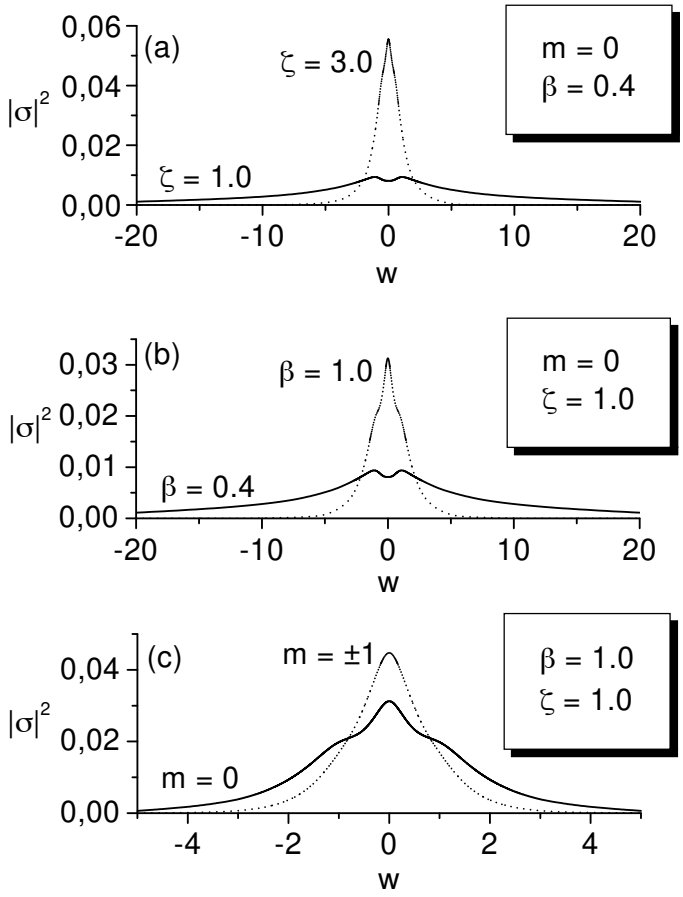

Figure 4.5: Square modulus of the ground-state normalized wave functions for $m = 0$ and $m = \pm 1$ with different values of β and ζ.

reactivity can significantly be enhanced by making a nanostructured material with a disordered surface very interesting for sensor applications.

Porous silicon is the nanostructured semiconductor for which the above consideration may be of relevance. The light-emitting material is composed of undulating wires, that is, a combination of both bulges and constrictions whose surface may support localized states. With the geometrical parameters

calculated in chapter 3 (see eqs. (3.13)) the localized ground surface states with $m = 0$ on a bulge ($\beta > 0$) cannot exist or have an energy of a few meV. For typical values of the parameters as $R_0 = 1.34$ nm, $\Delta z = 2.5$ nm and $\beta = 0.46$ corresponding to an emission energy of 1.7 eV, the ground state with $m = 0$ does not exist while for $m = \pm 1$ an energy of about -13 meV is found. If the same calculation for a constriction characterized by the same parameters indicated above (apart from the value of β which changes sign) is done, it is found for $m = 0$ a localization energy of about -15 meV. These results indicate that if one wants larger localization energies, the overall bulge dimension must be increased ($\zeta > 1$ in Fig. 4.4a). However, it must be pointed out that porous silicon is a very heterogeneous material whose nanostructures have a wide distribution of dimensions [138] with only a small fraction of them emitting light [181]. Most of the materials have nanostructures with dimensions which, in the considered structural model, correspond to the range $\zeta > 1$ and it is therefore in this part of the structure that localized surface ground states may easily form. If, for example, $R_0 = 9$ nm, $\Delta z = 2.5$ nm (that is, $\zeta = 12.96$) and $\beta = 1.0$ a ground state for $m = 0$ with energy of about -105 meV is found. These results suggest that in porous silicon the formation of localized surface states of the type discussed here is favoured in those nanostructures where the light emission is either absent or very inefficient [172–174].

4.3 Topological surface states on a deformed plane

The geometry studied in the previous section can be of interest, as already pointed out, because materials such porous silicon appear just as a collection of deformed quantum nanowires. Nevertheless, many experimental devices which can be commonly encountered are constituted by an interface between two different materials, such as the Si/SiO_2 interface. In this case the problem of the topological surface states can become of particular interest. In fact, on one hand interface properties can give rise just to an accumulation layer of electrons or holes near the interface itself [165, 171]. On the other hand, the interface roughness which is experimentally observed and measured [171] represents a deviation from the ideal, plane surface, which means that the surface which separates the two materials has a curvature that is not constant.

In this section topological surface states which appear on the surface of a deformed plane are investigated, by assuming that the deformation is of Gaussian shape.

4.3.1 Theory

Let us consider the surface with parametric equations

$$\begin{cases} x = \rho\cos\varphi \\ y = \rho\sin\varphi \\ z = z_0\exp(-k\rho^2) \end{cases}, \tag{4.40}$$

with $0 \leq \rho < +\infty$ and $0 \leq \varphi < 2\pi$. z_0 and k are the two parameters which characterize the surface deformation. A simple sketch of this kind of surface is shown in Fig. 4.6. For this surface the matrixes $\mathbf{g}$, $\mathbf{h}$ and $\boldsymbol{\alpha}$ become respectively:

$$\mathbf{g} = \begin{Vmatrix} \dfrac{1}{\mathcal{G}^2(\rho)} & 0 \\ 0 & \rho^2 \end{Vmatrix}, \tag{4.41a}$$

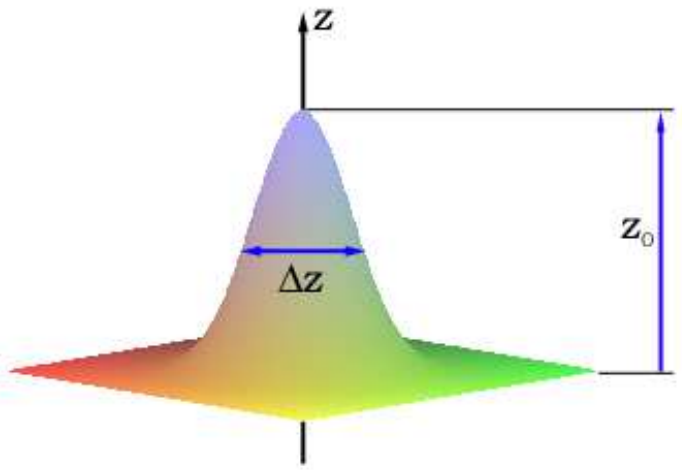

Figure 4.6: The deformed plane surface parameterized in eq. (4.6). z_0 is the deformation height while $\Delta z = \sqrt{\frac{2}{k}}$ can be used as a measure of its extension along the plane.

$$\mathbf{h} = -2kz_0 \exp(-k\rho^2)\mathcal{G}(\rho) \begin{Vmatrix} 1-2k\rho^2 & 0 \\ 0 & \rho^2 \end{Vmatrix} \tag{4.41b}$$

and

$$\boldsymbol{\alpha} = 2kz_0 \exp(-k\rho^2)\mathcal{G}^3(\rho) \begin{Vmatrix} 1-2k\rho^2 & 0 \\ 0 & \dfrac{1}{\mathcal{G}^2(\rho)} \end{Vmatrix}, \tag{4.41c}$$

with

$$\frac{1}{\mathcal{G}^2(\rho)} = 1 + 4k^2 z_0^2 \rho^2 \exp(-2k\rho^2). \tag{4.42}$$

As for the deformed cylindrical wire, it is possible to put the solution of eq. (4.21) in the form:

$$\sigma(\rho,\varphi) = \frac{1}{\sqrt{\rho\,\mathcal{G}(\rho)}} t(\rho) \frac{\exp(im\varphi)}{\sqrt{2\pi}} \tag{4.43}$$

with $m = 0, \pm 1, \pm 2, \ldots$. The φ-dependence of the wave function takes into account the rotational symmetry around the z axis, which means that all the

eigenstates of the full Hamiltonian are eigenfunctions of the z component of the angular momentum as well. Moreover, the extra initial factor has been introduced in such a way that the term of eq. (4.21) containing the first derivative of the wave function with respect to ρ disappears, leading to the Schrödinger-like equation:

$$-\mathcal{G}^2\frac{d^2t}{d\rho^2}+\left[-\mathcal{G}^2\left(\frac{d\Omega}{d\rho}-\Omega^2\right)-\frac{T^2}{4}+D+\frac{m^2}{\rho^2}\right]t(\rho)=(\widetilde{\varepsilon}-\widetilde{\varepsilon}_n)t(\rho) \quad (4.44)$$

where $\Omega(\rho)=-\dfrac{1}{2\rho\,\mathcal{G}(\rho)}\dfrac{d(\rho\mathcal{G})}{d\rho}$. Therefore the motion of the particle confined on the surface is subjected to the potential

$$v(\rho)=-\mathcal{G}^2\left(\frac{d\Omega}{d\rho}-\Omega^2\right)-\frac{T^2}{4}+D+\frac{m^2}{\rho^2}. \quad (4.45)$$

It is interesting to note that the particle is characterized by an effective mass $\mathcal{G}^{-2}<1$. Differently from the case of the deformed cylindrical quantum wire, the potential (4.45) is zero asymptotically (namely, as $\rho\to+\infty$). If we set $w_0=\sqrt{k}z_0$ and $w=\sqrt{k}\rho$, it can be easily seen that the following scaling rules are satisfied:

$$v(\rho)=k\mathcal{V}(w_0,w), \quad (4.46a)$$

$$\frac{1}{\mathcal{G}^2(\rho)}=\mathcal{M}(w_0,w), \quad (4.46b)$$

where $\mathcal{V}$ and $\mathcal{M}$ are two adimensional functions. Eq. (4.44) becomes (the symbol $t(w)$ will be used instead of $t(w/\sqrt{k})$)

$$-\frac{1}{\mathcal{M}(w_0,w)}\frac{d^2t}{dw^2}(w)+\mathcal{V}(w_0,w)t(w)=\gamma t(w) \quad (4.47)$$

where $\gamma=(\widetilde{\varepsilon}-\widetilde{\varepsilon}_n)/k$. In this case the adimensional differential equation (4.47) depends just on one parameter (namely, w_0). Eq. (4.47) must be solved with the normalization condition

$$\frac{1}{\sqrt{k}}\int_0^{+\infty}dw\mathcal{M}(w_0,w)t^2(w)=\int_S dS\sqrt{\det\mathbf{g}}\,|\sigma(\rho,\varphi)|^2=1. \quad (4.48)$$

4.3.2 Results

The main results obtained for curvature-induced localization on deformed interfaces are presented here. Because the main points have already been explained for the deformed wire (subsec. 4.2.2), less details will be given.

In Fig. 4.7 the adimensional energies γ (see above) obtained with $m = 0$ are shown as a function of w_0^2. Let us note that the deformation aspect ratio can be defined as $\delta = z_0/\Delta z = w_0/\sqrt{2}$. It is seen that the modulus of the localization energy increases with w_0 or, equivalently, with the deformation aspect ratio. Moreover, several excited states appear, even if for each state there is a critical aspect ratio value below which it disappears.

The localized wave function square modulus is shown for the ground state with $m = 0$ and for several values of w_0, in Fig. 4.8. It is clear that the surface state localization increases with the aspect ratio.

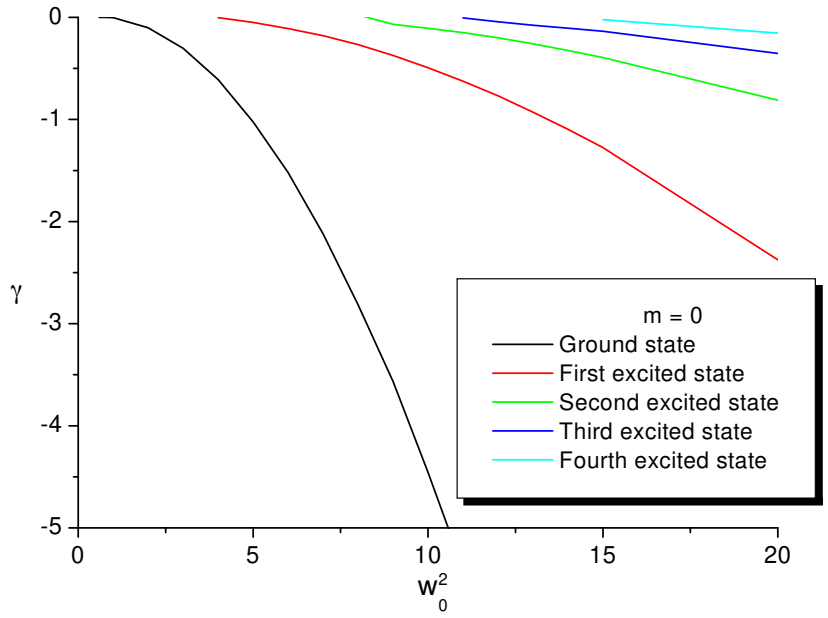

Figure 4.7: Adimensional energy for the ground and the first four excited states with $m = 0$. The increase of the modulus with w_0 clearly comes out.

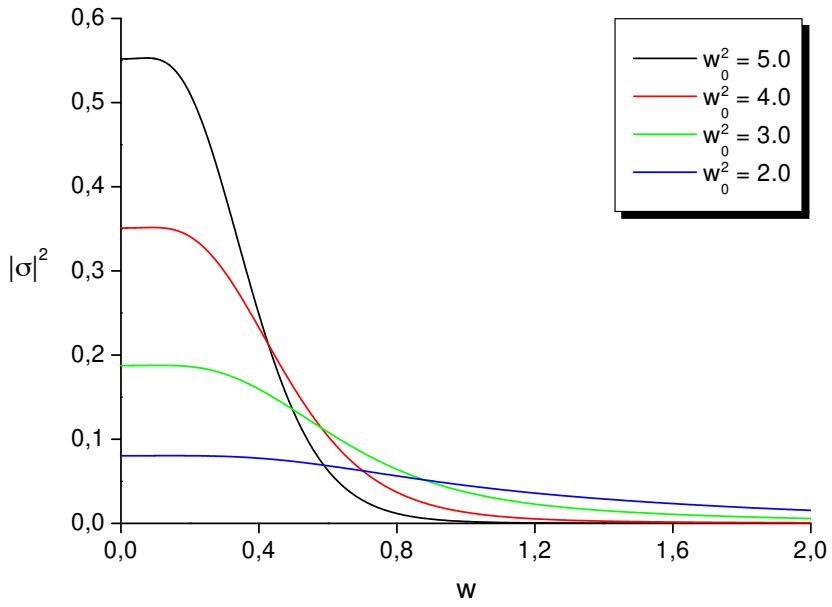

Figure 4.8: Square modulus of the ground-state normalized wave functions for $m = 0$ with different values of w_0.

Finally, let us note that for the deformed wire localized states have been found also with $m = \pm 1$. It has been shown that for a given geometry the corresponding wave functions are more localized than those with $m = 0$. In this case no localized states with $|m| \geq 1$ are found. This is related to the fact that the contribution to the potential (4.45) given by the term containing m tends to push the particle away from the top of the deformation of Fig. 4.6 (therefore, in this case a repulsive contribution is obtained, differently from the case of the deformed wire in which this contribution is attractive).

4.4 Topological surface states on ellipsoid quantum dots

In this section it is shown that topological surface states can arise also on an ellipsoid closed surface [120], as one would expect because of their very general nature.

4.4.1 Theory

The surface curvilinear coordinates (Θ, φ) suitable to describe an ellipsoid surface are defined in eq. (2.1). Let us remember that we are considering an ellipsoid with rotational symmetry around the z axis, that c and a are the semi-axes along the z axis and in the x-y plane respectively, that $\chi = c/a$ represents their ratio and that $0 \leq \Theta \leq \pi$, $0 \leq \varphi < 2\pi$.

For this surface the matrixes $\mathbf{g}$, $\mathbf{h}$ and $\boldsymbol{\alpha}$ become respectively:

$$\mathbf{g} = \begin{Vmatrix} \dfrac{1}{\mathcal{H}^2(\Theta)} & 0 \\ 0 & a^2 \sin^2 \Theta \end{Vmatrix}, \tag{4.49a}$$

$$\mathbf{h} = ac\mathcal{H}(\Theta) \begin{Vmatrix} 1 & 0 \\ 0 & \sin^2 \Theta \end{Vmatrix} \tag{4.49b}$$

and

$$\boldsymbol{\alpha} = -c\mathcal{H}(\Theta) \begin{Vmatrix} a\mathcal{H}^2(\Theta) & 0 \\ 0 & \dfrac{1}{a} \end{Vmatrix}, \tag{4.49c}$$

with

$$\frac{1}{\mathcal{H}^2(\Theta)} = a^2 \cos^2 \Theta + c^2 \sin^2 \Theta. \tag{4.50}$$

Similarly to the previous cases, it is possible to put the solution of eq. (4.21) in the form:

$$\sigma(\Theta, \varphi) = \frac{1}{\sqrt{a \sin \Theta \, \mathcal{H}(\Theta)}} t(\Theta) \frac{\exp(im\varphi)}{\sqrt{2\pi}}, \tag{4.51}$$

which leads to the Schrödinger-like equation:

$$-\mathcal{H}^2(\Theta)\frac{d^2t}{d\Theta^2}+\left[-\mathcal{H}^2(\Theta)\left(\frac{d\Xi}{d\Theta}-\Xi^2\right)-\frac{T^2}{4}+D+\frac{m^2}{a^2\sin^2\Theta}\right]t(\Theta)= (\widetilde{\varepsilon}-\widetilde{\varepsilon}_n)t(\Theta) \tag{4.52}$$

where $\Xi(\Theta)=-\dfrac{1}{2\sin\Theta\,\mathcal{H}(\Theta)}\dfrac{d(\sin\Theta\,\mathcal{H})}{d\Theta}$. Therefore the motion of the particle confined on the surface is subjected to the potential

$$v(\Theta)=-\mathcal{H}^2\left(\frac{d\Xi}{d\Theta}-\Xi^2\right)-\frac{T^2}{4}+D+\frac{m^2}{a^2\sin^2\Theta}. \tag{4.53}$$

Even in this case it can be seen that the particle is characterized by an effective mass $\mathcal{H}^{-2}<1$ and that scaling rules are satisfied, as follows:

$$v(\Theta)=\frac{\mathcal{V}(\chi,\Theta)}{c^2}, \tag{4.54a}$$

$$\frac{1}{\mathcal{H}^2(\Theta)}=c^2\mathcal{M}(\chi,\Theta) \tag{4.54b}$$

where $\mathcal{V}$ and $\mathcal{M}$ are two adimensional functions. Eq. (4.52) becomes [120]:

$$-\frac{1}{\mathcal{M}(\chi,\Theta)}\frac{d^2t}{d\Theta^2}+\mathcal{V}(\chi,\Theta)t(\Theta)=\gamma t(\Theta) \tag{4.55}$$

where $\gamma=(\widetilde{\varepsilon}-\widetilde{\varepsilon}_n)c^2$. As for the deformed plane, the adimensional differential equation (4.55) depends just on one parameter (namely, χ). The normalization condition reads, in this case:

$$c^2\int_0^{\pi}d\Theta\mathcal{M}(\chi,\Theta)t^2(\Theta)=\int_S dS\sqrt{\det\mathbf{g}}\,|\sigma(\Theta,\varphi)|^2=1. \tag{4.56}$$

Because as $\chi\to 1$ the solutions of eq. (4.55) are the associated Legendre functions (as it can be easily shown), it is possible to label eigenvalues and eigenfunctions with two indexes l and m with $m=0,\pm1,\pm2,\dots$ and $l=|m|,|m|+1,|m|+2,\dots$ ($\gamma\equiv\gamma_{l,m}$, $t(\Theta)\equiv t_{l,m}(\Theta)$ and $\sigma(\Theta,\varphi)\equiv\sigma_{l,m}(\Theta,\varphi)$).

4.4.2 Results

Eq. (4.55) has been numerically solved [120] by using a mid-point shooting method. In Fig. 4.9a the calculated energy spectrum is shown. The ground state with $l = m = 0$ and the first two excited states ($m = 0$, $l = 1$, and $l = |m| = 1$) are shown. These last two are degenerate for $\chi = 1$, in which case the ellipsoid degenerate to a sphere and the wave functions become the spherical harmonics $Y_l^m(\Theta, \varphi)$ with energies $\hbar^2 l(l+1)/2m^* R^2$ (if R is the sphere radius). In particular for $\chi = 1$ the ground state has zero energy which corresponds to the fact that the topological potential, being vanishing, is unable to localize the wave function along the surface. This confirms the topological nature of these states, namely their dependence on the system geometry.

The calculation of the ground-state energy has been performed also by solving eq. (4.55) with the variational method. An inspection of the effective potential (4.53) suggests that a good choice of the ground-state trial wave function can be

$$\widetilde{t}_0(\Theta) = \sqrt{(\sin\Theta)}\exp(\Lambda\cos^2\Theta) \tag{4.57}$$

where Λ is a variational parameter which must be determined by the condition of minimum energy. In Fig. 4.9b it is shown the ground-state energy (solid line) and the value of the variational parameter (dashed line) as functions of χ which have been determined in this way. This ground-state energy always represents, as it has to be, an upper bound to the exact one (shown in Fig. 4.9a, black curve) and is in very good accordance with it.

It is of interest to compare the energies of volume confined states with those which are surface localized. By comparing the ground-state energy for the volume confined states (see Figs. 2.4 and 2.5) and surface states (see Fig. 4.9a) it can be seen that these last ones are always (that is, for any χ) below the first ones, confirming what it has been found for the completely different geometry of the deformed quantum wire with an not limited surface.

In Fig. 4.10 it is shown the surface ground-state wave function calculated for $\chi = 4.0$ (a), $\chi = 2.5$ (b) and $\chi = 0.5$ (c). It can be seen that for values of $\chi > 1$ the surface state tends to localize at the positions $\Theta = 0$ and $\Theta = \pi$ while if $\chi < 1$ we find a state localized at $\Theta = \pi/2$. This means that the "Θ-

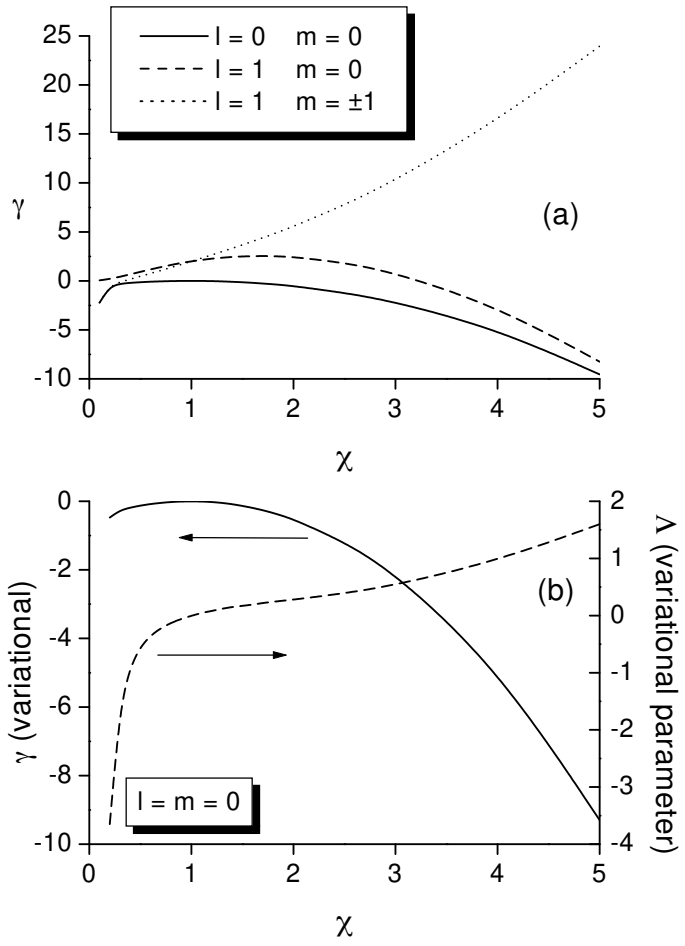

Figure 4.9: (a) The topological surface states energy is shown for the ground state $l = m = 0$ and the first two excited states $l = 1$, $m = 0$ and $l = |m| = 1$. (b) The ground-state energy as calculated by using the variational method (solid line) and the corresponding variational parameter (dashed line) are shown.

localization" of the surface state is opposite to that of the volume confined state. Therefore, the possibility of a charge transfer from the bulk to this particular class of states should be less efficient than on deformed quantum wires (see subsec. 4.2.2).

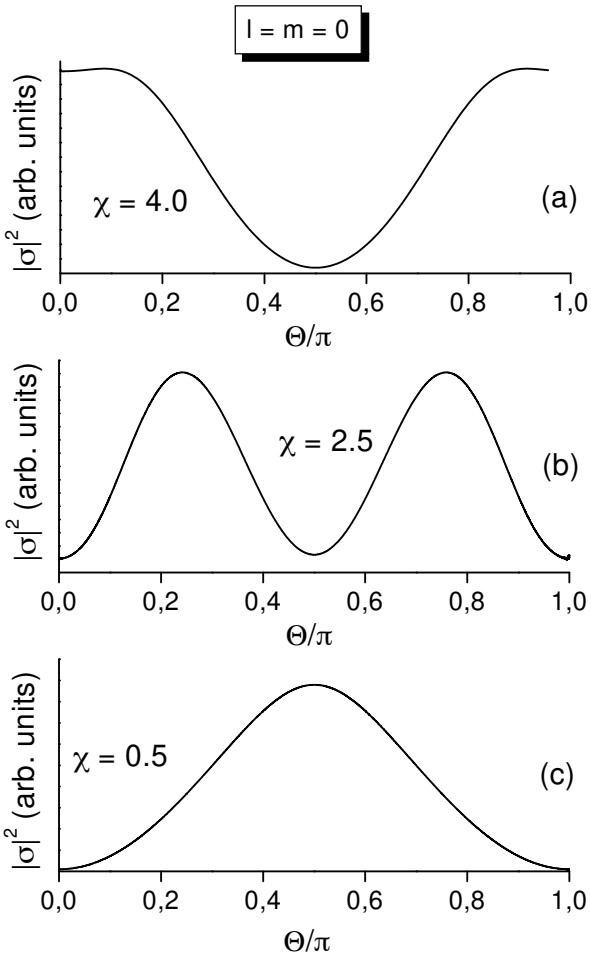

Figure 4.10: Surface ground-state wave functions for $\chi = 4.0$ (a), $\chi = 2.5$ (b) and $\chi = 0.5$ (c). The particle localization as a function of χ behaves in the opposite way to volume confined ground state.

Conclusions

In this thesis work shape-induced effects in nanometric systems have been investigated. The main point is that as the system dimensions are reduced confinement effects become relevant, giving rise to a "new" physics whose nature is strongly related to quantum mechanics. While size effects are widely investigated in the literature, not very much work has been done in establishing if and how the shape of the nanostructure can modify the relevant physical properties. This point becomes particularly interesting if we consider that very recently, as shown in chapter 1, the fabrication of shape-controlled nanocrystals has been experimentally realized. The applications can be very relevant, mainly for all those devices which require, for example, an anisotropic optical response.

First, ellipsoid quantum dots have been investigated (chapter 2). The effective-mass Schrödinger equation has been exactly solved, showing the significant effect of the shape on the single-particle spectrum. The loss of symmetry with respect to the spherical quantum dot determines the removal of degenerations as well as the appearance of accidental degenerations (energy level crossing) absent in the spherical geometry. The geometrical limits of very long quantum rods or very oblate spheroids have been checked, showing the complete accordance with the limit structures (that is, the cylindrical quantum wire and the slab respectively). The inclusion of dielectric effects shows that as far as the infrared transitions are considered, while they significantly modify the single-particle energies, they do not affect their differences (namely, the transition energies) which are the relevant quantities from the experimental point of view.

The effect of the anisotropy has been investigated also with respect to

the optical transitions, showing as selection rules and oscillator strengths are modified in such a way that the radiation polarization along the major axis always becomes the more relevant one.

From all these results, it comes out that the fabrication of shape-controlled ellipsoid quantum dots can have fundamental applications. First, the infrared transition energies can be tuned as a function of both the dot shape and dimensions (see, for example, Fig. 2.8), giving the possibility of tuning the system resonant frequency even keeping constant the dot volume. In other words, asymmetric quantum dots can be realized, with the infrared absorption peak at any infrared wavelength. Second, the control on the ellipsoid aspect ratio allows the fabrication of nanostructures which exhibit light emission and absorption spectra dependent on the radiation polarization. The study presented in this work has been focused on the infrared spectrum, for which experimental data are in practice not yet available (even if there are some experimental evidences, such in Fig. 1.19, where the splitting of the first allowed infrared transition peak could be attributed just to shape effects). However, it must be stressed that experiments done on the photoluminescence emission of anisotropic dots have given a clear evidence for such applications. In particular, single-molecule luminescence spectroscopy measurements on CdSe quantum rods have shown a sharp transition from non-polarized to purely linearly polarized emission if the ellipsoid aspect ratio is varied from 1 to 2, making these nanocrystals ideal for many orientation-sensitive applications [182]. In the same way, it has been shown how by fixing the minor axis a and changing only the major axis c, the emission wavelength can be tuned over the same range as for spherical quantum dots, while the emission from each individual CdSe quantum rod is highly linearly polarized in contrast to the plane-polarized emission from spherical dots [183].

As the dot dimensions increase, many-particle effects can become interesting and important as well, mostly if we think to how much work has been done both experimentally and theoretically to understand the single-electron features of quantum dots (addition spectra, $I - V$ characteristics, etc.). Therefore, just to have an indication on how the shape could modify these properties, the two-electron system has been investigated, within both a perturbative and a variational scheme. This last one has allowed the in-

clusion of the electron-electron (Coulomb and dielectric) correlation effects (not present in the perturbative scheme) and their study as a function of the shape. It has been shown that both the energy spectrum and the two-electron spatial configuration have a substantial change on varying the dot anisotropy. In particular the energy necessary to add a second electron to the dot changes in a quite relevant way. This could be of interest, as soon as the possibility of investigating addition spectra of anisotropic quantum dots will be experimentally available.

The investigation of shape effects can be extended also to *open* quantum dots, namely to confined states which appear if, for example, quantum wires with a deformation are considered. This has been shown in chapter 3, with the aim of explaining some optical properties of porous silicon which experimentally appears just like a collection of wires and dots. By studying an average nanostructure given by a straight cylindrical wire with a Gaussian deformation, some very interesting effects come out. The method used for such a study is based on a variational approach which is in principle applicable to arbitrarily shaped nanostructures and can account for the interaction with an external environment as well.

The main point is that, if suitable geometrical parameters of the deformation are considered, confined states (completely absent in the straight wire) within the bulge appear. Their presence can give a possible, realistic explanation of how all the porous silicon optical spectra show a significant shift between absorption and emission. Absorption can occur between the mini-bands which correspond to delocalized states and are characterized by a large density of states (let us note that they are basically the same as the straight wire). The relaxation towards localized states in the mini-band gap and the following radiative recombination gives rise to an emission energy peak which is lower than the absorption one. This explains the large Stokes shift which is experimentally observed.

The presence of a localized wave function within the deformation together with the finite barrier at the nanostructure boundary makes porous silicon very interesting for sensor applications. In fact, the wave function tail outside the nanostructure makes the deformation very reactive in presence of an external environment. This has been investigated, showing how both the

photoluminescence quenching and red-shift in presence of oxygen (which are experimentally observed phenomena) can be accounted for. In this sense, shape effects become relevant in the sensor application of such systems.

Finally, the presence of structural deformations has been shown to give rise to a new kind of surface states (chapter 4), with topological nature. The motion of a particle in the neighbourhood of a deformed surface can be characterized by the presence of quantum states localized on the deformation. It is not clear at the moment how such states could be observed and/or reproduced experimentally. However, the possibility of surface shape-induced localization can be of interest because the reactivity towards an external environment as well as the optical and transport properties of the system could change because of the presence of such states. Besides, it must be pointed out that the miniaturization of transistor devices down to nanometric scale requires the absence of surface defects of any nature, to ensure a good device efficiency. This study could bring out that also defects extended over many lattice constants can worsen the performances of such devices in presence of surfaces not flat enough. Finally, let us cite as a possible application of such study the interpretation of some aspects of catalysis phenomena, such as their enhancement near rough surfaces [171, 184].

Appendix A

The effective-mass approximation

The theoretical treatment of quantum confinement of electrons and holes within nanostructures can be performed by following several schemes, each one with its advantages and drawbacks. A very common point of view assumes as a starting point the bulk material band structure and describes the electric and optical properties of the material by accounting for the effects of the periodic crystalline potential and of the many-body interactions within the crystal just by a renormalization of the particle mass. This corresponds to the assumption that only the zone centre of the energy bands of the bulk material significantly contributes to determine the material properties and that near the centre these bands can be approximated with a quadratic dispersion law. Within this scheme, which is the one used in this thesis work, quantum confinement in nanostructures can be described as a confining potential in which the particle moves with a renormalized mass.

There are obviously other approaches, which start from an atomistic description and simulate the lattice atoms arrangement within the nanostructure. If dimensions small enough are considered, the number of surface atoms becomes comparable with the total number of atoms contained in the structure. In this case the description starting from the bulk material band structure is expected to fail and the microscopic arrangement of the lattice atoms must be properly taken into account, by including strain and surface effects,

which are negligible for large structures.

In sec. A.1 the perturbative $\vec{k} \cdot \vec{p}$ method is described, showing how the band structure of a given material can be calculated around a band extremum point. This leads to the so-called *effective-mass approximation*, which as already stressed above consists in accounting for the microscopic lattice structure just by a mass renormalization.

If, in addition to the crystalline potential, an external potential is present, the particle motion can be studied within the *envelope wave function* method, described in sec. A.2. It is shown how by using both the effective-mass and the envelop wave function approximations, a very simple equation is reached, which describes a particle with a renormalized mass moving just in the external potential.

Finally, some remarks are done in sec. A.3 about the use of such approximations for the study of nanostructures.

A.1 The $\vec{k} \cdot \vec{p}$ method

It is known that the many-body Hamiltonian of an "ideal" lattice can be treated by reducing it to a single-particle Hamiltonian with a self-consistent potential which contains the contributions arising from the interaction of each electron with both the periodic potential of the crystal lattice and the other electrons. The details of the approximations involved in such a picture can be found in many standard solid state physics textbooks [26, 132] and will not be discussed. Here it is enough to stress that it is possible to derive a single-particle Schrödinger equation which describes the motion of each electron, as follows:

$$\left[\frac{p^2}{2m_e} + V(\vec{r})\right] \psi(\vec{r}) = E\psi(\vec{r}), \tag{A.1}$$

where $V(\vec{r})$ is the self-consistent mean potential which has the same periodicity of the crystal lattice. The Hamiltonian on the left hand of eq. (A.1) (which will be referred to as the crystalline Hamiltonian $H_{\rm cr}$) is invariant for translations generated by any vector belonging to the crystal lattice. By

symmetry considerations it can be shown that the Bloch's theorem holds, that is, the most general solution of eq. (A.1) can be written has

$$\psi_{n,\vec{k}}(\vec{r}) = \frac{1}{\sqrt{V}} \exp(i\vec{k}\cdot\vec{r}) u_{n,\vec{k}}(\vec{r}), \tag{A.2}$$

where $\vec{k}$ ranges through the first Brilluoin zone (according to the Born-von Karman boundary conditions) and $u_{n,\vec{k}}(\vec{r})$ is a periodic function with the same period of the crystal lattice. The wave function (A.2) has been normalized for the crystal volume V. The quantum number n labels the energy bands. For each fixed n, the quantum states within the same band are labelled with $\vec{k}$. By substituting eq. (A.2) in the single-particle Schrödinger equation (A.1), it is easy to show that the periodic part of the Bloch's function $u_{n,\vec{k}}(\vec{r})$ must satisfy the following equation:

$$\left[\frac{p^2}{2m_e} + \frac{\hbar\vec{k}\cdot\vec{p}}{m_e} + \frac{\hbar^2k^2}{2m_e} + V(\vec{r})\right] u_{n,\vec{k}} = E_{n,\vec{k}} u_{n,\vec{k}} \,. \tag{A.3}$$

At $\vec{k} = (0,0,0)$ eq. (A.3) becomes

$$\left[\frac{p^2}{2m_e} + V(\vec{r})\right] u_{n,\vec{0}} = E_{n,\vec{0}} u_{n,\vec{0}} \,. \tag{A.4}$$

Because $u_{n,\vec{0}}$ is a periodic function, this equation is easier to solve than the general single-particle equation. Its solutions form a complete orthonormal set of basis functions. If it is assumed that $E_{n,\vec{0}}$ and $u_{n,\vec{0}}$ are known, the additional terms $\dfrac{\hbar\vec{k}\cdot\vec{p}}{m_e}$ and $\dfrac{\hbar^2k^2}{2m_e}$ on the left hand of eq. (A.3) for a generic wave vector $\vec{k}$ can be treated perturbatively by using either non-degenerate or degenerate perturbation theory. This is known as $\vec{k}\cdot\vec{p}$ method. The same procedure can be followed by writing eq. (A.3) around any point $\vec{k}_0$, provided that the complete set of eigenfunctions relative to this wave vector or at least the matrix elements on this basis of $\vec{p}$ can be calculated. In this way the crystal band structure around any point in the Brilluoin zone can be known.

Let us consider a band which has an extremum around $\vec{k} = 0$ and which is not degenerate at this point. For example, this is the case of the conduction

band minimum of direct-gap semiconductors such as CdSe and CdS. By using the non-degenerate perturbation theory both the eigenfunctions $u_{n,\vec{k}}$ and the eigenvalues $E_{n,\vec{k}}$ at a given point $\vec{k}$ near to the band extremum can be expanded respectively to the first and second order in k using the unperturbed wave functions $u_{n,\vec{0}}$ and eigenvalues $E_{n,\vec{0}}$. We get

$$u_{n,\vec{k}} = u_{n,\vec{0}} + \frac{\hbar}{m_e} \sum_{n' \neq n} \frac{\langle u_{n,\vec{0}} | \, \vec{k} \cdot \vec{p} \, | u_{n',\vec{0}} \rangle}{E_{n,\vec{0}} - E_{n',\vec{0}}} u_{n',\vec{0}}, \tag{A.5}$$

$$\begin{aligned} E_{n,\vec{k}} &= E_{n,\vec{0}} + \frac{\hbar^2 k^2}{2m_e} + \frac{\hbar^2}{m_e^2} \sum_{n' \neq n} \frac{\left| \langle u_{n,\vec{0}} | \, \vec{k} \cdot \vec{p} \, | u_{n',\vec{0}} \rangle \right|^2}{E_{n,\vec{0}} - E_{n',\vec{0}}} \\ &= E_{n,\vec{0}} + \frac{\hbar^2}{2} \sum_{i,j=1}^{3} \left(\frac{1}{m^*} \right)_{ij} k_i k_j, \end{aligned} \tag{A.6}$$

where in the eigenvalues expression the terms linear in $\vec{k}$ are null because $\vec{k} = \vec{0}$ represents an extremum point. The reciprocal effective-mass tensor defined as

$$\begin{aligned} \left(\frac{1}{m^*} \right)_{i,j} = \frac{\delta_{i,j}}{m_e} + \frac{1}{m_e^2} \sum_{n' \neq n} \Bigg\{ & \left[\langle u_{n,\vec{0}} | \, \vec{p}_i \, | u_{n',\vec{0}} \rangle \langle u_{n',\vec{0}} | \, \vec{p}_j \, | u_{n,\vec{0}} \rangle \right. \\ & \left. + \langle u_{n,\vec{0}} | \, \vec{p}_j \, | u_{n',\vec{0}} \rangle \langle u_{n',\vec{0}} | \, \vec{p}_i \, | u_{n,\vec{0}} \rangle \right] \frac{1}{E_{n,\vec{0}} - E_{n',\vec{0}}} \Bigg\} \end{aligned} \tag{A.7}$$

has been introduced[1]. It describes the properties of the n-th band near the point $\vec{k} = 0$. Its actual form depends on the crystal structure. Anyway, some remarks can be done. For cubic crystals, symmetry considerations show that the inverse mass tensor becomes:

$$\left(\frac{1}{m^*} \right)_{i,j} = \left(\frac{1}{m_e} + \frac{2}{m_e^2} \sum_{n' \neq n} \frac{\left| \langle u_{n,\vec{0}} | \, \vec{p} \, | u_{n',\vec{0}} \rangle \right|^2}{E_{n,\vec{0}} - E_{n',\vec{0}}} \right) \delta_{i,j} = \frac{1}{m^*} \delta_{i,j}, \tag{A.8}$$

[1]The additional index n should be appended to indicate the band which the tensor is referred to. It is omitted for simplicity of notation.

that is, it is diagonal. The effective mass m^* of the n-th band depends on the matrix elements $\langle u_{n,\vec{0}} | \vec{p} | u_{n',\vec{0}} \rangle$ and the distance between the considered band and all the other ones. However, the main contribution to the effective mass at a given extremum arises from the nearest band. In particular, for a minimum point the nearest band is below the considered one (that is, $E_{n'}(\vec{0}) < E_n(\vec{0})$) and a positive mass is obtained. On the contrary, for a maximum point a negative electronic mass is obtained (positive if the description in terms of holes is used). This explains qualitatively why insulators with small energy gaps have small effective masses and vice-versa.

The extension of this method to the calculation of the band dispersion near a degenerate or a nearly degenerate band extremum is also possible but will not be discussed here (see, for example, ref. [185]).

A.2 The envelope wave function approximation

In the previous section it has been shown that if the electronic energy levels around a band extremum point are considered, it is possible to obtain a quadratic dispersion law for that band by defining an effective-mass tensor. Moreover, for crystals with particular symmetries this tensor is diagonal and therefore it is possible to define an effective electronic mass. In this section it is shown that, if the motion in a slowly varying external potential is considered, the electron motion can be described as that of a free particle in the same potential, the effect of the crystal periodic potential being taken into account by just assigning to this particle the electron effective mass.

Let us consider an electron moving inside a crystal with an additional potential $U(\vec{r})$. The solution of the Schrödinger equation

$$[H_{\mathrm{cr}} + U(\vec{r})]\, \psi(\vec{r}) = E\psi(\vec{r}) \tag{A.9}$$

can be found by expanding the function $\psi(\vec{r})$ over the basis of the Bloch's functions, as follows:

$$\psi(\vec{r}) = \sum_{n,\vec{k}} C_{n,\vec{k}} \psi_{n,\vec{k}}. \tag{A.10}$$

By considering that $\psi_{n,\vec{k}}$ is an eigenfunction of $H_{\rm cr}$ with eigenvalue $E_n(\vec{k})$, eq. (A.9) becomes:

$$E_{n,\vec{k}}C_{n,\vec{k}} + \sum_{n',\vec{k}'} < n,\vec{k}|U|n',\vec{k}' > C_{n',\vec{k}'} = EC_{n,\vec{k}}, \tag{A.11}$$

with

$$< n,\vec{k}|U|n',\vec{k}' >= \frac{1}{NV_0}\int_{V_0} d\vec{r}\exp\left[i(\vec{k}'-\vec{k})\cdot\vec{r}\right] u^*_{n,\vec{k}}(\vec{r})U(\vec{r})u_{n',\vec{k}'}(\vec{r}). \tag{A.12}$$

Here V_0 is the volume of the lattice primitive cell and N the number of primitive cells contained in the crystal volume V ($V = NV_0$). The external potential can be expanded in a Fourier series as follows:

$$U(\vec{r}) = \sum_{\vec{K}} \widetilde{U}_{\vec{K}} \exp(i\vec{K}\cdot\vec{r}). \tag{A.13}$$

By supposing that this potential is a slowly varying function of $\vec{r}$ (with respect to the crystal lattice period), the sum (A.13) can be truncated at small values of $|\vec{K}|$. Under this hypothesis it is possible to show [186] that eq. (A.11) becomes:

$$E_{n,\vec{k}}C_{n,\vec{k}} + \sum_{\vec{K}} \widetilde{U}_{\vec{K}} C_{n,\vec{k}-\vec{K}} = EC_{n,\vec{k}}. \tag{A.14}$$

This last equation does not mix different bands (that is, if the external potential is sufficiently smooth it cannot induce inter-band transitions), so that the sum over n in eq. (A.10) can be neglected. Finally, by introducing the *envelope wave function*

$$F_n(\vec{r}) = \frac{1}{\sqrt{V}}\sum_{\vec{k}} \exp(i\vec{k}\cdot\vec{r})C_{n,\vec{k}}, \tag{A.15}$$

it can be shown that eq. (A.14) becomes:

$$\left[E_n(-i\vec{\nabla}) + U(\vec{r})\right] F_n(\vec{r}) = EF_n(\vec{r}). \tag{A.16}$$

The last equation shows that for sufficiently smooth external potentials, it is possible to find the electronic spectrum by treating $\hbar\vec{k}$ exactly has the

quantum mechanics momentum operator (which means that the classical Hamiltonian - quantum mechanics correspondence is obtained with the prescription that $\hbar\vec{k} \rightarrow -i\hbar\vec{\nabla}$). In the effective-mass approximation we have $E_{n,\vec{k}} = E_{n,\vec{0}} + \hbar^2 k^2/2m^*$, so that eq. (A.16) becomes:

$$\left[-\frac{\hbar^2}{2m^*}\vec{\nabla}^2 + U(\vec{r})\right] F_n(\vec{r}) = \left[E - E_n(\vec{0})\right] F_n(\vec{r}), \tag{A.17}$$

which is just the Schrödinger equation of a particle of mass m^* moving in the external potential $U(\vec{r})$. In the same approximation eq. (A.10) becomes

$$\psi(\vec{r}) \simeq \frac{1}{\sqrt{V}} \sum_{\vec{k}} C_{n,\vec{k}} \exp(i\vec{k}\cdot\vec{r}) u_{n,\vec{0}}(\vec{r}) = F_n(\vec{r}) u_{n,\vec{0}}(\vec{r}). \tag{A.18}$$

This means that in this case the effect of the external potential on the electron wave function is the modulation of the Bloch's function $u_{n,\vec{0}}(\vec{r})$ with the function $F_n(\vec{r})$. From eq. (A.18) the normalization condition for this function is $\int d\vec{r}\,|F(\vec{r})|^2 = 1$.

A.3 Some remarks about the study of nanostructures

The simplest way of describing the motion of electrons and holes within a nanostructure is to assume that the quantum confinement arises from an infinite potential well (hard wall boundary conditions)

$$V(\vec{r}) = \begin{cases} 0 & \text{inside the nanostructure} \\ +\infty & \text{outside the nanostructure} \end{cases} . \tag{A.19}$$

If S indicates the nanostructure surface, the presence of the potential (A.19) corresponds to solving the effective-mass Schrödinger equation (A.17) with the boundary condition $F(\vec{r})|_{\vec{r}\in S} = 0$. This can be easily done for geometries which allow the separation of this equation. Typical examples have been shown in chapter 2, where the solutions for a cylindrical quantum wire (eqs. (2.62)), a slab (eqs. (2.63)), a spherical quantum dot (eqs. (2.19)) and an

ellipsoid quantum dot (eqs. (2.18)) calculated within this scheme have been given.

Many other theoretical models based on the effective-mass approximation have been done for investigating the single and many particle features of quantum confinement in low-dimensional structures (see references at the beginning of chapter 2). Extensions of the effective-mass approximation for nanostructures with a degenerate valence band have also been done [118,119] as well as many band effects (which lead to a non-parabolic energy spectrum) have been investigated [187,188] in the framework of the Kane's model [189][2]. Finally, generalized boundary conditions for the envelope wave function have been done, to take into account the presence of interface states at the quantum dot surface [190, 191]. However, it must be stressed that if too small dimensions are considered, the effect of the surface becomes very relevant. In this case an atomistic description is needed, because the simpler effective-mass approximation, which starts from the bulk crystal band structure, fails. One of the main reasons is that for small dimensions high confinement energies are achieved. This means that energy states far from the Brilluoin zone centre are involved, and the effect of band non-parabolicities are relevant. In this case an overestimation of the confinement energy is usually achieved [16]. Moreover, the effect of inter-facial strain and surface states leads to inter-band coupling and wave function decay outside the nanostructure, which can be properly described only by using an atomistic approach [192, 193]. The study of nanostructures where such effects make the effective-mass approximation failing can be done by using several approaches (see also ref. [25]) such as

[2]In particular, it has been shown that it is possible to analytically take into account the finite barrier at the nanostructure boundary and the non-parabolicity (valence- and conduction-band mixing). It comes out that for either quantum wells deep enough or large nanostructure dimensions the electron envelop wave function is null at the boundary, as in the parabolic single-band model used in this thesis. Moreover, a self-consistent equation is derived, which gives the corrections to the confined electrons energy levels with respect to the simpler effective-mass approximation, due to the conduction band non-parabolicity. These corrections are size-dependent. If a spherical quantum dot with radius $R > 5$ nm is considered, it is found that the single-electron ground-state energy varies at most of a few meV.

- non-local pseudo-potential semi-empirical method [133, 134, 194–198],
- local pseudo-potential empirical method [199–202] or empirical tight-binding method [203–210] which assume the transferability of the bulk-band structure parameters to the nanostructure,
- *ab initio* pseudo-potential methods [211–214],
- Wannier functions approach [215–217],

etc. The details of the advantages and drawbacks of each of these methods will not be treated here.

In this thesis work the effective-mass approximation is widely used, with the awareness that if on one hand this approach has the highest degree of flexibility, on the other hand care must be taken in choosing the lowest nanostructure dimension tractable within this scheme. However, it must be stressed that mainly conduction band electrons properties have been studied, which gives a wider applicability of the effective-mass approximation, the main problems arising from confined states near the degenerate top valence band. Moreover, the study which has been done is mainly focused in bringing out how the nanostructure spectrum changes in presence of a deformation, rather than bands mixing and degeneracy effects which have already been studied by many authors and are not of interest here. An all inclusive calculation, most if applied to nanostructures with a large number of atoms, even if in principle possible, would be very demanding and perhaps give, for the dimensions which have been considered, results not very different from the ones which have been shown.

Appendix B

The Schrödinger equation in spheroidal coordinates

In this appendix some more details about the solution of the Schrödinger equation in spheroidal coordinates are given. First, mathematical aspects will be underlined. Second, a brief discussion about the numerical problems involved in the determination of the electronic confined spectrum in ellipsoid quantum dots will be presented.

B.1 Some mathematical aspects

The separation of the Schrödinger equation in prolate spheroidal coordinates leads, as seen in subsec. 2.1.1, to a radial equation (eq. (2.10a)) and an angular equation (eq. (2.10b)). They are formally equivalent but must be solved in different ranges of the respective variables, which means that the radial equation involves the behaviour of the solution for ξ ranging between the singular point $+1$ and $+\infty$ while the angular equation involves the behaviour of the solution for η ranging between the two singular points -1 and $+1$. These equations are coupled by both the separation constant A and h (proportional to the eigenvalue). From a mathematical point of view the calculation scheme is the following [131]:

- the solution of the angular equation is written in terms of a series

of associated Legendre functions, always possible because they form a complete basis set for functions defined in $[-1,+1]$:

$$S(\eta) = \sum_{s=0}^{+\infty} d_s P_{|m|+s}^{|m|}(\eta); \tag{B.1}$$

- by inserting eq. (B.1) into eq. (2.10b) the following recursion formula relating successive coefficients is obtained [122]:

$$\begin{aligned} &\frac{s(s-1)h^2}{(2s+2|m|-1)(2s+2|m|-3)} d_{s-2} + \\ &\qquad h^2 \frac{(s+2|m|+1)(s+2|m|+2)}{(2s+2|m|+3)(2s+2|m|+5)} d_{s+2} + \\ &\qquad \left[h^2 \frac{2(s+|m|)(s+|m|+1) - 2m^2 - 1}{(2s+2|m|+3)(2s+2|m|-1)} + \right. \\ &\qquad \left. (s+|m|)(s+|m|+1) - A \right] d_s = 0 \quad s = 2,3,4,\ldots, \end{aligned} \tag{B.2}$$

  which couples either all the odd coefficients or all the even ones. This reflects the system invariance for parity transformations, which means that the most general solution of eq. (B.2) can be found with the initial conditions $d_0 \neq 0, d_1 = 0$ or, vice-versa, $d_0 = 0, d_1 \neq 0$;

- eq. (B.2) must be solved for fixed m and h. It comes out that for most values of A the solution S which is obtained is finite at $\eta = +1$ but infinite (not regular) at $\eta = -1$. Anyway, by solving that equation by using the continued-fraction technique [124, 131], the result is that a convergent series in all the interval $[-1,+1]$ is obtained for a discrete set of values of A. As already pointed out, there are actually two independent sets of values of A which give a regular solution, the first one corresponding to even values of s, the second one corresponding to odd values of s. If we arrange each set in order of increasing values of A and label these values with an index l we get $A \equiv A_{l,|m|}(h)$ with $A_{l,|m|}(h) < A_{l+1,|m|}(h)$. For each fixed m and h, the lowest value of A is labelled $A_{|m|,|m|}(h)$, the next one $A_{|m|+1,|m|}(h)$, and so on. The set of

corresponding eigenfunctions $S_{l,m}$, where $l = |m|, |m|+1, |m|+2, \ldots$ (with fixed m), is orthogonal;

- as already pointed out in subsec. 2.1.1, as $h \to 0$, the equation for S reduces to that for a single associated Legendre function $P_l^m(\eta)$. The function S can be normalized so that its behaviour near $\eta = 1$ is close to that of P, independently from the value of h, namely:

$$\lim_{\eta \to 1} S_{l,m}(h, \eta) = P_l^m(1). \tag{B.3}$$

This leads to the following normalization condition for the coefficients $d_s^{l,|m|}$:

$$\sum_{s=0,1}^{+\infty\,\prime} \frac{(s+2|m|)!}{s!} d_s^{l,|m|}(h) = \frac{(l+|m|)!}{(l-|m|)!}, \tag{B.4}$$

where the primate sum has the same meaning as in subsec. 2.1.1 (it runs only over even values of s, starting from 0, if $l-m$ is even and only over odd values of s, starting from 1, if $l-m$ is odd);

- power series as $h \to 0$ and asymptotic expansions as $h \to +\infty$ can be obtained both for the coefficients $d_s^{l,|m|}(h)$ and the separation constant $A_{l,|m|}(h)$. The unknown coefficients of these power series or asymptotic expansions can be calculated by inserting these expansions and the series (2.11b) into eq. (2.10b) [124, 131];

- the series coefficient for the radial solution turn out to be related to the $d_s^{l,|m|}(h)$ via the following relation [122]:

$$a_s^{l,|m|}(h) = (-1)^{\frac{l-|m|-s}{2}} \frac{(s+2|m|)!}{s!} \frac{(l-|m|)!}{(l+|m|)!} d_s^{l,|m|}(h). \tag{B.5}$$

By using this relation, eq. (B.4) can be rewritten as:

$$\sum_{s=0,1}^{+\infty\,\prime} (-1)^{\frac{(l-|m|-s)}{2}} a_s^{l,|m|}(h) = 1, \tag{B.6}$$

which corresponds to the requirement

$$je_{l,m}(h,\xi) \underset{\xi\to+\infty}{\simeq} j_l(h\xi). \tag{B.7}$$

This requirement is consistent with the fact that as $\xi \to +\infty$ we have $\sqrt{\xi^2-1} \simeq \xi$ which means that the ellipsoid surfaces ξ = constant become nearly spherical.

The calculation scheme for oblate spheroidal coordinates, is exactly the same. In this case the starting point is given by eqs. (2.16a) and (2.16b) (instead of eqs. (2.10a) and (2.10b)). As for the previous case, they are formally equivalent but must be solved in different ranges of the respective variables (the radial equation involves the behaviour of the solution for ξ ranging between 0 and $+\infty$ while the angular equation involves the behaviour of the solution for η ranging between the two singular points -1 and $+1$). However, it is worth noting that a simple transformation makes prolate coordinates into oblate coordinates, as follows:

$$\begin{array}{l} \xi \to -i\xi \\ f \to if \\ h \to ih \end{array} \quad . \tag{B.8}$$

Therefore, it is also possible in principle to get solutions for the Schrödinger equation in oblate spheroidal coordinates, just solving the equations for prolate spheroidal coordinates (eqs. (2.10a) and (2.10b)), for complex values of their arguments, as indicated in eq. (B.8). In other words, if $je_{l,m}^{(\mathrm{prol})}(h,\xi)$ and $S_{l,m}^{(\mathrm{prol})}(h,\eta)$ are the prolate functions of the prolate coordinates ξ and η and parameter h, $je_{l,m}^{(\mathrm{obl})}(h,\xi) = je_{l,m}^{(\mathrm{prol})}(ih,-i\xi)$ and $S_{l,m}^{(\mathrm{obl})}(h,\eta) = S_{l,m}^{(\mathrm{prol})}(ih,\eta)$ are the oblate functions of the oblate coordinates ξ and η and parameter h. In particular, the recursion equation for the angular solution series expansion, is obtained from eq. (B.2) just by replacing h^2 with $-h^2$.

B.2 The numerical solution

The solution of both the angular equation for fixed l, m and h and the radial equation for fixed l and m and with hard walls boundary conditions is a Sturm-Liouville problem. The general problem is to find a specified eigenvalue Λ of a self-adjoint differential equation of the second-order

$$\frac{d}{dx}\left[P(x)\frac{d}{dx}g(x)\right] + Q(x;\Lambda)g(x) = 0 \quad x_1 < x < x_2, \tag{B.9}$$

together with boundary conditions at the two end-points x_1 and x_2 in the form

$$a_2 g(x_1) = a_1 P(x_1)\frac{d}{dx}g(x_1), \tag{B.10a}$$

$$b_2 g(x_2) = b_1 P(x_2)\frac{d}{dx}g(x_2). \tag{B.10b}$$

We do not want to enter the details of the mathematical problem, which can be found in many mathematical textbooks (see, for example, [218]). It is enough to stress that under suitable conditions the numerical solution of this problem can be numerically attempted by performing a Pruefer transformation [218, 219] first, and then by using a *shooting method* [220]. In particular we must require that $P(x)$ is non-zero and of constant sign throughout $[x_1, x_2]$ and that $\dfrac{\partial Q}{\partial \Lambda}$ is, as a function of x and for fixed Λ, of constant sign and non-zero throughout (x_1, x_2).

The values of $P(x)\dfrac{d}{dx}g(x)$ and $g(x)$ at both x_1 and x_2 must be given (actually just their ratio is needed). Each regular solution is called, as it is known, an eigenfunction of the eq. (B.9), and the corresponding value of Λ its eigenvalue.

The following table shows the boundary conditions used for the radial equation both for prolate and oblate ellipsoids. By comparing eq. (B.9) with eqs. (2.10a) and (2.16a) respectively, it is straightforward to get the explicit form for $P(x)$ and $Q(x;\Lambda)$. In this case we have $\Lambda = h^2$ while the separation constant A is a parameter.

	$\chi > 1$	$\chi < 1$
$P(\xi)$	$\xi^2 - 1$	$\xi^2 + 1$
$Q(\xi;\Lambda)$	$-\left(A - \Lambda\xi^2 + \frac{m^2}{\xi^2 - 1}\right)$	$-\left(A - \Lambda\xi^2 - \frac{m^2}{\xi^2 + 1}\right)$
$\xi_1 \equiv x_1$	1	0
$g(\xi_1)$	$(\xi_1 - 1)^{\frac{\lvert m\rvert}{2}}$	1 if $l-m$ is even 0 if $l-m$ is odd
$P(\xi_1)\frac{dg}{d\xi}(\xi_1)$	$\lvert m\rvert g(\xi_1)$	0 if $l-m$ is even 1 if $l-m$ is odd
$\xi_2 \equiv x_2$	$\overline{\xi}$	$\overline{\xi}$
$g(\xi_2)$	0	0
$P(\xi_2)\frac{dg}{d\xi}(\xi_2)$	1	1

Table B.1: The boundary conditions used for both prolate and oblate ellipsoids to solve the radial Sturm-Liouville problem.

Similarly, boundary conditions for the angular problem can be get by comparing eq. (B.9) with eqs. (2.10b) or (2.16b), as shown in table B.2. In this case h is a parameter, while $\Lambda = A$.

The numerical problem in getting the ellipsoid quantum dot confined spectrum is, as pointed out in subsec. 2.1.1, that the angular and radial equation are coupled by both the separation constant and the eigenvalue. Actually, only the solution of the radial equation would be enough to give the spectrum, but this solution requires the knowledge of the separation constant as a function of h. A way of skipping this problem consists in using tabulated power series or asymptotic expansions of the function $A(h)$ (see above), but it has been verified that it works as $h \to 0$ and $h \to +\infty$, while there is a region of values of h in which neither the power series expansion nor the asymptotic one provide enough accurate values of A. This gives not very good numerical evaluations for those eigenvalues which correspond to values of h ranging in this intermediate region. Therefore, a recursive method has been used. Let us suppose we want to determine the eigenvalue $E^v_{n,l,m}$

	$\chi > 1$	$\chi < 1$
$P(\eta)$	$1-\eta^2$	$1-\eta^2$
$Q(\eta;\Lambda)$	$\left(\Lambda - h^2\eta^2 - \frac{m^2}{1-\eta^2}\right)$	$\left(\Lambda + h^2\eta^2 - \frac{m^2}{1-\eta^2}\right)$
$\eta_1 \equiv x_1$	-1	
$g(\eta_1)$	$(1+\eta_1)^{\frac{\lvert m\rvert}{2}}$	
$P(\eta_1)\frac{d}{d\eta}g(\eta_1)$	$\lvert m\rvert g(\eta_1)$	
$\eta_2 \equiv x_2$	$+1$	
$g(\eta_2)$	$(1-\eta_2)^{\frac{\lvert m\rvert}{2}}$	
$P(\eta_2)\frac{dg}{d\eta}(\eta_2)$	$-\lvert m\rvert g(\eta_2)$	

Table B.2: The boundary conditions used for both prolate and oblate ellipsoids to solve the angular Sturm-Liouville problem.

corresponding to $h = h_{n,l,m}$. The following iteration procedure is followed:

i. an initial value $h^{(0)}_{n,l,m}$ is assigned to $h_{n,l,m}$;

ii. by fixing $h = h^{(0)}_{n,l,m}$, the $(l - |m| + 1)$-th eigenvalue of the angular equation is calculated by using the numerical algorithms cited above. The eigenvalue which is obtained is $A^{(0)}_{l,m} = A_{l,|m|}(h^{(0)}_{n,l,m})$;

iii. this value of the separation constant is used in the radial equation to calculate its n-th eigenvalue. This gives a new value of h, let us say $h = h^{(1)}_{n,l,m}$;

iv. this value of h is compared with the initial estimation and the previous steps are repeated till convergence has been achieved within a required error.

It must be pointed out that the mathematical solution of the problem is exact, because series or asymptotic expansions with respect to h can be obtained up to any order. Nevertheless, as pointed out above, it is not possible to provide

a closed form expression for the solutions, because the recursion equations for the coefficients have not an analytical solution. This is the reason why a numerical approach is needed. The eigenvalues are in this way determined by the number of steps performed in the described iterative procedure (in principle it can be increased as much as needed) and by the precision of the numerical algorithm used to solve the Sturm-Liouville problem. Some checks have been done in this respect, showing that the eigenvalues can be determined with precision of the order of 0.01%. This is what we mean when we say that we give a numerical, exact solution of the problem.

Acknowledgments

The first thank must surely go to Prof. Giuseppe Iadonisi and Prof. Domenico Ninno, who have given a fundamental contribution to this thesis with continuous suggestions and critical discussions. Their teachings and their support, both scientific and human, have been for me very important.

Thanks to Dr. Francesco Buonocore for helpful and stimulating discussions.

A special thank to my family, who has always supported me.

Financial support from the European Social Found, ENEA under contract No.2000/29324 and Istituto Nazionale per la Fisica della Materia is acknowledged.

List of Figures

List of Tables

Bibliography

[1] N. Lane, *National Nanotechnology Initiative: Leading to the Next Industrial Revolution*, US National Science and Technology Council, February 2000.

[2] M. A. Kastner, *Rev. Mod. Phys.* **64**, 849 (1992).

[3] M. Kastner, *Nature* **389**, 667 (1997).

[4] D. L. Klein, R. Roth, A. K. L. Lim, A. P. Alivisatos and P. L. McEuen, *Nature* **389**, 699 (1997).

[5] L. Zhuang, L. Guo and S. Y. Chou, *Appl. Phys. Lett.* **72**, 1205 (1998).

[6] M. H. Devoret and R. J. Schoelkopf, *Nature* **406**, 1039 (2000).

[7] A. Fujiwara and Y. Takahashi, *Nature* **410**, 560 (2001).

[8] M. Grundmann, *Physica E* **5**, 167 (2000) and references therein.

[9] V. I. Klimov, A. A. Mikhailovsky, S. Xu, A. Malko, J. A. Hollingsworth, C. A. Leatherdale, H.-J. Eisler and M. G. Bawendi, *Science* **290**, 314 (2000).

[10] L. Pavesi, L. Dal Negro, C. Mazzoleni, G. Franzò and F. Priolo, *Nature* **408**, 440 (2000).

[11] T. Lundstrom, W. Schoenfeld, H. Lee and P. M. Petroff, *Science* **286**, 2312 (1999).

[12] R. F. Service, *Science* **281**, 1930 (1998).

[13] M. Bruchez Jr., M. Moronne, P. Gin, S. Weiss and A. P. Alivisatos, *Science* **281**, 2013 (1998).

[14] W. C. W. Chan and S. Nie, *Science* **281**, 2016 (1998).

[15] M. A. Kastner, *Phys. Today* **46**(1), 24 (1993) and references therein.

[16] A. D. Yoffe, *Adv. Phys.* **42**, 173 (1993) and references therein.

[17] N. F. Johnson, *J. Phys.: Condens. Matter* **7**, 965 (1995) and references therein.

[18] A. P. Alivisatos, *Science* **271**, 933 (1996) and references therein.

[19] A. P. Alivisatos, *J. Phys. Chem.* **100**, 13226 (1996) and references therein.

[20] R. C. Ashoori, *Nature* **379**, 413 (1996) and references therein.

[21] P. L. McEuen, *Science* **278**, 1729 (1997).

[22] D. Gammon, *Science* **280**, 225 (1998).

[23] A. Zrenner, *J. Chem. Phys.* **112**, 7790 (2000) and references therein.

[24] D. Gammon, *Nature* **405**, 899 (2000).

[25] A. D. Yoffe, *Adv. Phys.* **50**, 1 (2001) and references therein.

[26] N. W. Ashcroft and N. D. Mermin, *Solid State Physics* (Holt, Rinehart and Winston, New York, 1976).

[27] R. P. Feynmann, *Caltech Engineering and Science Journal*, February 1960.

[28] P. Moriarty, *Rep. Prog. Phys.* **64**, 297 (2001) and references therein.

[29] D. M. Eigler and E. K. Schweizer, *Nature* **344**, 524 (1990).

[30] M. F. Crommie, C. P. Lutz and D. M. Eigler, *Science* **262**, 218 (1993).

[31] T. W. Fishlock, A. Oral, R. G. Egdell and J. B. Pethica, *Nature* **404**, 743 (2000).

[32] H. J. Lee and W. Ho, *Science* **286**, 1719 (1999).

[33] X. G. Peng, L. Manna, W. Yang, J. Wickham, E. Scher, A. Kadavanich and A. P. Alivisatos, *Nature* **404**, 59 (2000).

[34] L. Manna, E. C. Scher and A. P. Alivisatos, *J. Am. Chem. Soc.* **122**, 12700 (2000).

[35] V. F. Puntes, K. M. Krishnan and A. P. Alivisatos, *Science* **291**, 2115 (2001).

[36] C. A. Mirkin, R. L. Letsinger, R. C. Mucic and J. J. Storhoff, *Nature* **382**, 607 (1996).

[37] A. P. Alivisatos, K. P. Johnsson, X. Peng, T. E. Wilson, C. J. Loweth, M. P. Bruchez Jr. and P. G. Schultz, *Nature* **382**, 609 (1996).

[38] A. K. Boal, F. Ilhan, J. E. DeRouchey, T. Thurn-Albrecht, T. P. Russel and V. M. Rotello, *Nature* **404**, 746 (2000).

[39] S. R. Whaley, D. S. English, E. L. Hu, P. F. Barbara and A. M. Belcher, *Nature* **405**, 665 (2000).

[40] C. A. Mirkin and T. A. Taton, *Nature* **405**, 626 (2000).

[41] H. Hofmeister, F. Huisken and B. Kohn, *Eur. Phys. J. D* **9**, 137 (1999).

[42] J.-Y. Marzin, J.-M. Gérard, A. Isräel, D. Barrier and G. Bastard, *Phys. Rev. Lett.* **73**, 716 (1994).

[43] M. Grundmann, J. Christen, N. N. Ledentsov, J. Böhrer, D. Bimberg, S. S. Ruvimov, P. Werner, U. Richter, U. Gösele, J. Heydenreich, V. M. Ustinov, A. Y. Egorov, A. E. Zhukov, P. S. Kop'ev and Z. I. Alferov, *Phys. Rev. Lett.* **74**, 4043 (1995).

[44] D. Gammon, E. S. Snow and D. S. Katzer, *Appl. Phys. Lett.* **67**, 2391 (1995).

[45] D. J. Norris and M. G. Bawendi, *Phys. Rev. B* **53**, 16338 (1996).

[46] S. A. Blanton, M. A. Hines and P. Guyot-Sionnest, *Appl. Phys. Lett.* **69**, 3905 (1996).

[47] S. A. Empedocles, D. J. Norris and M. G. Bawendi, *Phys. Rev. Lett.* **77**, 3873 (1996).

[48] L. Landin, M. S. Miller, M.-E. Pistol, C. E. Pryor and L. Samuelson, *Science* **280**, 262 (1998).

[49] N. H. Bonadeo, A. S. Lenihan, G. Chen, J. R. Guest, D. G. Steel, D. Gammon, D. S. Katzer and D. Park, *Appl. Phys. Lett.* **75**, 2933 (1999).

[50] D. Gammon, E. S. Snow, B. V. Shanabrook, D. S. Katzer and D. Park, *Science* **273**, 87 (1996).

[51] C. B. Murray, D. B. Norris and M. G. Bawendi, *J. Am. Chem. Soc.* **115**, 8706 (1993).

[52] E. E. Vdovin, A. Levin, A. Patanè, L. Eaves, P. C. Main, Y. N. Khanin, Y. V. Dubrovskii, M. Henini and G. Hill, *Science* **290**, 122 (2000).

[53] U. Meirav, M. A. Kastner and S. J. Wind, *Phys. Rev. Lett.* **65**, 771 (1990).

[54] R. C. Ashoori, H. L. Stormer, J. S. Weiner, L. N. Pfeiffer, S. J. Pearton, K. W. Baldwin and K. W. West, *Phys. Rev. Lett.* **68**, 3088 (1992).

[55] H. Drexler, D. Leonard, W. Hansen, J. P. Kotthaus and P. M. Petroff, *Phys. Rev. Lett.* **73**, 2252 (1994).

[56] S. Tarucha, D. G. Austing, T. Honda, R. J. van der Hage and L. P. Kouwenhoven, Phys. Rev. Lett. **77**, 3613 (1996).

[57] L. P. Kouwenhoven, D. G. Austing and S. Tarucha, *Rep. Prog. Phys.* **64**, 701 (2001).

[58] K. Likharev, *Nature* **410**, 531 (2001).

[59] M. W. Keller, J. M. Martinis, N. M. Zimmerman and A. H. Steinbach, *Appl. Phys. Lett.* **69**, 1804 (1996).

[60] M. W. Keller, A. L. Eichenberger, J. M. Martinis and N. M. Zimmerman, *Science* **285**, 1706 (1999).

[61] L. P. Kouwenhoven, T. H. Oosterkamp, M. W. S. Danoesastro, M. Eto, D. G. Austing, T. Honda and S. Tarucha, *Science* **278**, 1788 (1997).

[62] L. P. Kouwenhoven, T. H. Oosterkamp, S. Tarucha, D. G. Austing and T. Honda, *Physica B* **249-251**, 191 (1998).

[63] Y. Tokura, L. P. Kouwenhoven, D. G. Austing and S. Tarucha, *Physica B* **246-247**, 83 (1998).

[64] R. J. Warburton, C. Schäflein, D. Haft, F. Bickel, A. Lorke, K. Karrai, J. M. Garcia, W. Schoenfeld and P. M. Petroff, *Nature* **405**, 926 (2000).

[65] U. Banin, Y. Cao, D. Katz and O. Millo, *Nature* **400**, 542 (1999).

[66] M. Bayer, O. Stern, P. Hawrylak, S. Fafard and A. Forchel, *Nature* **405**, 923 (2000).

[67] D. Gammon, E. S. Snow, B. V. Shanabrook, D. S. Katzer and D. Park, *Phys. Rev. Lett.* **76**, 3005 (1996).

[68] S. W. Brown, T. A. Kennedy, D. Gammon and E. S. Snow, *Phys. Rev. B* **54**, R17339 (1996).

[69] D. Gammon, S. W. Brown, E. S. Snow, T. A. Kennedy, D. S. Katzer and D. Park, *Science* **277**, 85 (1997).

[70] R. C. Ashoori, H. L. Stormer, J. S. Weiner, L. N. Pfeiffer, K. W. Baldwin and K. W. West, *Phys. Rev. Lett.* **71**, 613 (1993).

[71] H. F. Hess, E. Betzig, T. D. Harris, L. N. Pfeiffer and K. W. West, *Science* **264**, 1740 (1994).

[72] A. Zrenner, L. V. Butov, M. Hagn, G. Abstreiter, G. Böhm and G. Weimann, *Phys. Rev. Lett.* **72**, 3382 (1994).

[73] D. R. Stewart, D. Sprinzak, C. M. Marcus, C. I. Duruöz and J. S. Harris Jr., *Science* **278**, 1784 (1997).

[74] W. Heller and U. Bockelmann, *Phys. Rev. B* **55**, R4871 (1997).

[75] D. G. Austing, Y. Tokura, S. Tarucha, T. H. Oosterkamp, J. W. Janssen, M. W. S. Danoesastro and L. P. Kouwenhoven, *Physica E* **6**, 358 (2000).

[76] S. A. Empedocles and M. G. Bawendi, *Science* **278**, 2114 (1997).

[77] N. C. van der Vaart, S. F. Godijn, Y. V. Nazarov, C. J. P. M. Harmans, J. E. Mooij, L. W. Molekamp and C. T. Foxon, *Phys. Rev. Lett.* **74**, 4702 (1995).

[78] F. R. Waugh, M. J. Berry, D. J. Mar, R. M. Westervelt, K. L. Campman and A. C. Gossard, *Phys. Rev. Lett.* **75**, 705 (1995).

[79] L. Kouwenhoven, *Science* **268**, 1440 (1995).

[80] R. H. Blick, R. J. Haug, J. Weis, D. Pfannkuche, K. V. Klitzing and K. Eberl, *Phys. Rev. B* **53**, 7899 (1996).

[81] D. Dixon, L. P. Kouwenhoven, P. L. McEuen, Y. Nagamune, J. Motohisa and H. Sakaki, *Phys. Rev. B* **53**, 12625 (1996).

[82] C. Livermore, C. H. Crouch, R. M. Westervelt, K. L. Campman and A. C. Gossard, *Science* **274**, 1332 (1996).

[83] G. Schedelbeck, W. Wegscheider, M. Bichler and G. Abstreiter, *Science* **278**, 1792 (1997).

[84] W. Wegscheider, G. Schedelbeck, M. Bichler and G. Abstreiter, *Physica E* **3**, 103 (1998).

[85] S. Tarucha, T. Honda, D. G. Austing, Y. Tokura, K. Muraki, T. H. Oosterkamp, J. W. Janssen and L. P. Kouwenhoven, *Physica E* **3**, 112 (1998).

[86] D. G. Austing, T. Honda, K. Muraki, Y. Tokura and S. Tarucha, *Physica B* **249-251**, 206 (1998).

[87] Y. Tokura, S. Sasaki, D. G. Austing and S. Tarucha, *Physica E* **6**, 676 (2000).

[88] Q. Xie, A. Madhukar, P. Chen and N. P. Kobayashi, *Phys. Rev. Lett.* **75**, 2542 (1995).

[89] G. S. Solomon, J. A. Trezza, A. F. Marshall and J. S. Harris Jr., *Phys. Rev. Lett.* **76**, 952 (1996).

[90] C. B. Murray, C. R. Kagan and M. G. Bawendi, *Science* **270**, 1335 (1995).

[91] R. P. Andres, J. D. Bielefeld, J. I. Henderson, D. B. Janes, V. R. Kolagunta, C. P. Kubiak, W. J. Mahoney and R. G. Osifchin, *Science* **273**, 1690 (1996).

[92] P. Guyot-Sionnest and M. A. Hines, *Appl. Phys. Lett.* **72**, 686 (1998).

[93] M. Shim and P. Guyot-Sionnest, *Nature* **407**, 981 (2000).

[94] C. Wang, M. Shim and P. Guyot-Sionnest, *Science* **291**, 2390 (2001).

[95] Y. Kayanuma, *Phys. Rev. B* **38**, 9797 (1988).

[96] B. Szafran, J. Adamowski and S. Bednarek, *Physica E* **4**, 1 (1999).

[97] S. Bednarek, B. Szafran and J. Adamowski, *Phys. Rev. B* **59**, 13036 (1999).

[98] D. Pfannkuche, V. Gudmundsson and P. A. Maksym, *Phys. Rev. B* **47**, 2244 (1993).

[99] R. Yang and P. P. Ruden, *J. Appl. Phys.* **78**, 1798 (1995).

[100] J.-L. Zhu, J.-Z. Yu, Z.-Q. Li and Y. Kawazoe, *J. Phys.: Condens. Matter* **8**, 7857 (1996).

[101] J.-L. Zhu, Z.-Q. Li, J.-Z. Yu, K. Ohno and Y. Kawazoe, *Phys. Rev. B* **55**, 15819 (1997).

[102] R. M. G. García-Castelán, W. S. Choe and Y. C. Lee, *Phys. Rev. B* **57**, 9792 (1998).

[103] M. Rontani, F. Rossi, F. Manghi and E. Molinari, *Phys. Rev. B* **59**, 10165 (1999).

[104] B. Szafran, J. Adamowski and S. Bednarek, *Physica E* **5**, 185 (2000).

[105] I.-H. Lee, Y.-H. Kim and K.-H. Ahn, *J. Phys: Condens. Matter* **13**, 1987 (2001).

[106] A. Aharony, O. Entin-Wohlman and Y. Imry, *Phys. Rev. B* **61**, 5452 (2000).

[107] L. E. Brus, *J. Chem. Phys.* **79**, 5566 (1984).

[108] L. E. Brus, *J. Chem. Phys.* **80**, 4403 (1984).

[109] L. E. Brus, *J. Phys. Chem.* **90**, 2555 (1986).

[110] Y. Kayanuma, *Phys. Rev. B* **41**, 10261 (1990).

[111] Y. Kayanuma, *Solid State Comm.* **59**, 405 (1986).

[112] Y. Kayanuma, *Appl. Phys. A* **53**, 475 (1991).

[113] Y. Kayanuma, *Phys. Rev. B* **44**, 13085 (1991).

[114] A. Alavi, *J. Chem. Phys.* **113**, 7735 (2000).

[115] J. Adamowski, M. Sobkowicz, B. Szafran and S. Bednarek, *Phys. Rev. B* **62**, 4234 (2000).

[116] T. Ezaki, N. Mori and C. Hamaguhi, Phys. Rev. B **56**, 6428 (1997).

[117] D. G. Austing, S. Sasaki, S. Tarucha, S. M. Reimann, M. Koskinen and M. Manninen, Phys. Rev. B **60**, 11514 (1999).

[118] Al. L. Efros and A. V. Rodina, *Phys. Rev. B* **47**, 10005 (1993).

[119] Al. L. Efros, M. Rosen, M. Kuno, N. Nirmal, D. J. Norris and M. Bawendi, *Phys, Rev. B* **54**, 4843 (1996).

[120] G. Cantele, D. Ninno and G. Iadonisi, *J. Phys.: Condens. Matter* **12**, 9019 (2000).

[121] G. Cantele, D. Ninno and G. Iadonisi, *Nanoletters* **1**, 121 (2001).

[122] J. A. Stratton, P. M. Morse, L. J. Chu, J. D. C. Little and F. J. Corbatò, *Spheroidal Wave Functions* (New York: John Wiley & Sons, Inc., 1956).

[123] L. Bianchi, *Lezioni di Geometria Differenziale* (Nicola Zanichelli Editore, Bologna, 1904).

[124] M. Abramovitz and I. A. Stegun, *Handbook of Mathematical Formulas* (Dover Publications, Inc., New York, 1972).

[125] L. Bányai, I. Galbraith, C. Ell and H. Haug, *Phys. Rev. B* **36**, 6099 (1987).

[126] D. Babić, R. Tsu and R. F. Greene, *Phys. Rev. B* **45**, 14150 (1992).

[127] J.-N. Chazalviel, F. Ozanam and V. M. Dubin, *J. Phys. I France* **4**, 1325 (1994).

[128] T. Takagahara, *Phys. Rev. B* **47**, 4569 (1993).

[129] P. G. Bolcatto and C. R. Proetto, *Phys. Rev. B* **59**, 12487 (1999).

[130] G. Cantele, D. Ninno and G. Iadonisi, *Phys. Rev. B* **64**, 125325-1 (2001).

[131] P. M. Morse and H. Feshbach, *Methods of Theoretical Physics* (New York: McGraw-Hill Book Company, Inc., 1953).

[132] F. Bassani and G. Pastori Parravicini, *Electronic States and Optical Transitions in Solids*, Pergamon Press, Oxford, 1975.

[133] L.-W. Wang and A. Zunger, Phys. Rev. Lett. **73**, 1039 (1994).

[134] L.-W. Wang and A. Zunger, *Phys. Rev. B* **53**, 9579 (1996).

[135] M. Lannoo, C. Delerue and G. Allan, *Phys. Rev. Lett.* **74**, 3415 (1995).

[136] R. Tsu, D. Babić and L. Ioriatti Jr., *J. Appl. Phys.* **82**, 1327 (1997).

[137] A. Franceschetti, A. Williamsom and A. Zunger, *J. Phys. Chem. B* **104**, 3398 (2000).

[138] A. G. Cullis, L. T. Canham and P. D. J. Calcott, *J. Appl. Phys.* **82**, 909 (1997) and references therein.

[139] A. G. Cullis and L. T. Canham, *Nature* **353**, 335 (1991).

[140] L. T. Canham, *Appl. Phys. Lett.* **57**, 1046 (1990).

[141] M. J. Sailor, *Sensor applications of porous silicon*, in: *Properties of Porous Silicon* edited by L. Canham (INSPEC, London, 1997), p. 364.

[142] G. Di Francia, F. De Filippo, V. La Ferrara, L. Quercia, L. Lancellotti, C. Baratto, E. Comini, G. Faglia and G. Sberveglieri, *Porous silicon layer for the detection at R. T. of low concentrations of vapours from organic compounds*, in: *Proceedings of Eurosensors XII*, Southampton, UK, 13-16 September 1998, pp. 544-547.

[143] G. Di Francia, V. La Ferrara, T. Fasolino, L. Quercia, L. Lancellotti, G. Iadonisi, D. Ninno, in: *Proceedings of the 4th Italian Conference on Sensors and Microsystems* edited by C. Di Natale, A. D'Amico and G. Sberveglieri (World Scientific, Singapore, 2000), p. 134.

[144] G. M. Halloran, J. Groeneweg, P. M. Sarro and P. J. French, *Proc. Eurosensors XII*, Southampton, UK, 13-16 September 1998, pp. 489 - 492.

[145] H. Fujii, S. Kanemaru, T. Matsukawa and J. Itoh, *Appl. Phys. Lett.* **75**, 3986 (1999).

[146] D. J. Lockwood, *Solid State Commun.* **92**, 101 (1994).

[147] B. Hamilton, J. Jacobs, D. A. Hill, R. F. Pettifer, D. Teehan and L. T. Canham, *Nature* **393**, 443 (1998).

[148] P. D. J. Calcott, K. J. Nash, L. T. Canham, M. J. Kane and D. Brumhead, *J. Phys.: Condens. Matt.* **5**, L91 (1993).

[149] D. Ninno, P. Maddalena and G. Di Francia, in: *Structural and Optical Properties of Porous Silicon Nanostructures* edited by G. Amato, C. Delerue and H.-J. von Bardeleben (Gordon and Breach Science Publishers, The Netherlands, 1997), p. 111.

[150] P. Malý, F. Trojánek, J. Kudrna, A. Hospodková, S. Banás, V. Kohlová, J. Valenta and I. Pelant, *Phys. Rev. B* **54**, 7929 (1996).

[151] D. Ninno, G. Iadonisi and F. Buonocore, *Solid State Comm.* **112**, 521 (1999).

[152] F. Buonocore and G. Cantele, in: *Porous Semiconductors - Science and Technology*, edited by V. Parkhutik and L. Canham (Rayton Impresores, Valencia, Spain, 2000).

[153] D. Ninno, G. Iadonisi, F. Buonocore, G. Cantele and G. Di Francia, *Sensors and Actuators B* **68**, 17 (2000).

[154] F. Buonocore, D. Ninno and G. Iadonisi, *phys. stat. sol. (b)* **225**, 343 (2001).

[155] A. Messiah, *Quantum Mechanics*, vol. I (North-Holland, Amsterdam, 1991).

[156] D. Bilenko, O. Belobrovaya, E. Jarkova, O. Coldobanova, I. Mysenko and E. Khasina, *Sens. and Actuators A* **62**, 621 (1997).

[157] G. Di Francia, V. La Ferrara, P. Maddalena, D. Ninno, L. P. Odierna and V. Cataudella, *Nuovo Cimento D* **18**, 1187 (1996).

[158] M. Reed and B. Simon, *Methods of Modern Mathematical Physics: Analysis of Operators* (Academic Press, London, 1978).

[159] D. Ninno, F. Buonocore, G. Cantele, G Iadonisi and G. Di Francia, in: *Proceedings of the 5th Italian Conference Extended to Meditarranean Countries on Sensors ad Microsystems*, edited by C. Di Natale, A. D'Amico and P. Siciliano (World Scientific, Singapore, 2000).

[160] G. Di Francia, M. L. Addonizio, G. Cantele, M. Della Noce, V. La Ferrara, L. Lancellotti, P. Morvillo, D. Ninno and L.Quercia, in: *Proceedings of the 6th National Conference on Sensors ad Microsystems*, Pisa, 5-7 February, 2001, edited by C. Di Natale, A. D'Amico and P. Siciliano (World Scientific, Singapore, 2001).

[161] J. von Behren, T. van Buuren, M. Zacharis, E. H. Chimovitz and P. M. Fauchet, *Solid State Commun.* **105**, 317 (1998).

[162] Qi Zhang and S. C. Baliss, *J. Appl. Phys.* **79**, 1351 (1996).

[163] J. Harper and M. J. Sailor, *Photoluminescence quenching and the photo-chemical oxidation of porous silicon by molecular oxygen*, *Langmuir* **13**, 4652 (1997).

[164] F. Buonocore, D. Ninno and G. Iadonisi, *Phys. Rev. B* **62**, 10914 (2000).

[165] H. Lüth, *Surfaces and Interfaces of Solid Materials* (Springer-Verlag, Berlin, 1997).

[166] R. C. T. da Costa, *Phys. Rev. A* **23**, 1982 (1981).

[167] M. Encinosa and B. Etemadi, *Phys. Rev. A* **58**, 77 (1998).

[168] *Semiconductor Sensors in Physico-Chemical Studies*, edited by L. Yu. Kupriyanov (Elsevier Science, Amsterdam, 1996).

[169] D. J. Lockwood, P. Schmuki, H. J. Labbé and J. W. Fraser, *Physica E* **4**, 102 (1999).

[170] B. Hamilton, *Semicond. Sci. Technol.* **10**, 1187 (1995) and references therein.

[171] T. Ando, A. B. Fowler and F. Stern, *Rev. Mod. Phys.* **54**, 437 (1982).

[172] G. Cantele, D. Ninno and G. Iadonisi, *Phys. Rev. B* **61**, 13730 (2000).

[173] D. Ninno, F. Buonocore, G. Cantele, and G. Iadonisi, *phys. stat. sol. a* **182**, 285 (2000).

[174] D. Ninno, G. Iadonisi, F. Buonocore and G. Cantele, in: *Porous Semiconductors - Science and Technology*, edited by V. Parkhutik and L. Canham (Rayton Impresores, Valencia, Spain, 2000).

[175] See, for istance, V. I. Smirnov, *A Course of Higher Mathematics*, vol. II (Pergamon Press, Oxford, 1964).

[176] P. Duclos and P. Exner, *Rev. Math. Phys.* **7**, 73 (1995).

[177] J. Goldstone and R. L. Jaffe, *Phys. Rev. B* **45**, 14100 (1992).

[178] M. Shigeki, *Phys. Rev. A* **47**, 686 (1993).

[179] J. Harper, M. J. Sailor, *Langmuir* **13**, 4652 (1997).

[180] V. Lehmann, F. Hofmann, F. Möller and U. Grüning, *Thin Solid Films* **255**, 20 (1995).

[181] G. M. Credo, M. D. Mason and S. K. Buratto, *Appl. Phys. Lett.* **74**, 1978 (1999).

[182] J. Hu, L.-s. Li, W. Yang, L. Manna, L.-w. Wang and A. P. Alivisatos, *Science* **292**, 2060 (2001).

[183] L.-s. Li, J. Hu, W. Yang and A. P. Alivisatos, *Nanoletters* **1**, 349 (2001).

[184] T. Wolkenstein, *Electronic Processes on Semiconductor Surfaces during Chemisorption* (Consultants Bureau, New York, 1991).

[185] E. O. Kane, *J. Phys. Chem. Solids* **8**, 38 (1959).

[186] V. V. Mitin, V. A. Kochelap and M. A. Stroscio, *Quantum Heterostructures: Microelectronics and Optoelectronics* (Cambridge University Press, Cambridge, 1999).

[187] D. I. Chepic, Al. L. Efros, A. I. Ekimov, M. G. Ivanov, V. A. Kharchenko, I. A. Kudriavtsev and T. V. Yazeva, *J. Lumin.* **47**, 113 (1990).

[188] A. I. Ekimov, F. Hache, M. C. Schanne-Klein, D. Ricard, C. Flytzanis, I. A. Kudryavtsev, T. V. Yazeva, A. V. Rodina and Al. L. Efros, *J. Opt. Soc. Am. B* **10**, 100 (1993).

[189] E. O. Kane, *J. Phys. Chem. Sol.* **1**, 249 (1956).

[190] L. S. Braginsky, *Phys. Rev. B* **57**, R6870 (1998).

[191] L. S. Braginsky, *Phys. Rev. B* **60**, R13970 (1999).

[192] A. Franceschetti and A. Zunger, *Phys. Rev. B* **62**, 2614 (2000).

[193] H. Fu, L.-W. Wang and A. Zunger, *Phys. Rev. B* **57**, 9971 (1998).

[194] L.-W. Wang and A. Zunger, *J. Phys. Chem.* **98**, 2158 (1994).

[195] L.-W. Wang and A. Zunger, *J. Chem. Phys.* **100**, 2394 (1994).

[196] L.-W. Wang and A. Zunger, *Phys. Rev. B* **51**, 17398 (1995).

[197] L.-W. Wang and A. Zunger, *Phys. Rev. B* **54**, 11417 (1996).

[198] L.-W. Wang and A. Zunger, *Phys. Rev. B* **59**, 15806 (1999).

[199] M. V. Rama Krishna and R. A. Friesner, *Phys. Rev. Lett.* **67**, 629 (1991).

[200] M. V. Rama Krishna and R. A. Friesner, *J. Chem. Phys.* **95**, 8309 (1991).

[201] M. V. Rama Krishna and R. A. Friesner, *J. Chem. Phys.* **96**, 873 (1991).

[202] A. Tomasulo and M. V. Rama Krishna, *J. Chem. Phys.* **105**, 3612 (1996).

[203] J. P. Proot, C. Delerue and G. Allan, *Appl. Phys. Lett.* **61**, 1948 (1992).

[204] C. Delerue, G. Allan and M. Lannoo, *Phys. Rev. B* **48**, 11024 (1993).

[205] C. Delerue, M. Lannoo and G. Allan, *Phys. Rev. Lett.* **76**, 3038 (1996).

[206] N. A. Hill and K. B. Whaley, *Phys. Rev. Lett.* **75**, 1130 (1995).

[207] N. A. Hill and K. B. Whaley, *Phys. Rev. Lett.* **76**, 3039 (1996).

[208] J.-M. Jancu, R. Scholz, F. Beltram and F. Bassani, *Phys. Rev. B* **57**, 6493 (1998).

[209] G. Allan, Y. M. Niquet and C. Delerue, *Appl. Phys. Lett.* **77**, 639 (2000).

[210] Y. M. Niquet, G. Allan, C. Delerue and M. Lannoo, *Appl. Phys. Lett.* **77**, 1182 (2000).

[211] J. R. Chelikowsky, N. Troullier and Y. Saad, *Phys. Rev. Lett.* **72**, 1240 (1994).

[212] S. Öğüt, J. R. Chelikowsky and S. G. Louie, Phys. Rev. Lett. **79**, 1770 (1997).

[213] J. R. Chelykowsky, Y. Saad, S. Öğüt, I. Vasiliev and A. Stathopoulos, *phys. stat. sol. (b)* **217**, 273 (2000).

[214] J. R. Chelykowsky, *J. Phys. D: Appl. Phys.* **33**, R33 (2000) and references therein.

[215] A. Mizel and M. L. Cohen, *Phys. Rev. B* **56**, 6737 (1997).

[216] A. Mizel and M. L. Cohen, *Solid State. Commun.* **104**, 401 (1997).

[217] A. Mizel and M. L. Cohen, *Solid State. Commun.* **113**, 189 (2000).

[218] G. Birkhoff and G. C. Rota, *Ordinary Differential Equations* (Boston and New York: Ginn & Co., 1962).

[219] P. B. Bailey, *SIAM J. Appl. Math.* **14**, 242 (1966).

[220] W. H. Press, S. A. Teukolsky, W. T. Vetterling and B. P. Flannery, *Numerical Recipes in Fortran 77*, vol. 1 New York: Cambridge University Press, 1999 and references therein.